



School of Chemistry

Fabrication of Nanostructured Diamond for Electrochemical Applications

Luca Riley

**This thesis is submitted in partial fulfilment of the requirements for the Honours Degree of
MSci (Bsc) at the University of Bristol**

[Supervisor] Paul. W. May
[Second Assessor] David J. Fermin
[Section] Physical & Theoretical

Statement of Limiting Factors

The progress of this project was hindered due to these factors:

1. The pump for the Hot Filament Chemical Vapour Deposition reactor was unusable and required replacement. This delayed the progress of boron-doped diamond deposition by a few weeks.
2. The electrode holder produced did not meet the requirements of the specifications and had to be altered. This hindered the progress of analysis that required the three-electrode set-up.
3. Several factors limited production of the Electron Beam Lithography (EBL) substrates:
 - (i) Time constraints: due to limited hours available to staff to produce our samples, the total fabrication time was increased.
 - (ii) Budget constraints: the EBL process is expensive and required a significant portion of funds. This limited the number of conditions that could be attempted at a time.

This meant that deposition of BDD on the final EBL-Si substrates could not be done and so subsequent cyclic voltammetry and nickel deposition could not be performed.

Abstract

High surface area nanostructured boron-doped diamond (BDD) electrodes offer promising potential for electrochemical analysis, sensing and deposition. This report focuses on optimising the surface area of electron beam lithography silicon substrates (EBL-Si). Scanning electron microscopy (SEM) analysis reveals insights into the impact of parameters such as pitch (P) and column thickness (T) on electrode morphology and surface area. At this stage, T = 200 nm and P = 600 nm are deemed to be suitable values. However, EBL-Si substrates with a P = 1000 nm have also been fabricated.

Included in this report is a comparison between the performance of flat electrodes (f-BDD) and high surface area nanostructured black diamond electrodes (bD-BDD). Hot filament chemical vapour deposition (HFCVD) was used to produce all BDD electrodes. The comparison between f-BDD and bD-BDD was achieved using Scanning Electron Microscopy (SEM), Energy-dispersive X-ray Spectroscopy (EDX), laser Raman and Cyclic Voltammetry.

Cyclic Voltammetry experiments demonstrated the importance of surface termination and electrode surface area on the double-layer capacitance of the BDD electrodes. A 1.85x increase in capacitance is seen for an O-terminated f-BDD electrode compared to an H-terminated electrode. A 21.93x increase in double-layer capacitance is observed for a bD-BDD electrode compared to an f-BDD electrode.

The electrochemical deposition of a Ni-Cu alloy onto the electrode surface was followed by the dissolution of the nobler component (Cu) from the alloy. A Ni(II) and Cu(II) aqueous solution was used at room temperature for this process. Successful hydrogen evolution has also been shown.

Acknowledgements

I would like to express my gratitude to my supervisor Professor Paul May for his guidance and recommendations throughout the progress of this report. I would also like to thank Professor David Fermin for his suggestions and support.

I would like to thank Kisty Mao for her encouragement and assistance in the lab. Thank you to Alex Black for providing us with essential knowledge and equipment. I would also like to thank Dr James Smith for his advice on laser Raman.

Table Of Contents

Statement of Limiting Factors	1
Abstract	2
Acknowledgements	3
Chapter 1 Introduction	8
1.1. Properties of Diamond	8
1.2. Band Gap Theory.....	9
1.2.1. Band Gap (Intrinsic Semiconductors).....	9
1.2.2. Band Gap (Insulators)	10
1.2.3. Direct and Indirect Band Gap Semiconductors	10
1.2.4. Wide Band Gap Semiconductors	11
1.3. Electrochemical Cells.....	11
1.3.1. History of Electrochemical Cells.....	11
1.3.2. Different Types of Electrochemical Cells.....	11
1.4. BDD & Electrochemical Theory	11
1.4.1. Metal Electrode Electrochemistry	12
1.4.2. Electrode-Electrolyte Interface	12
1.4.3. P-Type Semiconductor Electrochemistry	13
1.4.4. BDD Electrode Electrochemistry	14
1.4.4.1. Electrode Surface Termination Tunability	14
1.4.4.2. Charge Transfer Mechanism	14
1.4.4.3. Variations to Doping Level	14
1.4.4.4. Inactive Dopants	15
1.5. BDD & Electrochemical Applications.....	16
1.5.1. Electroanalysis	16
1.5.1.1. Detection of DTG.....	16
1.5.1.2. Detection of NADH & Ethanol.....	16
1.5.1.3. Detection of Carbamate Pesticides.....	16
1.5.1.4. Detection of Heavy Metals in Water	16
1.5.2. Electrosynthesis	17
1.5.3. Optically Transparent Electrodes (OTEs).....	17
1.5.4. Supercapacitors	17
1.5.5. Electrodeposition for Hydrogen Evolution.....	18
1.5.5.1. Hydrogen Evolution.....	18
1.5.5.1.1. Acidic Electrolytes	18
1.5.5.1.2. Alkaline Electrolytes.....	19
1.5.5.2. Nickel Electrodes for Hydrogen Evolution.....	20
1.5.5.3. Electrodeposition & Dealloying of Nickel-Copper Alloys	20
1.5.5.3.1. Boron-doped Diamond Support Layer	20
1.5.5.3.2. Ni-Cu Alloy Deposition	20
1.5.5.3.3. Selective Dissolution & Passivation.....	21
1.6. Project Aims & Objectives	22

Chapter 2 Chemical Vapour Deposition (CVD) & Diamond	23
2.1. CVD as a Method for Diamond Growth.....	23
2.2. CVD Gas Phase Chemistry.....	23
2.2.1. CH ₄ /H ₂ Gas-Phase Chemistry	23
2.2.2. CH ₄ /H ₂ /B ₂ H ₆ Gas-Phase Chemistry	24
2.3. Diamond CVD Techniques.....	25
2.3.1. Plasma-Enhanced CVD (PECVD).....	25
2.3.2. Hot Filament CVD (HFCVD)	26
2.4. Nanostructure Boron-Doped Diamond	27
2.4.1. Introduction	27
2.4.2. Bottom-up Approach	27
2.4.2.1. Nano-cone Structures	27
2.4.2.2. Umbrella Structures.....	27
2.4.3. Top-down Approach	28
2.4.3.1. Nano-whisker Structures	28
2.4.3.2. Honeycomb Structures	28
2.4.3.3. Carbon Nanotubes (CNTs) & Teepee-like Structures.....	29
2.4.3.4. Nanotip Structures.....	30
2.4.3.5. Black Silicon (bSi) Structures for Black Diamond (bD).....	31
2.4.3.6. Electron Beam Lithography Columns.....	32
2.5. Diamond Nucleation Techniques	34
2.5.1. Heterogeneous Nucleation – Surface Nucleation	34
2.5.1.1. Mechanical Abrasion-enhanced Nucleation	34
2.5.1.2. Ion Implantation-enhanced Nucleation	34
2.5.1.3. Low Gas Pressure Nucleation.....	34
2.5.1.4. Bias-enhanced Nucleation (BEN)	34
2.5.2. Homogeneous Nucleation – Gas Phase Nucleation.....	35
2.6. Nanodiamond Seeding	35
2.6.1. Introduction	35
2.6.2. Surface Charge	36
2.6.3. Solvent Choice	36
2.6.4. Nanodiamond Seeding Technique	36
2.6.4.1. Mechanical Abrasion Seeding	36
2.6.4.2. Suspension Evaporation Seeding	37
2.6.4.3. Electrostatic Self-Assembly Seeding	37
Chapter 3 Characterisation Techniques.....	38
3.1. Scanning Electron Microscopy (SEM)	38
3.2. Energy Dispersive X-ray Spectroscopy (EDX)	38
3.3. Raman Spectroscopy	38
3.4. Cyclic Voltammetry (CV)	39
3.4.1. Nernst Equation	39
3.4.2. Capacitance	40
3.4.3. Surface Area Calculations	41

Chapter 4 Experimental	42
4.1. BDD Sample Preparation	42
4.1.1. Wafer Cutting.....	42
4.1.2. EBL Etching of Si Wafer	42
4.1.3. Nanodiamond Seeding	42
4.1.4. HFCVD	42
4.2. Electrode Preparation	43
4.2.1. f-BDD Electrode Preparation.....	43
4.2.2. bSi Electrode Preparation	43
4.3. Electrochemical Analysis	44
4.3.1. Cyclic Voltammetry for H-terminated Samples.....	44
4.3.2. Ozone Treatment for O-terminated CV Analysis.....	44
4.4. Electrodeposition & Dealloying	44
4.4.1. Electrodeposition.....	44
4.4.2. Dealloying	45
4.5. Scanning Electron Microscopy (SEM)	45
Chapter 5 Results & Discussion	46
5.1. Scanning Electron Microscopy (SEM) Results	46
5.1.1. EBL-Si Substrate Fabrication	46
5.1.1.1. Post-deposition Pattern Definition.....	46
5.1.1.2. EBL-Si Substrate Pattern Accuracy	47
5.1.2. Post-nickel Deposition & Dealloying Pattern Definition.....	48
5.1.2.1. f-BDD Electrode.....	48
5.1.2.2. bD-BDD Electrodes.....	48
5.2. Energy Dispersive X-ray Spectroscopy (EDX)	49
5.2.2. EDX for f-BDD	49
5.2.1.1. Lack of Nickel Deposition	49
5.2.1.2. Surface Contamination	50
5.2.1.3. Bulk Nickel-deposited Region	50
5.2.2. EDX for bD-BDD	51
5.2.2.1. bD (MM22)-Ni Bulk Deposition.....	51
5.2.2.2. bD (MM22)-Ni Close-up.....	52
5.3. Raman Spectroscopy	53
5.4. Cyclic Voltammetry	55
5.4.1. Effect of H- & O- Termination.....	55
5.4.2. Double Layer Capacitance of f-BDD & bD-BDD	56
5.4.3. Effective Surface Area of Electrodes	57
5.4.4. Effect of Scan Rate on Current	58
5.4.5. Ni-Cu Solution Cyclic Voltammetry	59
5.4.5.1. Anodic Potentials	60
5.4.5.2. Cathodic Potentials	60
5.4.5.3. H ₂ Evolution	60
5.4.5.4. Dealloying	61
Chapter 6 Conclusions	62

Chapter 7 Future Work	63
Chapter 8 References	64
Chapter 9 Appendix.....	70

Chapter 1 - Introduction

1.1. Properties of Diamond

Diamond is a structure with a tetrahedral coordination and two interpenetrating face-centred cubic (fcc) lattices that are occupied entirely by sp^3 hybridised carbon atoms. This lattice produces a repeating structure where each carbon atom has four carbon-carbon single bonds.¹ Since diamond is a tetrahedral structure, it will have a bond angle of 109° , as shown in **Figure 1.1**.

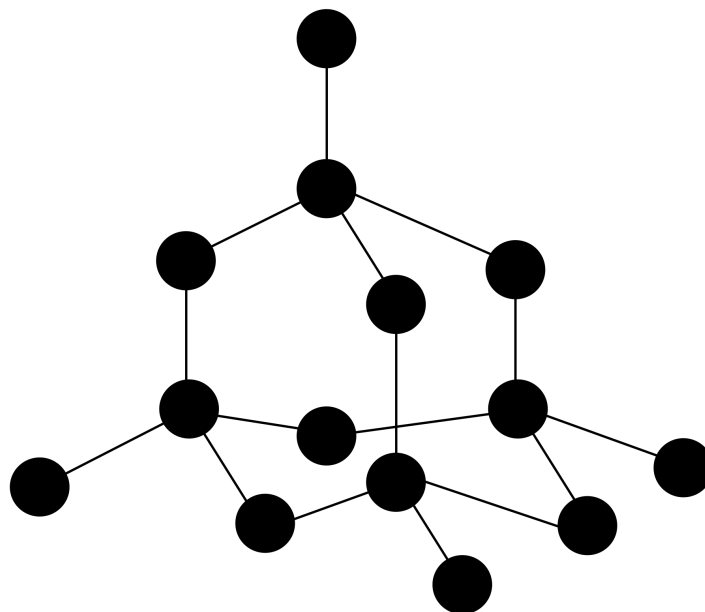


Figure 1.1. The tetrahedral coordination of diamond and the fcc lattices of sp^3 hybridised carbon.

Naturally formed diamonds occur with a mix of 98.9% ^{12}C and 1.1% ^{13}C as this represents the natural abundance of these two isomers in nature. Group IV elements (Carbon, Silicon, Germanium and Tin) can crystallise in the diamond structure by forming the necessary directional covalent bonds. Of this group, carbon is known to form the strongest bonds in the sp^3 diamond structure.² Diamond has several other valuable properties such as: (i) exceptional hardness, (ii) high melting point and (iii) high thermal conductivity. A more detailed list of the properties of diamonds can be found in **Table 1.1**.

Table 1.1. Some of the properties and associated values of diamond.

Property	Value
Band Gap ³	5.45 eV
Compressive Strength ⁴	110 GPa
Density ⁴	3.52 g cm ⁻³
Electron Mobility ³	2200 cm ² V ⁻¹ s ⁻¹
Heat Capacity ⁴	6.2 Jmol ⁻¹ K ⁻¹
Hole Mobility ³	1600 cm ² V ⁻¹ s ⁻¹
Hardness ⁵	10,000 Kg mm ⁻²

Optical Index of Refraction ⁵	2.41
Resistivity ⁶	$1 \times 10^{13} \Omega \text{ cm}$
Tensile Strength ⁵	1.2 GPa
Thermal Conductivity ³	$20 \text{ W cm}^{-1} \text{ K}^{-1}$
Thermal Expansion Coefficient ⁴	$1.1 \times 10^{-6} \text{ K}^{-1}$
Young's Modulus ⁴	1250 GPa

It is because of these properties that the growth of synthetic diamonds has become an area of interest as they have various commercial uses such as (i) Electronic Devices, (ii) Optical Windows,⁷ (iii) Abrasives⁸ and (iv) Heat Sinks.⁹

1.2. Band Gap Theory

1.2.1. Band Gap (Intrinsic Semiconductors)

The band gap (E_g) describes the energy spacing between the valence band edge (the highest region in the valence band) and the conduction band edge (the lowest region of the conduction band). At temperatures above 0K electrons will be raised from the valence band (VB) to the conduction band (CB) across the band gap, in a process called thermal excitation. The resulting electrons in the CB and holes in the VB will produce the material's electrical conductivity. Whereas, for intrinsic semiconductors at 0 K, there are no vacant states in the VB and all states in the CB are vacant. This means that intrinsic semiconductors are not electrically conductive at 0 K, as shown in **Figure 1.2**.¹⁰

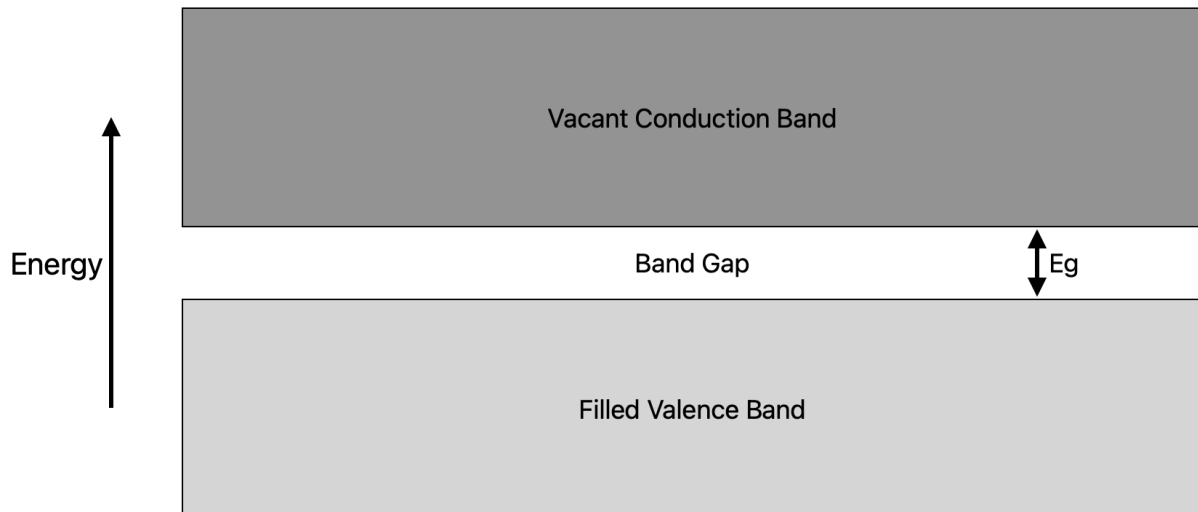


Figure 1.2. Diagram of the valence band, conduction band and band gap of an intrinsic semiconductor.

When an electron moves into the CB it breaks a covalent bond in the crystal lattice and creates a positively charged “hole”. At higher temperatures, more covalent bonds are broken and more electrons enter the CB. Since holes are also charge carriers, electron movements can be represented by the change in position of holes and the resulting current, as shown in **Figure 1.3**.¹¹

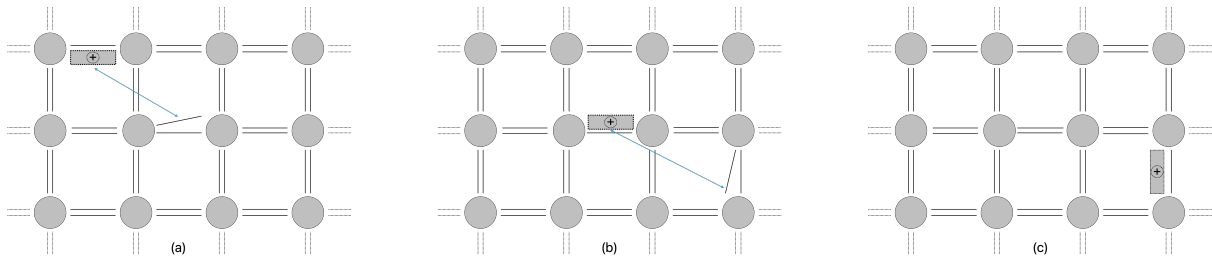


Figure 1.3. (a) the movement of electrons by breaking a covalent bond, (b) formation of a hole at the site of the broken covalent bond, (c) the recombination of the hole and the electron to reform the covalent bond.

1.2.2. Band Gap (Insulators)

The width of the band gap will affect the conductivity of the material, as a larger amount of energy is required to move an electron into the CB from the VB when the band gap is bigger. If the energy required to move an electron into the CB is too great the material can be classified as an insulator. Electrons may only cross the band gap, of an insulator, at very high temperatures or when a large electric field is applied.

1.2.3. Direct and Indirect Band Gap Semiconductors

When the CB edge is directly above the VB edge the semiconductor is described as a direct band gap semiconductor. In this case, the wave vectors of the valence and conduction band edges are the same. Whereas, in an indirect band gap material, the band edges have different wave vector values. This indicates that the direction and magnitude of the particle's momentums are not the same. Both situations are shown in **Figure 1.4**. A photon with an energy equal to the E_g (energy of the band gap) will produce an electron-hole pair easily since not much change in momentum is required. However, indirect band gaps require a lattice vibration (phonon) to achieve the change in momentum required to produce an electron-hole pair. This process is also true for the recombination of the electron-hole pair and so the process is faster for direct band gap semiconductors as they do not require a phonon. To conserve energy, recombination must result in the emission of photons with an energy corresponding to E_g . The differentiation between direct and indirect band gaps is important for determining the material's photoconductivity.^{12,13}

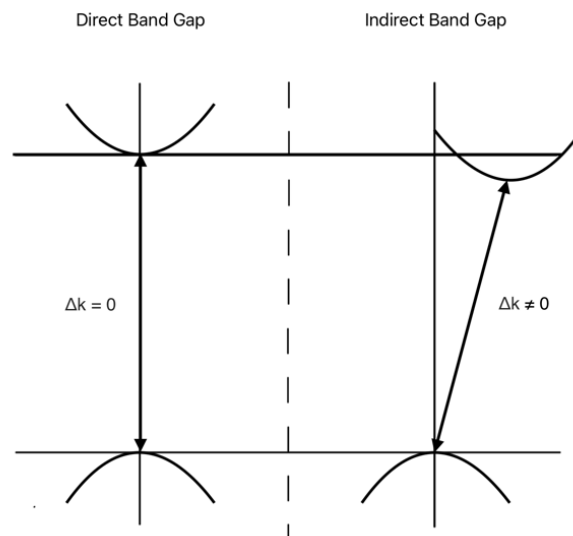


Figure 1.4. Schematic of direct and indirect optical transitions.

1.2.4. Wide Band Gap Semiconductors

A wide band gap (WBG) semiconductor is a material with a band gap larger than 2 eV making diamond (band gap = 5.45 eV) a good example of an indirect WBG material.¹⁴ WBG semiconductors can tolerate a higher voltage and switching frequency and therefore can act as more efficient power supplies. This is because WBG semiconductors can apply the same voltage while being thinner, reducing the conductive and switching losses.¹⁵ The benefits of these materials can be summarised as (i) a high operating frequency, (ii) a high output power and (iii) a high applied voltage.¹⁶

1.3. Electrochemical Cells

1.3.1. History of Electrochemical Cells

Volta (1800) developed the voltaic pile, the first documented electrochemical cell providing on-demand electricity. This “columnar machine” requires alternating zinc or silver metal plates separated by brine-soaked cardboard for it to work.¹⁷

This work was further developed by Davy, in 1806, who suggested that the decomposition of a compound would be affected by the electrical properties of the cell. This electrical current would be able to overcome the chemical affinity that kept the compound together and so he was able to separate the elements. This work established many of the principles of electrolysis.¹⁸

Faraday (1834) expanded on these principles and introduced laws for electrolysis. According to Faraday's First Law, the amount of substance deposited at the electrode-electrolyte interface is determined by the quantity of electricity passing through the electrolyte. Faraday's Second Law states that the masses of different compounds released or deposited at this interface are proportional to their respective chemical weights.¹⁹

1.3.2. Different Types of Electrochemical Cells

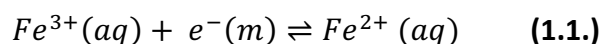
An electrochemical cell can be called either a galvanic or electrolytic cell when a faradaic current flows. If a reaction happens spontaneously, at electrodes which are joined together externally, it is a galvanic cell. Whereas, for an electrolytic cell, an external voltage must be applied for an electrode reaction to occur. If the reaction at only one of the electrodes is of interest, then it is not always necessary to make the distinction between galvanic and electrolytic.²⁰

1.4. BDD & Electrochemical Theory

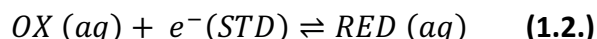
The electrochemistry of boron-doped diamond has been found to neither align with metal or semiconductor electrochemical theory directly. To better understand the potential uses of BDD it is necessary to further characterise the nature of the system.

1.4.1. Metal Electrode Electrochemistry

Electrons move between an electrode and a reactant causing a charge shift between the electrode and the solution, creating a potential difference:²¹



This can be expressed more generally as:



Metallic electrodes contain Fermi particles (electrons), that are described as being degenerate in a free electron gas (metal). They are said to follow the Fermi function and are characterised by the Fermi energy (E_f) which is set by electrons that can do work. It is for this reason that we can present the E_f value in terms of electron concentration (n_e) and our lowest allowed electron energy band. The Fermi level, for electrons in a metal, is shown below:²²

$$\varepsilon_F = \varepsilon_0 + \frac{(3\pi^2 n_e)^{\frac{2}{3}} \hbar^2}{2m_e} \quad (1.3.)$$

For the distribution of electrons, above 0K, the Fermi-Dirac distribution function must be employed. This function indicates the probability, $f(E)$, of an electron having the energy (E) at a given temperature (T). At $T = 0$, the probability that a particle will have an energy less than $E_f = 1$ is found by:

$$f(E) = \frac{1}{e^{(E-E_F/kT)} + 1} \quad (1.4.)$$

This suggests that available energy states below E_f will be filled by a fermion (e.g. an electron), at $T = 0$. Only at higher values of T , when particles have more energy, may electrons occupy higher levels than E_f .¹³

1.4.2. Electrode-Electrolyte Interface

The Gouy-Chapman theory can be used as a useful model for indicating the importance of the electrode-electrolyte interface in electrochemical solutions.²³ This model is an improvement over the Poisson-Boltzmann equation, an extension of Helmholtz's electric double layer (EDL) model from 1853. However, the Gouy-Chapman model, seen in **Figure 1.5. (b)**, is considered simplistic as ions are treated as points in a dielectric continuum and the electrode as a perfect conductor. The ion distribution near the interface is determined by electrostatic and statistical mechanics. Limitations of the Gouy-Chapman theory become apparent at higher electrolyte concentrations and high potentials.²⁴

Stern (1924)²⁵ modified Gouy (1910)²⁶ and Chapman's (1913)²⁷ work by introducing to the model a monolayer of specifically adsorbed ions with a set radius, as seen in **Figure 1.5. (c)** There is a significant decrease in electrostatic potential across the Stern layer and the plane separating the Stern and diffuse layers can be described as the slip (shear) plane.²⁴

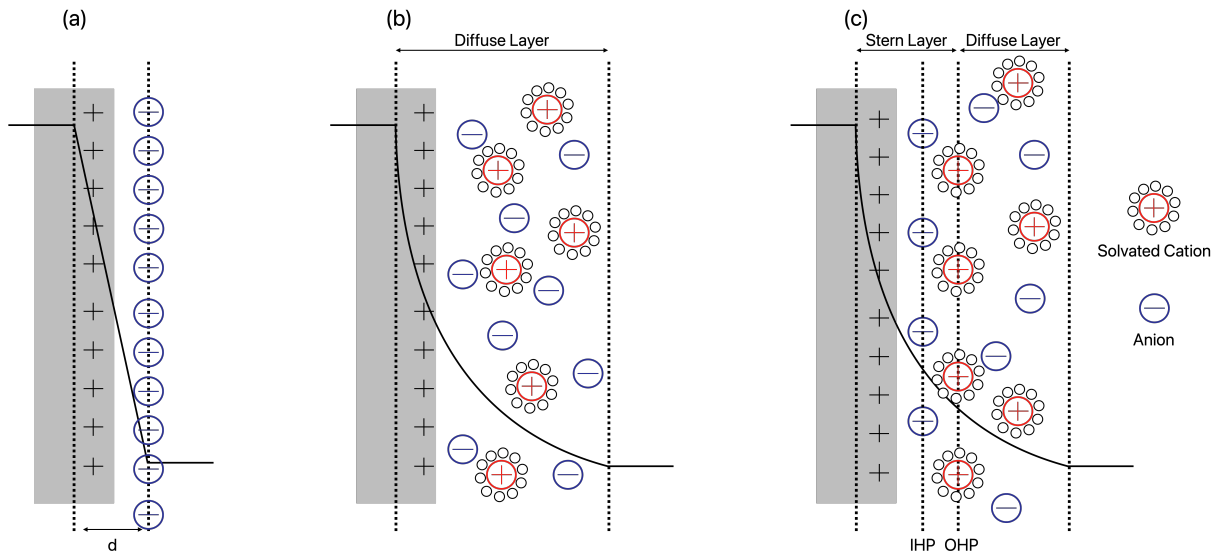


Figure 1.5. Electric Double Layer (EDL) represented by the (a) Helmholtz model, (b) Gouy-Chapman model and (c) Stern model. IHP is the Inner Helmholtz Plane & OHP is the Outer Helmholtz Plane.

1.4.3. P-Type Semiconductor Electrochemistry

Figure 1.6. shows that in an extrinsic semiconductor, the concentration of electrons and holes will not be equal. This change is caused by the addition of a small quantity of dopant atoms to the material that causes the material to favour one type of charge carrier over the other. For example, acceptor dopant atoms will increase the density of holes (a p-type semiconductor). This will lower the Fermi energy level (E_F), which relies on the distribution function, below the intrinsic level.¹¹ The hole is described as neutral when it is empty and negative when occupied by an electron. The p-type semiconductor is represented in **Figure 1.6.**

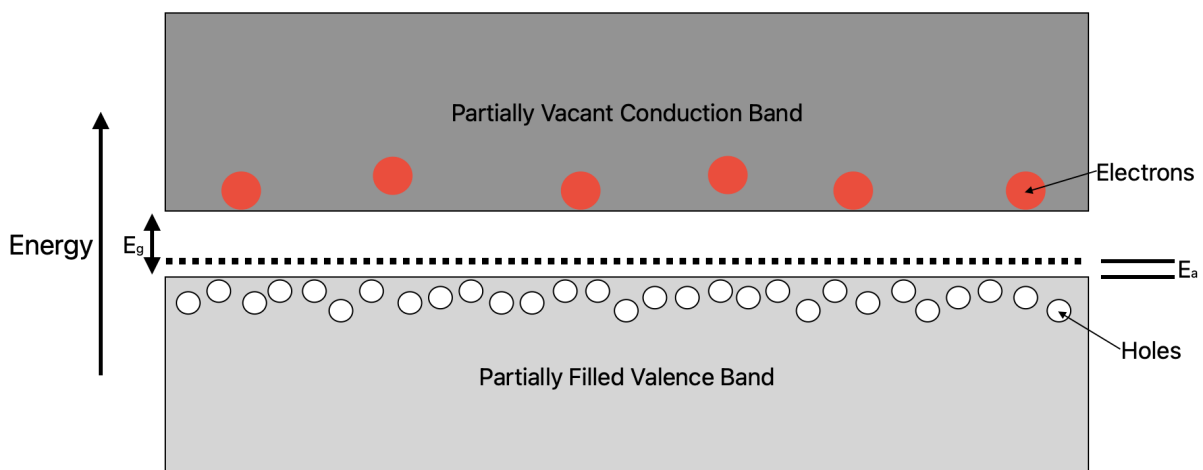


Figure 1.6. Valence band, conduction band and band gap of a p-type semiconductor.

This can also be described through calculation. The ionised acceptor concentration (N_A) is important as not all dopants are ionised at specific impurity energy levels or lattice temperatures. This value is necessary as the function of the semiconductor is limited by the ability of the system to transport charge and produce an electrical current. An expression for the concentration of ionised acceptors is shown below.

$$N_A^- = \frac{N_A}{1 + g_A e^{\frac{E_A - E_F}{kT}}} \quad (1.5.)$$

In a p-type material, the acceptor concentration is greater than the donor concentration ($N_A > N_D$). This leads to a situation where $p \gg n$, where p is the majority charge carrier (positive hole) in the valence band. The inverse will be true for an n-type material where the majority charge carriers (n) are electrons, as is also the case in metals. This means that for a p-type semiconductor $p \gg n_i \gg n$ where n_i is the intrinsic charge carrier concentration. An approximation can be made at higher temperatures because most donors and acceptors are ionised.²⁸

$$n + N_A = p + N_D \quad (1.6.)$$

1.4.4. BDD Electrode Electrochemistry

1.4.4.1. Electrode Surface Termination Tunability

BDD electrodes are often either oxygen (O)-terminated, or hydrogen (H)-terminated. O-terminated electrodes are hydrophilic compared to the hydrophobic H-terminated BDD surface initially produced. The surface will initially be H-terminated due to the conditions of the HFCVD process, where hydrogen gas remains in the chamber for a further two minutes after the other gasses have been removed. This is to remove products of graphitisation from the surface. The surface termination can be changed to allow for reactions that might otherwise be unfavourable, such as the reduction of N_2 to ammonia.²⁹

The surface termination will influence the work function and band bending and this can be measured by Ultraviolet Photoelectron Spectroscopy, to determine a change of 2 eV and 0.36 eV.³⁰ The induced band bending, by O-termination, will deplete the concentration of holes and lead to a depletion layer for the BDD electrode.³¹

1.4.4.2. Charge Transfer Mechanism

BDD demonstrates a surface-state mediated mechanism for charge transfer that allows for oxidative and reductive faradaic currents. This involves surface states, of the electrode, acting as charge carrier sinks. The oxidative process requires electron transfer between the redox system and the surface state, followed by hole transfer from the bulk to the electrode surface state.³²

1.4.4.3. Variations to Doping Level

Low-BDD electrodes are generally unsuitable for electrolysis, due to a low double-layer capacitance that is linked to a low density of states at the Fermi level. Altering the gas mixture significantly affects the double-layer capacitance, with 0.1% boron doping resulting in $2.5 \mu\text{F cm}^{-2}$, 1% ($8 \mu\text{F cm}^{-2}$), and 5% ($214 \mu\text{F cm}^{-2}$) capacitance respectively in 0.5 M H_2SO_4 .³³ For this reason, the boron doping concentration of the samples produced in this project is high.

At low doping concentrations, classical band conduction will control the overall carrier transport model for the material.³⁴ In this instance, boron atoms substitute carbon atoms to produce an acceptor level, 0.37 eV higher than the VB edge.³⁵

The p-type semiconductor behaviour can be attributed to the introduction of more impurity energy levels (acceptor levels). At 0K, the Fermi level initially sits within these energy levels due to the delocalization of wave functions through quantum overlapping. However, as shown in **Figure 1.7. (c)**, Coulombic repulsion can lead to the splitting of the initially half-filled 'impurity band' into an empty and full band which makes diffusive transport possible.³⁶ These bands may overlap when the doping level of the semiconductor is sufficiently increased.

Doping beyond the critical concentration shifts the ionisation energy causing the states associated with the acceptor levels to become extended. The result is the merging of the impurity band with the VB to induce metallic conduction, **Figure 1.7. (e)**.¹⁵³

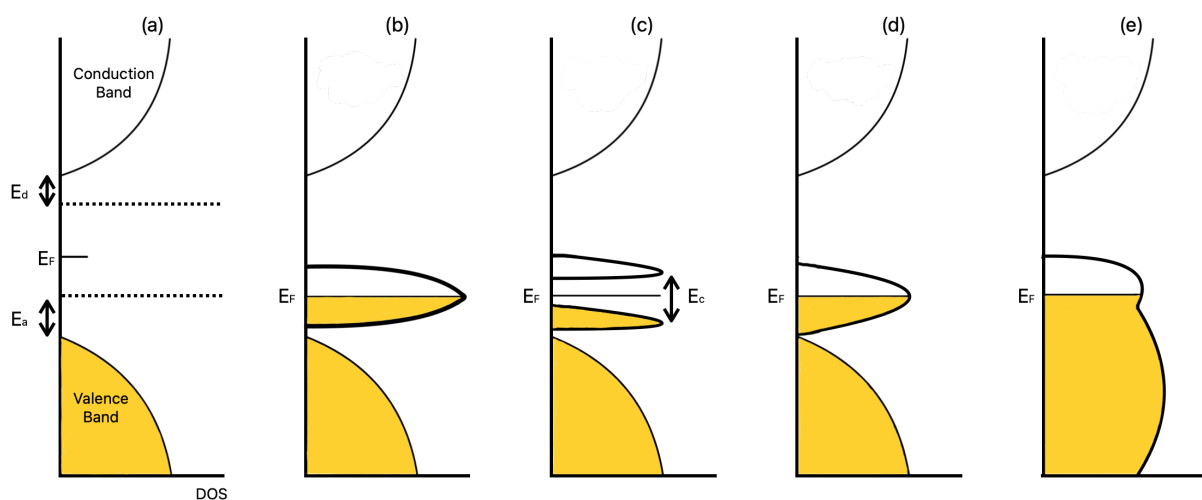


Figure 1.7. Changes to Density of States (DOS) and Band Structure as p-type doping progressively increases. Filled states are represented in yellow.

1.4.4.4. Inactive Dopants

It is important to note that not all boron dopants that are introduced into the diamond lattice are active as acceptors. It is suggested that ~10% of all boron dopants will be electrically inactive.³⁷ This effect can arise due to the boron acting as a deep acceptor or because passivating atoms have been introduced, such as hydrogen.³⁸ These deep energy levels, that can form in the band gap, will negatively affect the material's transport properties.³⁹

At higher doping levels, the number of deep traps, otherwise known as recombination centres, increases. These deep traps are deep levels within the band gap which require greater energy to excite the charge carrier. Deep traps tend to be undesirable as they counteract the free charge carriers present due to doping. It is believed that these deep traps in highly BDD are partly caused by boron pairs at nearest-neighbour sites.⁴⁰

1.5. BDD & Electrochemical Applications

1.5.1. Electroanalysis

1.5.1.1. Detection of DTG

The field of electroanalysis using boron-doped diamond electrodes is now well established. For example, HIV integrase inhibitor dolutegravir (DTG) can be sensitively detected at BDD electrodes using cyclic voltammetry (CV) to detect $100 \mu\text{g mL}^{-1}$ DTG within the potential window from 0.0V to +1.30 V. For this experiment, the peak current was plotted against the DTG concentration across the range of 1.0 to $50.0 \mu\text{g mL}^{-1}$ (2.38×10^{-6} – 1.19×10^{-4} M). It is stated that this method is not able to detect DTG at as low concentrations as chromatographic techniques (in the range of a ng mL^{-1}) coupled with tandem mass spectrometry. However, BDD electrodes are presented as the cheaper, quicker and simpler method.⁴¹

1.5.1.2. Detection of NADH & Ethanol

A vital aspect of BDD electrodes is their suppression of the fouling process, which is necessary for the detection of the oxidation of NADH to NAD^+ . Also, a wide potential window, low capacitance and high signal-to-background ratio result in an improved signal that is required to detect molecules at low concentrations.

Fouling results in a decrease in current after the first cycle of a cyclic voltammetry scan. Therefore, limiting the impact of fouling is important in ensuring an electrode can detect small changes in current. BDD shows improved resistance to fouling in comparison to glassy carbon, graphene-modified glassy carbon and boron-doped graphene-modified glassy carbon electrodes.⁴²

NADH can also be used as an ethanol biosensor, where an alcohol dehydrogenase-impregnated membrane is assembled with the BDD electrode. The ethanol concentration is determined using the oxidation current from NADH.⁴³

1.5.1.3. Detection of Carbamate Pesticides

BDD electrodes have proved themselves to be an asset in the detection of potentially hazardous products that could pose a threat, not only to nature but humans as well. BDD electrodes are an eco-friendly alternative to mercury-based sensors as they don't require hazardous materials that could potentially leak. Once again, the wide potential window of BDD electrodes, compared to alternatives, is valuable. This property prevents them from performing undesirable side reactions, at the electrode, that produce unwanted gaseous products.⁴⁴

1.5.1.4. Detection of Heavy Metals in Water

BDD electrodes can be used to control lead-based pollutants in drinking water and are a valuable alternative to the current electrodes which are described as being expensive, having a low life expectancy and being unstable.⁴⁵ The good sensitivity of BDD is thought to be due to the low background current of the electrode.⁴⁶

1.5.2. Electrosynthesis

The application of BDD to reduce nitrate to ammonia, which forms the second half of the synthesis of ammonia can be performed using BDD electrodes. The first step is to oxidize nitrogen to nitrous oxide and then dissolve in water to produce the nitrate that is then electrochemically reduced by the BDD electrode.⁴⁷

1.5.3. Optically Transparent Electrodes (OTEs)

OTEs are of particular use as a Spectro electrochemical method for analysis, frequently being applied to the observation of electrode reaction mechanisms. The characterisation of conducting / semiconducting materials surfaces and electronic states is an important feature of OTE analysis.⁴⁸ Low-defect diamond structures have a wide optical window (225 nm (band gap edge) - deep IR region) and there are no electronic states between the valence and conductive bands. However, in BDD OTEs, the boron acceptor band and multi-phonon bands are formed in a way that reduces optical transparency.⁴⁹

BDD film growth for OTEs was improved on substrates such as quartz and undoped silicon, which were chosen for their high optical transparency. Electrical conductivity of the BDD OTE is due to charge carriers produced by substitutionally doping the diamond with boron impurities. However, these same impurities will lower the optical transparency of the material.⁵⁰ Film thickness must also be controlled as thick films can directly contribute to an increase in ohmic resistivity and the subsequent disruption of electron transfer.⁵¹ BDDs refractive index is somewhat high and so light (of wavelengths above 300 nm) is reflected. This effect is exacerbated by surface roughness.⁵²

1.5.4. Supercapacitors

Supercapacitors are materials which can improve a unit's power output and they have improved life cycles when compared to batteries. They are of interest in the renewables market partly for their use in electric vehicles (EVs). The role of the supercapacitor in this scenario is to assist in the output of peak power for acceleration. This is made more efficient as the supercapacitor can be recharged through regenerative braking. This ability is benefited by BDD, which has good recyclability due to its anti-fouling properties.⁵³

BDD has been promoted as a possible future double-layer supercapacitor device, due to its wide potential window. This is a useful value because the square of the potential window is known to be proportional to both the power (P) and the energy (E), of the electrode:⁵⁴

$$E = \frac{1}{2} CV^2 \quad (1.7.)$$

$$P = \frac{V^2}{4R_s} \quad (1.8.)$$

Improving the effective surface area of the BDD electrode can result in better outcomes for capacitance. However, very dense nanowire structures sometimes provide a similar faradaic current to that of a flat-BDD sample. An explanation for this is that the nanowires do not act like a nanostructured array but more like a homogeneous flat surface. This is because the

faradaic current is most affected by the diffusion length, L_D . Any structure which is on a far smaller scale than this will produce results similar to that of the flat-BDD sample.⁵⁵

BDD can also be a very attractive support material for the electrodeposition of alternative materials. For example, MnO_2 can be deposited onto a BDD support structure and subsequently be used as a supercapacitor. In this case, the great strength and hardness of BDD are what make it a valuable support structure.⁵⁶ Further discussion on the use of BDD in electrodeposition can be found in **Section 1.5.5**.

The Chemical Vapour Deposition (CVD) process for the formation of a heavily doped BDD film is the preferred process as CVD films can accommodate higher concentrations of boron than High-Pressure High-Temperature diamonds. The transition from insulating to metallic properties, as carrier concentration is increased, is a necessary process in producing a supercapacitor.⁵⁷ This transition has already been covered in more detail in **Section 1.4.4.3**.

1.5.5. Electrodeposition for Hydrogen Evolution

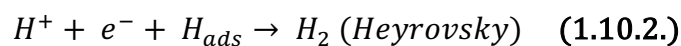
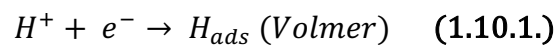
1.5.5.1. Hydrogen Evolution

The electrolytic splitting of water to produce hydrogen is seen as a viable alternative to the conventional industrial process, which requires methane steam reforming. This goal is hindered by the high energy and material cost of the process. These costs can be reduced by lowering the electrode overpotential and using less costly electrodes. The cost of the electrode can also be decreased by ensuring a high ratio between the effective area and the geometric area, as an improved surface area will produce a more efficient electrode.⁵⁸

The hydrogen evolution reaction (HER) and the oxygen evolution reaction (OER) are the two necessary half-reactions for splitting water. The chemical process and rate-determining step will be determined by the properties of the solution, as is seen in **Figures 1.8. & 1.9.**⁵⁹

1.5.5.1.1. Acidic Electrolytes

The Volmer step will require hydrogen adsorption and the second step will be either electrochemical (Heyrovsky) or chemical hydrogen desorption (Tafel):



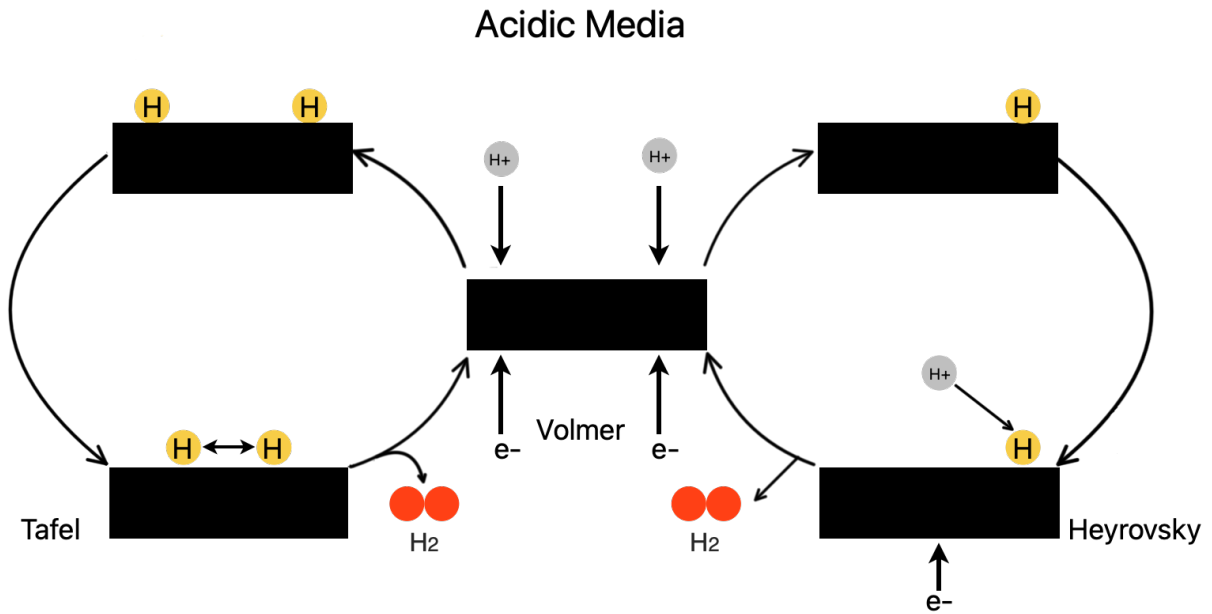


Figure 1.8. Diagram showing the Acidic HER mechanisms.⁵⁹

1.5.5.1.2. Alkaline Electrolytes

Step 1 (Volmer) requires the reduction of a water molecule to an adsorbed hydrogen and hydroxide molecules. Step 1 must be repeated so that two adsorbed hydrogen atoms can be combined to produce H₂ (Tafel) or one adsorbed hydrogen can combine with a water molecule to produce a hydrogen molecule and a hydroxide anion (Heyrovsky):⁶⁰

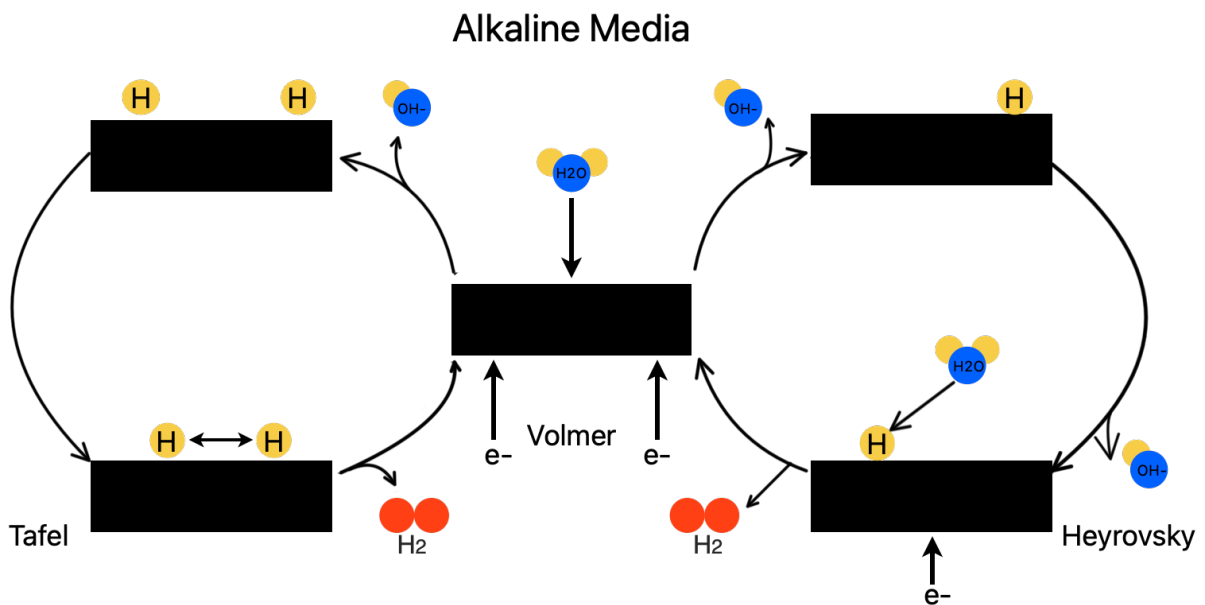
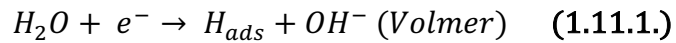


Figure 1.9. Diagram showing the Alkaline HER mechanisms.⁵⁹

1.5.5.2. Nickel Electrodes for Hydrogen Evolution

Nickel is known to be a valuable resource as a HER electrode since it is cheaper than many alternatives and is very chemically stable. Nickel also has a lower internal resistance than many other electrodes. This is an important aspect as it allows for greater current densities at reduced cell voltages. Reducing the required cell voltage will reduce the unit cost of the electrical power, making alkaline hydrolysis a more solid investment.⁶¹

The aspects of a useful electrode for hydrogen evolution can be summarised as the following: (i) High stability, (ii) Low Tafel slope and (iii) Lower overpotential at higher current densities. Another promising feature of Nickel is its valence range (-1 to +4) which allows for a greater number of electronic transitions.⁶²

The current density can be optimised at a set overpotential by increasing the surface area of the nickel electrode. This is because the electrolyte has greater coverage of the electrode surface. However, using a very dense nanostructured substrate can be detrimental as coating this with a thick nickel layer can cause agglomeration. This will cause the surface area to be reduced harshly, which will impact current density negatively.⁶³

To further improve the capability of a nickel electrode for HER, an alloy may be formed with another transition metal. For example, the presence of hetero atoms in a nickel layer may increase or decrease the energy of adsorption/desorption at the nickel atom site. The ratio of the two elements in the alloy is also an important factor for controlling the reduction in overpotential.

1.5.5.3. Electrodeposition & Dealloying of Nickel-Copper Alloys

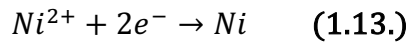
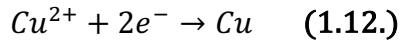
For cost-saving reasons, finding a universally active water-splitting catalyst is necessary. This is to ensure that the material is compatible between the hydrogen evolution reaction (HER) cathode and the oxygen evolution reaction (OER) anode.⁶⁴

1.5.5.3.1. Boron-doped Diamond Support Layer

BDD is a useful substrate for electrodeposition as the background current provided by the substrate is low in the useful potential range. The BDD electrode also has a large potential window which will allow for the deposition process to proceed without the formation of gaseous products from electrolysis. The anti-fouling nature of the BDD electrode is another useful feature for electrodeposition.⁶⁵

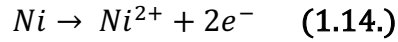
1.5.5.3.2. Ni-Cu Alloy Deposition

Nickel can be electrodeposited onto the boron-doped diamond electrode surface. This results in an increased surface area for the electrode due to the porous structure of the alloy.⁶⁶ Producing the nickel film first requires the deposition of a homogeneous and single-phase binary alloy of Ni-Cu. By applying a more negative potential, the rate of deposition of the nickel component of the Ni-Cu alloy can be increased. Whereas the rate of deposition of copper will not be affected by a change in potential, as it is diffusion-limited.⁶⁷ This culminates in an increased percentage of the as-deposited alloy being nickel, compared to copper, at more negative potentials. The electrochemical reactions, at the negative potential, for the deposition of the Ni-Cu alloy, are shown to be:

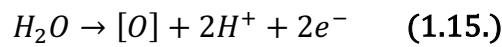


1.5.5.3.3. Selective Dissolution & Passivation

In the potential region below 0.2V, dissolution of Ni into the solution will be the primary reaction occurring at the electrode:



However, as the potential becomes more positive, the Ni is passivated leading to the selective dissolution of Cu and the formation of a Ni film. This is due to the formation of reactive atomic Oxygen in the 0.2 - 0.3V range:



The atomic Oxygen, [O], can react with the Ni element of the Ni-Cu alloy to form a Nickel Oxide, NiO, passive layer which selectively slows the dissolution of Ni.



The passivation process, induced by the formation of the NiO layer, seen in **Figure 1.9.**, is what allows for the selective anodic dissolution of the more noble metal, Cu, at greater potentials than 0.3V. At lower potentials, the Ni element is not protected by the NiO passive layer and so is dissolved, producing a porous Cu film.⁶⁸

NiO Passivating Layer

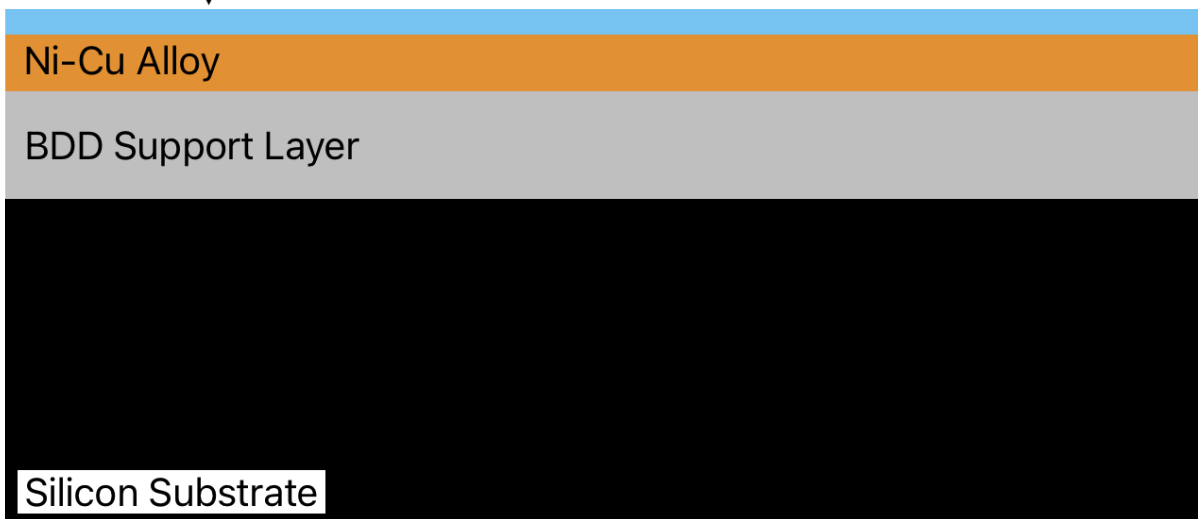


Figure 1.9. A representation of the side profile after deposition of the Ni-Cu Alloy.

Usually, it is the less noble metal that is selectively dissolved, as it is more thermodynamically active. This would result in a nanoporous network of copper. However, the passivation process is capable of kinetically stabilising the more thermodynamically

active element.⁶⁹ These kinetic and thermodynamic properties can have an impact on morphology as well as the elemental content of the network.⁷⁰

1.6. Project Aims & Objectives

This project aims to improve the electrochemical performance of boron-doped diamond electrodes. This will be done by increasing the effective surface area of the electrodes by altering the design patterns for black silicon and EBL-Si substrates and diamond growth conditions. Boron-doped diamond nanostructures will be produced using the Hot Filament Chemical Vapour Deposition (HFCVD) reactor and the electrodeposition/dealloying of a nickel-copper alloy will then be performed, on these nanostructures.

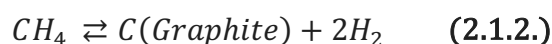
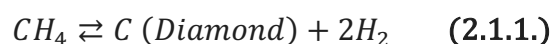
These electrodes will be analysed, at different stages of the process, by Scanning Electron Microscopy (SEM), Energy-dispersive X-ray Spectroscopy (EDX), Raman and Cyclic Voltammetry (CV).

A detailed review of relevant concepts will be provided. This will cover Semiconductors, Electrochemical Cells, Crystal Structure, Electroanalysis/synthesis/deposition, Gas phase chemistry, Nanostructures, Nucleation Techniques, Seeding and Analytical Methods.

Chapter 2 – Chemical Vapour Deposition (CVD) & Diamond

2.1. CVD as a Method for Diamond Growth

Chemical Vapour Deposition (CVD) is a valuable method used to deposit material upon a substrate surface in a step-by-step process. Despite graphene being the more thermodynamically stable form of carbon, diamond films can be deposited onto the substrate under reduced pressure by CVD. This is achieved by thermally decomposing a gaseous starting mixture that contains a carbon-based gas. This is often methane, however, is not the only gas that can be used in the gas medium. The process can be summarised with the following reaction:⁷¹



The growth of graphite over the diamond surface significantly hinders further preferential diamond growth.⁷² This can be addressed by selectively etching the graphene by introducing hydrogen into the gas phase to suppress graphitisation while affecting the diamond content minimally.⁷³ Diamond is only slightly less thermodynamically stable than crystalline graphite ($\Delta 2.90 \text{ kJ mol}^{-1}$).⁷⁴

2.2. CVD Gas Phase Chemistry

2.2.1. CH₄/H₂ Gas-Phase Chemistry

Early studies of the gas-phase chemistry of the CVD process for diamond growth indicated that atomic hydrogen and methyl radicals both play an important role in the proposed mechanisms. It is suggested that carbon atoms are added to the surface by either inserting themselves into dimer bonds or in the gaps between dimer bonds. These two sites must be filled in a 1:1 ratio for a new monolayer to form completely. This new monolayer may then dimerize with neighbouring carbons to form a 2x1 surface in an irreversible process.^{75,76} Diamond is metastable due to a high activation energy which prevents the transformation from diamond to graphite. This suggests that if graphitisation can be suppressed, diamond will form preferentially.⁷⁷ Therefore, the preferential generation of atomic hydrogen is crucial to diamond thin film growth rates.

Free carbon atoms, which might participate in the growth of the diamond layer, are relatively sparse in the vapour. This suggests that it is likely that a methane radical reacts with the surface and that the atomic hydrogen preferentially etches away any products of graphitisation.⁷⁸ A proposed mechanism for the insertion of carbon into the crystal structure is shown in **Figure 2.1**. Under atmospheric conditions, a high hydrogen: methane ratio is necessary for the competition between atomic hydrogen evolution and recombination.⁷⁹

However, the concentration of hydrogen and methane will also influence the diamond crystal size. By increasing the concentration of methane, the crystal size will decrease.⁸⁰ This

results in the surface becoming smoother and changing from microcrystalline (MCD) to nanocrystalline (NCD) as the number of grain boundaries increases. Grain boundaries are prone to graphitisation, resulting in the NCD surfaces having more graphitic impurities than MCD surfaces. If the methane ratio in the gas mixture is further increased, the film will eventually graphitise. This is because, relative to the amount of methane, there is not enough atomic hydrogen available to etch away all the graphitic sp^2 carbon.⁸¹ Therefore, the ratio of hydrogen to methane is a valuable indicator of the resulting morphology and can be used to finely tune the surface structure.

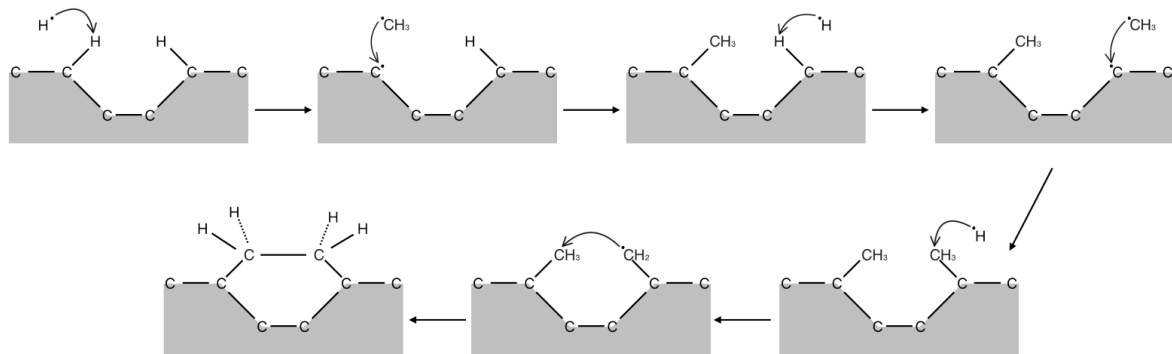


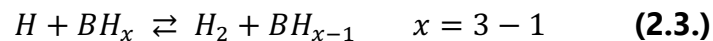
Figure 2.1. Diagram of the reaction for the insertion of carbon at the diamond surface.

An α -parameter can be used to characterise the structure and morphology of the diamond surface produced by HFCVD. The α -parameter is greatly influenced by the gas phase content and is determined by assuming that the growth rates of both $\{100\}$ & $\{111\}$ facets are constant. The growth rates of the two facets will be influenced by the gas phase content and ratio. The α -parameter is determined using **Equation (2.2.)**⁸²

$$\alpha = \sqrt{3} \left(\frac{V_{100}}{V_{111}} \right) \quad (2.2.)$$

2.2.2. $CH_4/H_2/B_2H_6$ Gas-Phase Chemistry

In a $B_2H_6/H_2/CH_4$ gas mixture, various BH_x ($X = 0 \rightarrow 3$) species are formed. The most commonly formed species are B and BH_3 .⁸³ There are many pathways by which boron-containing species can be introduced to the lattice structure. However, these pathways can be separated into three distinct classes (i) Bond cleavage, (ii) Radical abstraction and (iii) Insertion.⁸⁴ When introducing CH_4 , for BDD growth, carbon and boron-containing molecules will have competing reactions, but they may also work together.⁸⁵ BH_x interconversion is shown to play an important role in this process and follows the scheme shown below:



Boron-containing species can be inserted into a $\{100\}$ surface diamond by breaking a C-C bond to form a B-C bond. The indirect mechanism, of insertion, is not favourable due to high energy ring-opening barriers. Whereas the direct pathway only requires the interaction between an empty boron valence p-orbital and a carbon atom. Once the radical species is formed, either by the direct or indirect route, H atom addition will allow for the termination of the radical site.⁸³ This is shown in **Figure 2.2.**

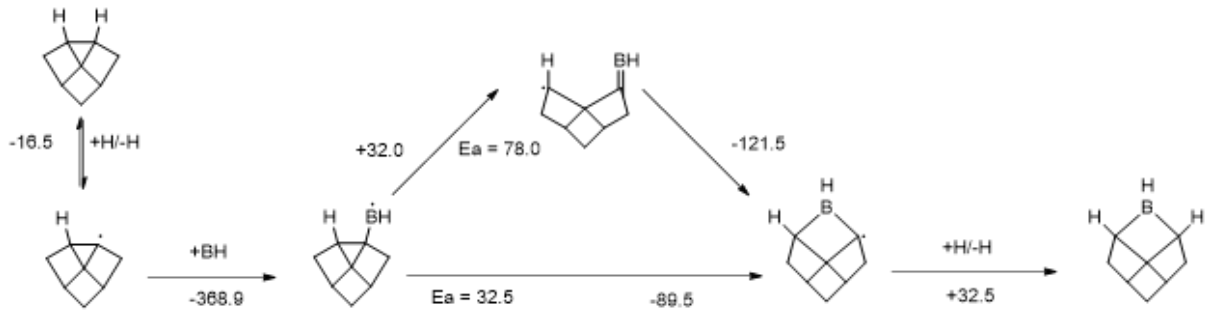


Figure 2.2. Diagram of potential pathways for the insertion of boron into the diamond surface.

2.3. Diamond CVD Techniques

2.3.1. Plasma-Enhanced CVD (PECVD)

Plasma-enhanced Chemical Vapor Deposition (PECVD) involves directing plasma above a substrate within the deposition chamber to induce a "glow discharge". This describes a NIRM-type reactor, shown in **Figure 2.3.**, which employs a waveguide assembly that can control the transmission of microwaves at a frequency of 2.45 GHz. Diamond can be successfully deposited onto the substrate under specific conditions, including CH_4 concentrations ranging from 1% to 3%, microwave power within the range of 300 to 700 W, and temperatures spanning 800 to 1000°C.^{86,87}

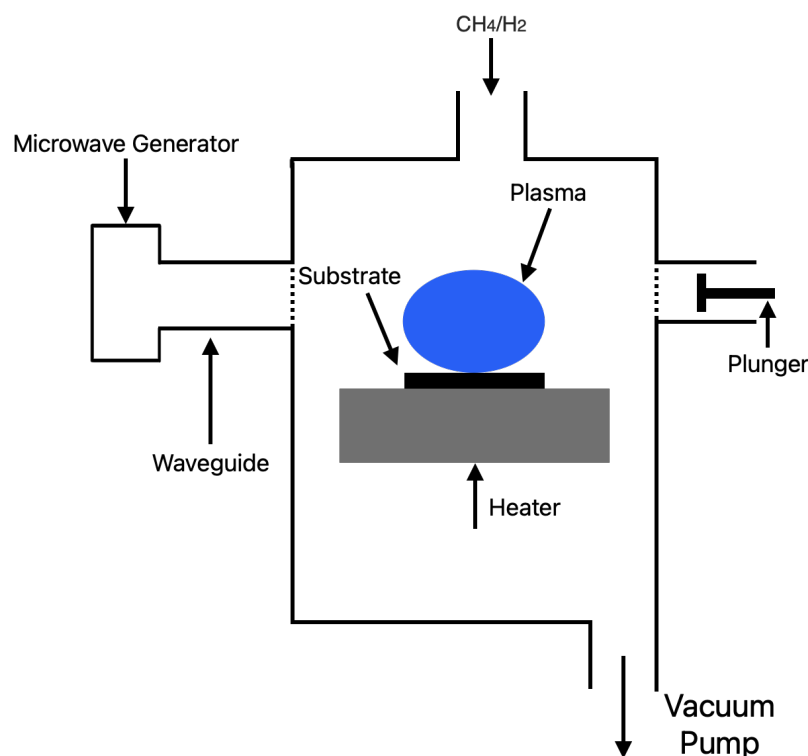


Figure 2.3. Diagram detailing a Microwave Plasma-Enhanced Reactor for Chemical Vapour Deposition.

In the PECVD process, the microwave energy is coupled into electrons, which then collide with gas-phase particles. However, microwave plasma-enhanced CVD reactors are more expensive compared to hot filament CVD reactors, which can limit their application.⁸⁸

2.3.2. Hot Filament CVD (HFCVD)

When a hot filament is placed above the surface of a non-diamond substrate, a diamond film can be deposited. The useful heating temperature ranges from 600 to 1000°C but it is suggested that the actual substrate surface temperature might be higher due to filament radiation.⁸⁹ For this project, a tantalum wire filament is heated to 2000°C and the substrate temperature will be 900°C.

McNeilly and Benzing proposed a reactor that resembles a Hot Filament CVD chamber shown in **Figure 2.4**. It enables the growth of an epitaxial film on a substrate wafer by heating a gas mixture in the reaction chamber. The directed heat confines growth to the substrate, as demonstrated by the growth of epitaxial silicon in their patent.⁹⁰ This work was continued in 1977 with the use of tungsten filament lamps for the uniform heating of primarily silicon substrates. The extent of application for the reactors had been widened to include the epitaxial growth of oxide, nitride, metal and other epitaxial films on substrates such as silicon wafers.⁹¹

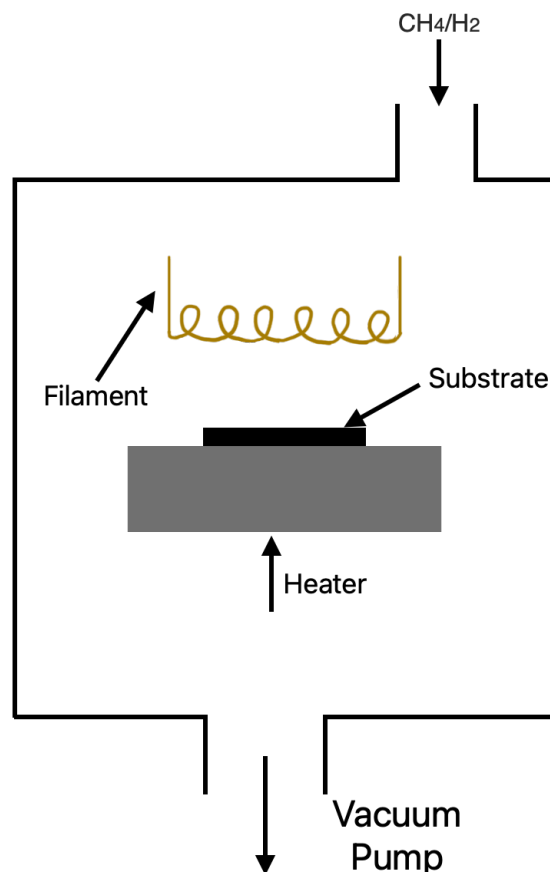


Figure 2.4. Diagram detailing a Hot Filament Reactor for Chemical Vapour Deposition.

2.4. Nanostructured Boron-Doped Diamond

2.4.1. Introduction:

To produce an electrode, with the improved sensitivity and selectivity required for electroanalysis/synthesis, a nanostructured surface can be employed. This nanostructured surface must have an increased surface area in order to improve the capacitance of the electrode nanostructured BDD structures can be produced according to various methods to yield different structures. A simplistic way to categorise these products is Top-down vs Bottom-up growth.

2.4.2. Bottom-up Approach:

2.4.2.1. Nano-cone Structures:

Nano-cone arrays can be produced using a bottom-up approach where Focused Ion Beam (FIB) milling is used to create a free-standing pattern. This is followed by HFCVD to grow free-standing nanostructured diamond films. FIB is an important method as it produces a hole geometry with a high aspect ratio which allows for greater control of diameter, depth and pitch. FIB creates an inverted conical-shaped hole pattern from a silicon mould.⁹²

2.4.2.2. Umbrella Structures:

Umbrella structures are partly inspired by the bottom-up self-assembly structures produced by nature. These natural structures can be used for photonic purposes and this is seen to be the case with the synthetic materials too. This bottom-up approach has been successfully used for polymer structures but faces difficulties with diamond.⁹³ This issue is overcome by introducing a template of silica spheres with a diameter range of 600 to 1000 nm.⁹⁴ The growth of these silicon spheres was based on the method presented by.⁹⁵

A major drawback of the production of nanostructured diamond arrays is that diamonds grow at higher temperatures and high plasma densities than a standard polymer mask can sustain. Instead, the bottom-up structure is formed by growing diamond through a silicon template. This template will limit lateral growth while promoting vertical growth. Once the diamond reaches above the surface of the template it can grow laterally giving rise to the pyramidal shape on top of the final product, shown in **Figure 2.5**.

Lateral growth beneath the surface can be limited by reducing secondary nucleation to accelerate growth only on the exposed diamond top surface. This is made possible by ensuring that a high hydrogen-to-methane ratio is used during HFCVD diamond growth. The research does not cover BDD growth and so it would be interesting to see how adding Boron to the gas mixture would affect the lateral growth aspect and in turn the overall shape of the umbrella structure.⁹³

Due to BH₂ groups terminating on the surface of the diamond, the growth rate will likely be further hindered. This is because termination can lower the rate of nucleation.⁹⁶

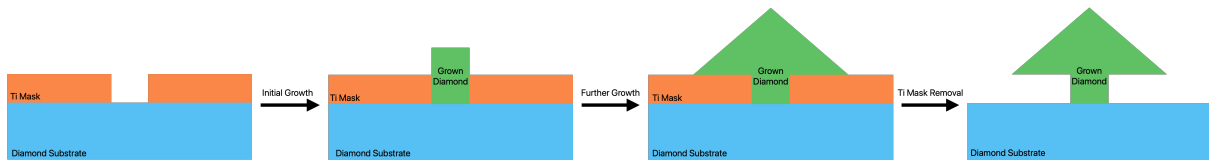


Figure 2.5. Diagram indicating the progressive growth of diamond through a Ti mask on a diamond substrate.

2.4.3. Top-down Approach:

2.4.3.1. Nano-whisker Structures:

Aligned nano-whiskers can possess very sharp tips which allow for defined and uniform emission sites for implementation in field emitter materials.⁹⁷ Initial production utilised sputter etching but this resulted in the random spacing of these structures.⁹⁸

A colloidal technique, where diamond seeds (diameter = 300~nm) were co-suspended with SiC particulates in an aqueous solution, may be applied to produce a pH-controlled method for the coating of SiC-whiskers. HFCVD then provides us with a method to grow dense diamond coatings on the whiskers.⁹⁹

2.4.3.2. Honeycomb Structures:

The fabrication of diamond membranes by plasma etching, using porous anodic aluminium oxide (AAO) masks, allows for control of pore size and depth.¹⁰⁰ A benefit of AAO masks is that the mask does not require any adhesion to the substrate, this is known as non-contact mode. The diamond replicas of the AAO masks may be useful as two-dimensional photonic bandgap structures or the diamond membranes may be used as microporous filters.¹⁰¹ The fabrication process is detailed in **Figure 2.6**.

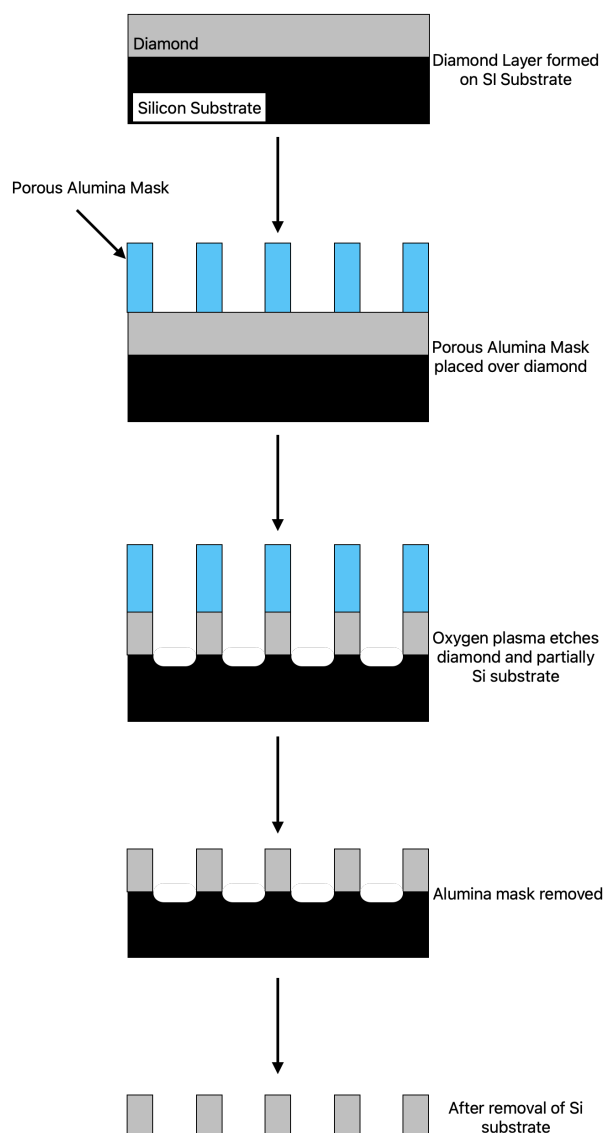


Figure 2.6. Schematic diagram of the diamond honeycomb film production process.

2.4.3.3. Carbon Nanotubes (CNTs) & Teepee-like Structures

Carbon Nanotubes (CNTs) can be coated with diamond, but nucleation can be difficult to initiate simultaneously across the entire length of the tube. A fundamental issue with coating CNTs in diamond is that hydrocarbons are hydrophobic. Therefore, an aqueous colloidal solution cannot be used for seeding. A major drawback to CNTs is the lack of control in their initial fabrication, which makes well-defined periodic arrays hard to fabricate.¹⁰²

Multiwalled carbon nanotubes (MWCNTs) can be produced in dense arrays by using electrospray deposition seeding. The electrospray deposition of diamond seeds causes droplets of methanol to stick to the top surface of the CNTs. This causes several nearby CNTs to collapse inwards on each other to form “teepee-like” structures, which can be seen in **Figure 2.7**. It is suggested that inward collapse could be attributed to electrostatic attractions. The purpose of this method is to produce a thin coating of diamond over the CNTs without embedding the CNTs with diamond. Multi-walled CNTs can be more desirable

than single-walled CNTs due to their greater resilience to etching caused by the CVD process.¹⁰³

The CNT-like structures can be improved with a Fe catalyst and further cooling to ambient temperature under a pure hydrogen flow, without pumping the residual methane out. This alters the pre-existing CNT growth process.¹⁰⁴

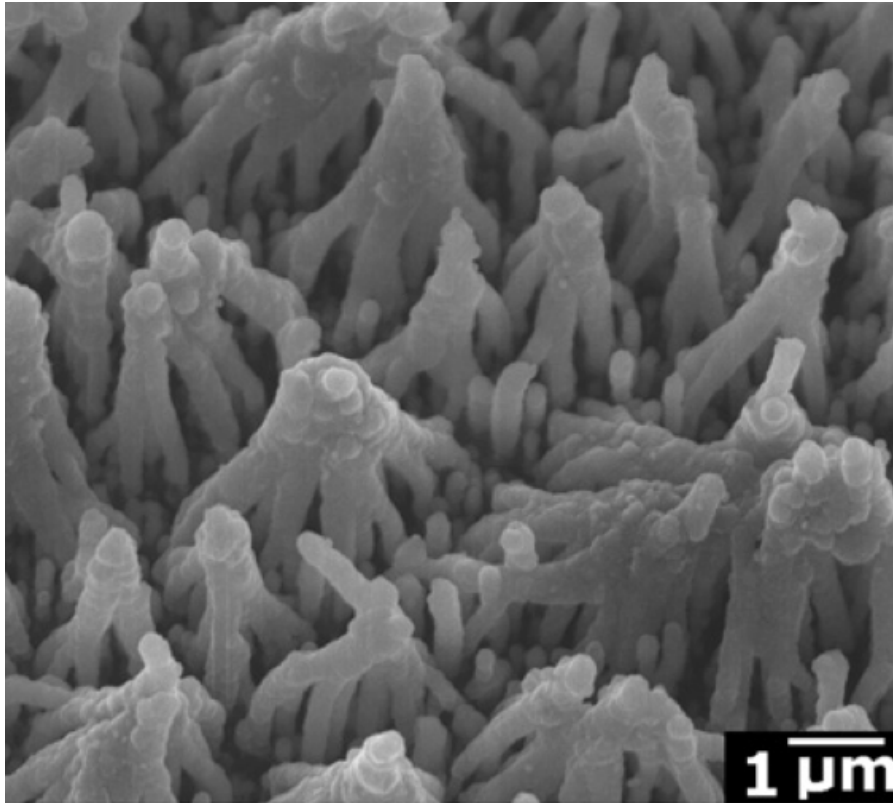


Figure 2.7. SEM image of teepee-like nanostructured diamond. Image taken from Reference 103.

2.4.3.4. Nanotip Structures:

This approach, shown in **Figure 2.8.**, relies upon a micellar approach where a diblock copolymer (di-BCP) is dissolved in toluene. HAuCl_4 is then incorporated into the mixture. The diamond substrate is dipped into the solution and pulled out at a specific velocity. This velocity will dictate the order of the gold-salt-loaded micelle monolayer. These macromolecules are self-ordered into arrays, determined by the removal velocity, that act as a precursor to the mask for the final pattern. The polymer is then removed by an isotropic oxygen plasma to leave evenly spaced gold nanoparticles. This spacing can be controlled by the velocity at which the substrate is lifted from the solution. The Au mask is then etched away using RIE to leave the nanotips.^{105,106}

An alternative, to dip-coating the hydrophobic block co-polymer, is spin-coating the BCP onto the surface of the substrate, with the BCP spreading due to centrifugal forces. The Silicon nanotips produced may then be coated in BDD which may prove useful in the production of sharper pointed BDD structures.¹⁰⁷

This method is a combination of the top-down approach of etching with the bottom-up approach of self-assembly. Self-assembly BCP chemistry is not limited to just nanotips as periodic domains can also be produced with spherical, gyroid or cylinder shapes. Top-down lithography of these BCPs is limited below the 22 nm half-pitch limit and is rather expensive.¹⁰⁸

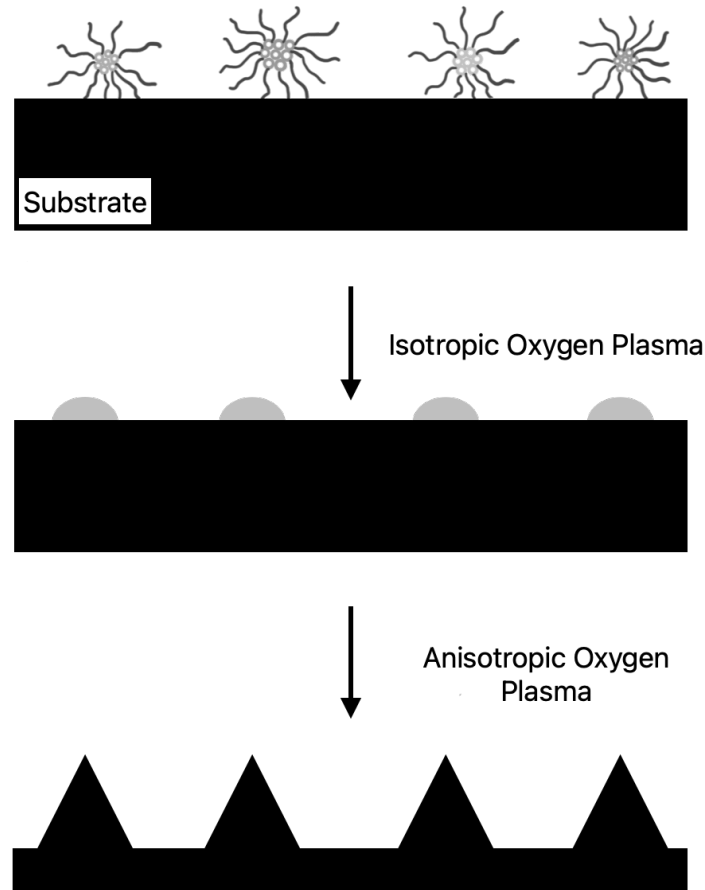


Figure 2.8. Diagram showing the basic principles of using micellar masks to produce diamond nanotips.

2.4.3.5. Black Silicon (bSi) Structures for Black Diamond (bD)

High surface area substrates, called black silicon (bSi), can be fabricated to improve the sensitivity of the resulting electrode. For this project, these nanostructures were purchased (TOM KAMP). The material is known as black silicon because the dense nanostructured surface increases the absorption of light while decreasing reflectivity. These surfaces are produced using a Reactive Ion Etching (RIE) technique in cooperation with the deposition of micro masks. The needle density can be changed by controlling the gas-phase composition, temperature and substrate bias. These factors will alter the coverage of a surface passivation layer, which acts like a mask. Further etching results in the formation of high aspect ratio randomly placed nanostructured needles.¹⁰⁹

bSi nanostructures can then be coated in diamond using the CVD technique to produce black diamond (bD), as shown in **Figures 2.9. & 2.10.** It has been shown that the capacitance value of bD electrodes can be around $280 \mu\text{F cm}^{-2}$ compared to an f-BDD electrode which has a double-layer capacitance of roughly $5 \mu\text{F cm}^{-2}$.¹¹⁰

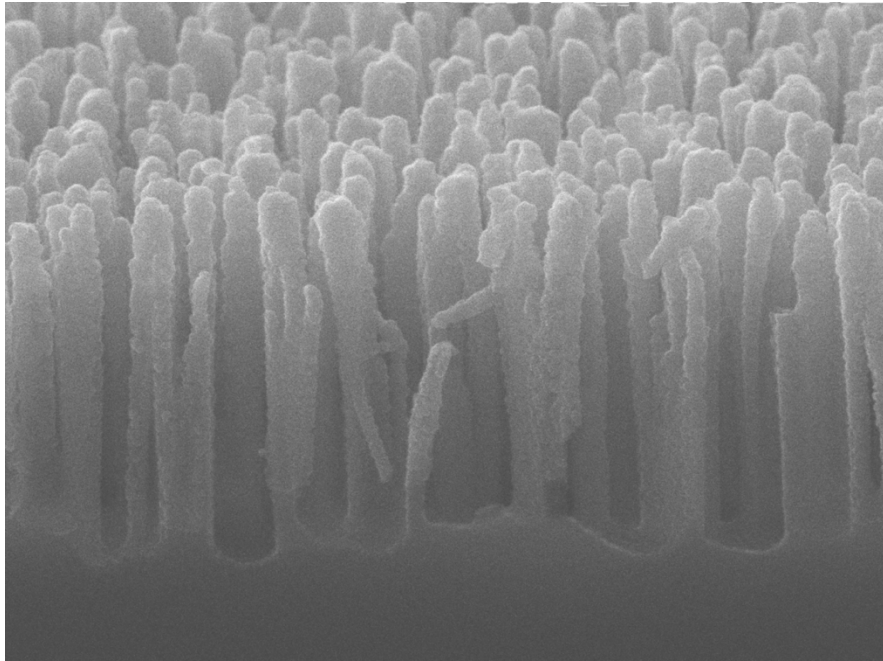


Figure 2.9. MM32 Side View After 40 Minutes BDD Deposition

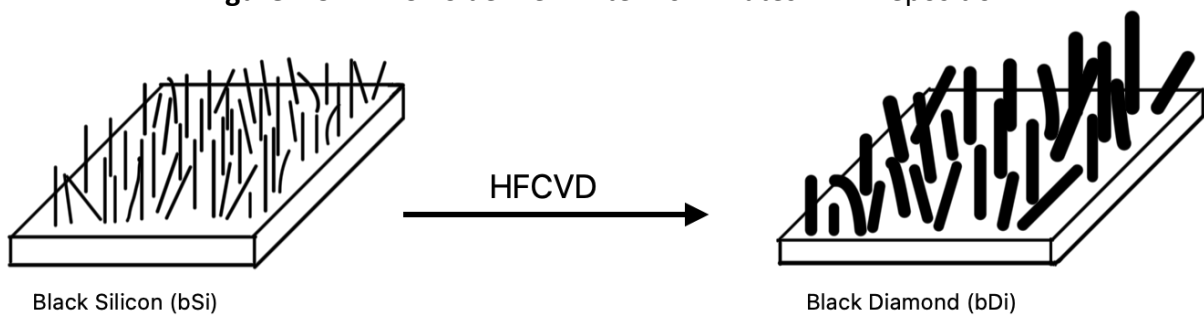


Figure 2.10. Diagram showing black silicon (bSi) needles coated by HFCVD and forming black diamond (bD).

2.4.3.6. Electron Beam Lithography Columns

Electron beam lithography (EBL) is a “direct writing technique” where good pattern definition of the silicon substrate can be produced. The desired pattern is applied to the surface of the resist to produce either a negative or a positive resist pattern. However, EBL is both expensive and time-consuming and so is often overlooked when considering the mass production of samples.¹¹¹

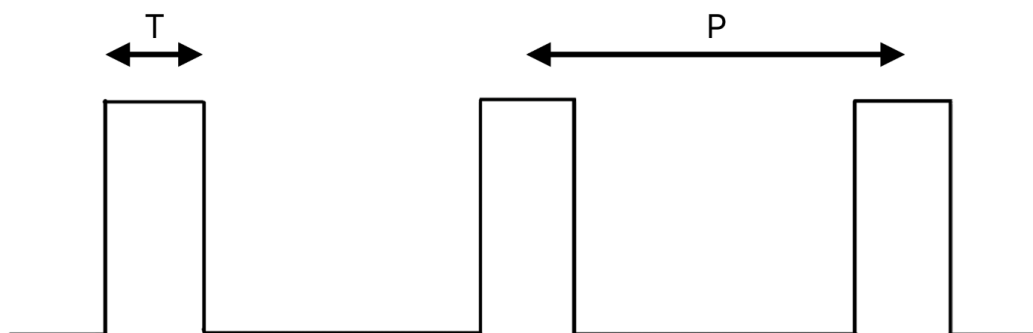


Figure 2.11. Diagram showing the spacing of columns in EBL. T = Thickness, P = Pitch.

EBL requires that the resist material, that coats the substrate, can be chemically or physically altered by the energetic absorption of electrons directed at the resist with an electron beam. The change in structure of the exposed resist is what will define the mask that covers the resist. For a positive resist, the region exposed to the focused electron beam is removed by a solution during the development stage.¹¹² In this report, the resist pattern and uncovered substrate beneath are then coated in a thin layer of metal by thermal evaporation. A process called selective lift-off is then implemented, where the metal layer and resist are removed but the metal covering the substrate remains.¹¹³ This process is shown in **Figure 2.12.** and defines the mask for the Reactive Ion Etching (RIE) process, shown in **Figure 2.13.**

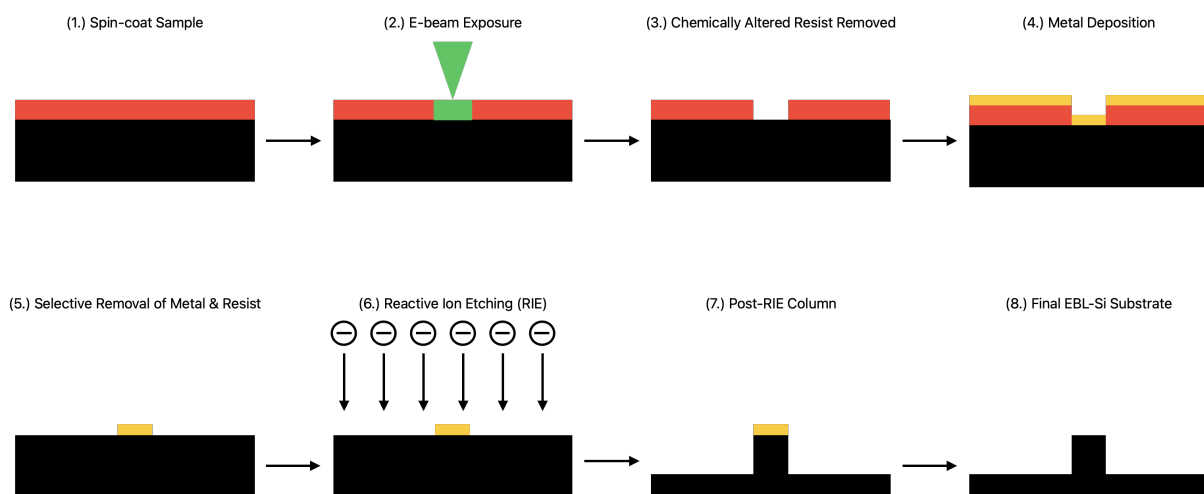


Figure 2.12. The process of electron-beam lithography is shown as well as reactive ion etching. The final product is shown to have a definable T and P value.

RIE was chosen for our etching process as it can combine beneficial aspects of both physical and chemical techniques. This makes RIE a highly anisotropic method with very little lateral etching. In RIE, reactive species are adsorbed onto the surface of the material that is to be etched. After reacting with the surface layer of the substrate, the product is desorbed from the surface and pumped out of the reaction chamber. For this reason, the products of the etching process must be in the gas phase, as shown in **Figure 2.14.**¹¹⁴

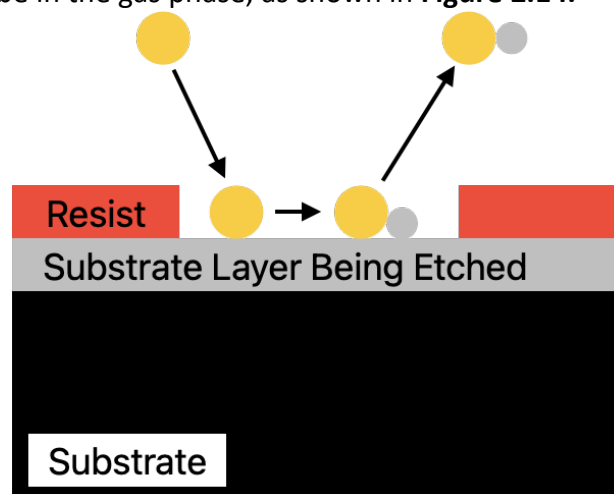


Figure 2.13. Diagram showing the process of Reactive Ion Etching.

2.5. Diamond Nucleation Techniques

2.5.1. Heterogeneous Nucleation – Surface Nucleation

2.5.1.1. Mechanical Abrasion-enhanced Nucleation

Initial studies of diamond grown on non-diamond substrates found that the nucleation density was low but also varied depending on the conditions of the substrate. For example, favourable growth is observed along scratches in the substrate surface.¹¹⁵ Scanning Tunnelling Microscopy (STM) shows that lateral growth of nuclei keeps to the surface and that precursors to possible intergrowth of nuclei are found on the surface.¹¹⁶ Nucleation of diamond can be inhibited by a surface oxide layer on the substrate.¹¹⁷

The addition of water into the gas mixture can aid in methane decomposition as excited electrons in the plasma can dissociate the hydrogen and water into H and OH radicals. These radicals then decompose methane into CH₃, CH₂ and CH radicals. Graphite is removed from the surface at a faster rate than diamond because it is far more reactive towards the H and OH radicals than diamond is.¹¹⁸

2.5.1.2. Ion Implantation-enhanced Nucleation

Si⁺ ion implantation increases the surface energy of the Si substrate due to atomic displacement. This reduces the surface energy difference between the Si wafer and the diamond film, enhancing nucleation. Ion implantation preferentially produces diamond precursors, such as silicon carbide, that can improve nucleation rates. Ion implantation is said to be preferable to scratching in that there is less effect on surface morphology.¹¹⁹

Ar⁺ ion implantation was shown to produce small changes to the surface morphology.¹²⁰ Ion implantation improves nucleation by producing nanostructured surface defects which can by themselves be of help in increasing nucleation rates.¹²¹

2.5.1.3. Low Gas Pressure Nucleation

At very low pressure (0.1 Torr = 13.33 Pa) the nucleation density is very high (10¹⁰ – 10¹¹ nuclei cm⁻²). This trend continues at moderately low pressures (1 Torr = 133.32 Pa) where the growth rate may also be high. It is suggested that this is the case because, at decreased pressures, the active species undergo fewer collisions. This means that the active species will lose less energy during movement to the substrate.¹²²

2.5.1.4. Bias-enhanced Nucleation (BEN)

Negative biasing of a silicon substrate can improve nucleation density on a non-scratched silicon surface by increasing the number of nucleation promoters like SiC.¹²³ Continued BEN can lead to secondary nucleation and/or twinning. Twinning and secondary nucleation can eliminate diamond growth orientation with respect to the substrate due to the nanocrystal diamonds growing on the surface. Therefore, prolonged BEN can have a negative impact on the final product.¹²⁴

Figure 2.14. highlights that, when a bias is applied, a plasma ball forms above the surface, as well as a secondary plasma “sheath” that lies 1mm above the surface of the substrate. This sheath aids in the attraction of diamond nuclei that have been scattered, which then furthers growth of nanocrystalline diamond. This growth helps move the plasma “sheath” across the surface, due to attraction of the bulk, advancing nucleation even further, this can be seen in **Figure 2.14.**¹²⁵

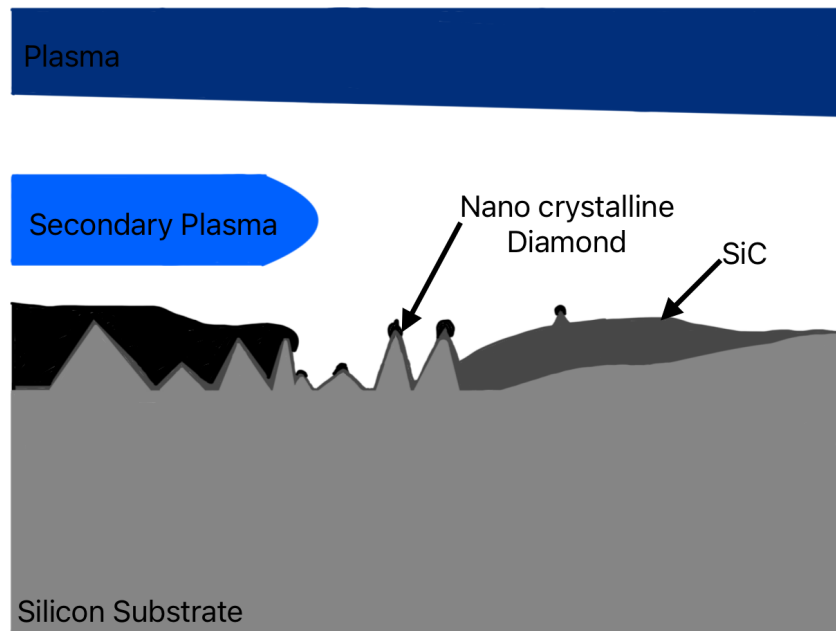


Figure 2.14. Bias-enhanced Nucleation (BEN) and diamond deposition across a Si substrate.

A constant bias level of negative d.c. $\sim 250\text{V}$ produces good nucleation values in PECVD. Again, negative biasing may be preferable over scratching as it does not have as large effect on surface structure. BEN is performed in the same chamber, under the same vacuum conditions, as the CVD diamond growth process. This removes the need for cleaning of the surface.¹²⁶

2.5.2. Homogeneous Nucleation – Gas Phase Nucleation

Homogeneous nucleation or homoepitaxy of diamond is the growth of diamond films on diamond substrates. Homogeneous nucleation is hindered by the graphitisation of the surface. Growth on diamond seeds, which is done using methane pyrolysis, is very slow (1nm/hr) and improved growth rates are only achievable on non-diamond substrates. Growing on non-diamond substrates also aids in avoiding graphite deposition.^{127,73}

2.6. Nanodiamond Seeding

2.6.1. Introduction

Seeding is an important step for the coating of substrates, such as Silicon. It cannot rightfully be described as a nucleation technique, due to the growth of diamond beginning on pre-deposited nanodiamond particles. High seed density, for a monolayer, is achieved when seeds are packed together in a hexagonal manner. This model assumes that each seed is

perfectly spherical. Another important assumption, displayed in **Figure 2.15.**, is that it is presumed that all nanodiamond seeds are of the same diameter.¹²⁸

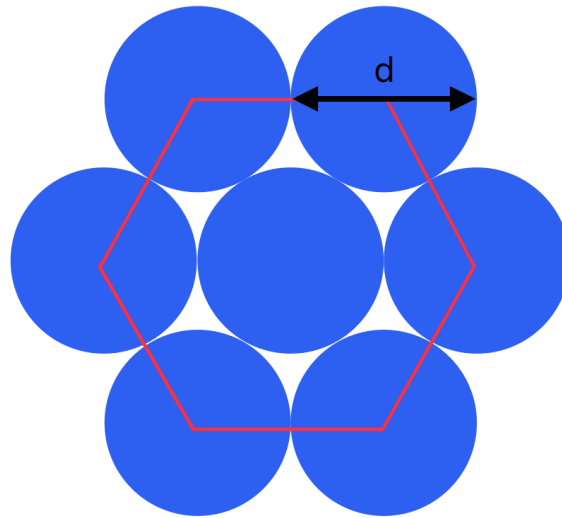


Figure 2.15. The diagram depicts a high seed density in a hexagonal formation.

2.6.2. Surface Charge

Detonation Nanodiamonds (DNDs) have been shown to have particularly notable colloidal behaviour. Dispersion of DNDs into water using high-power ultrasound produces a monodisperse solution. DND colloids result in a highly positive zeta-potential and an improved colloidal stability, due to dispersion, over a broad pH range.¹²⁹ Greater control of the surface charge of nanodiamonds allows for the manipulation of the zeta potential. This is important for controlling film growth, due to the colloidal stability.¹³⁰ An example is that diamond films can be grown on WC-Co surfaces using nanodiamond solutions with a colloidal aggregation that was controlled by the addition of NaOH or HCl. This addition alters the desired pH and aggregation can be increased for positively charged nanodiamonds.¹³¹

2.6.3. Solvent Choice

The solvent choice for the suspension of nanodiamonds must also be considered greatly when it comes to improving the state of the colloid and its aggregation. By controlling this parameter, it is possible to improve dense and consistent seeding for thin film growth. A solvent with beneficial qualities will have: i) A low surface tension ii) near-zero dipole moment iii) low density iv) low viscosity and v) high vapour pressure. The most valuable properties in the pursuit of de-aggregation are the dipole moment and high vapour pressure. When silicon is used as the substrate, n-hexane, n-pentane and methanol are suitable choices for homogeneous seeding.¹³²

2.6.4. Nanodiamond Seeding Techniques

2.6.4.1. Mechanical Abrasion Seeding

Diamond fragments that lie within the scratched grooving of the Si allow for the preferential growth of diamond.¹³³ However, the increased nucleation rate, post-scratching, cannot only be attributed to the diamond residue on the scratched surface. Most of this residue is

incorporated into transitional layers that are not believed to be substantial enough to explain the increased nucleation rate.¹³⁴

Nanoscale scratches can be caused by ultrasonic abrasion to increase nucleation rates with nanodiamond suspensions. This complicates the matter as it is harder to determine whether scratching caused by the process is what's increasing the nucleation rate or if it is the implantation of diamond nanoparticles.¹³⁵

Mono-disperse slurries constituting larger diameter nanoparticles result in higher nucleation rates because larger particles, that collide with the surface, fragment into small diamond debris that is inserted into the surface. Large particles have greater momentum and so are more capable of “hammering” the surface, compared to small particles.¹³⁶

2.6.4.2. Suspension Evaporation Seeding

Droplets of nanodiamond suspension are applied to a substrate and the solvent is evaporated. DMSO is a useful solvent for detonation nanodiamonds (DNDs) as DMSO helps prevent agglomeration of the colloidal suspension for up to a year. Seeding can be performed uniformly when DMSO/Alcohol seed suspensions are dried upon a substrate. This is an improvement over deionised water which is known to promote agglomeration when dried.¹³⁷

Spin-coating is an alternative method for uniform nanodiamond distribution across a flat substrate surface. It is a sol-gel technique where the diamond colloid is applied to the surface and spin-coated to produce the desired uniform film of diamond seeds.¹³⁸

2.6.4.3. Electrostatic Self-Assembly Seeding

For electrostatic Self-Assembly seeding, the subsequent growth of diamond upon this seeding by CVD initially follows the Volmer-Webb growth mechanism. This is indicative of a circumstance where adsorbed atoms interact more intensely with each other than they do with the substrate. Clusters begin to form which proceed to grow leading to a rough surface forming.¹³⁹ Van der Drift suggested a “survival of the fastest” growth mechanism which has been shown to take over from the previous model once the clusters are large enough. Crystals that grow the fastest perpendicular to the substrate will become dominant and those that grow with a greater lateral component will not be preferred.¹⁴⁰

It is possible to alter the electrostatic attraction of the particles by solution pH and functional groups. Nanodiamond colloids are believed to be stable at a pH above 4 when the zeta-potential magnitude is greater than 30mV, below this potential DNDs will form aggregates. Surface functionalisation can also be used to control ND seeding densities. Colloidal properties of the DNDs are suppressed by the reduction of oxygen containing surface groups. An example of the impact of surface functionalisation on seeding density is that silicon dioxide surfaces are repulsive to nanodiamonds.¹⁴¹

Chapter 3 – Characterisation Techniques

3.1. Scanning Electron Microscopy (SEM)

Scanning Electron Microscopy (SEM) provides the user with an image of a sample with a high level of spatial and visual resolution, primarily used to determine features on the surface of a material. SEM is used to detect scattered electrons that are emitted by the surface of a material. This is where primary electrons fired at a surface are absorbed by surface atomic electrons which then release secondary electrons. The detection of these secondary electrons will be used to form an image of the surface.¹⁴²

3.2. Energy Dispersive X-ray Spectroscopy (EDX)

Energy-dispersive X-ray (EDX) analysis is a technique that can be used to determine the elemental composition of nanostructures by SEM. In this technique, X-rays are generated from the sample by the electron beam of the Scanning Electron Microscope (SEM) and then analysed by the EDX spectrophotometer that is built into the SEM. The generated X-rays that are produced by this process will have energies that correspond to specific elements in the sample. It is also possible to determine the concentration of each element in the sample.¹⁴³ This can be represented in the format shown in **Figure 3.2**.¹⁴⁴

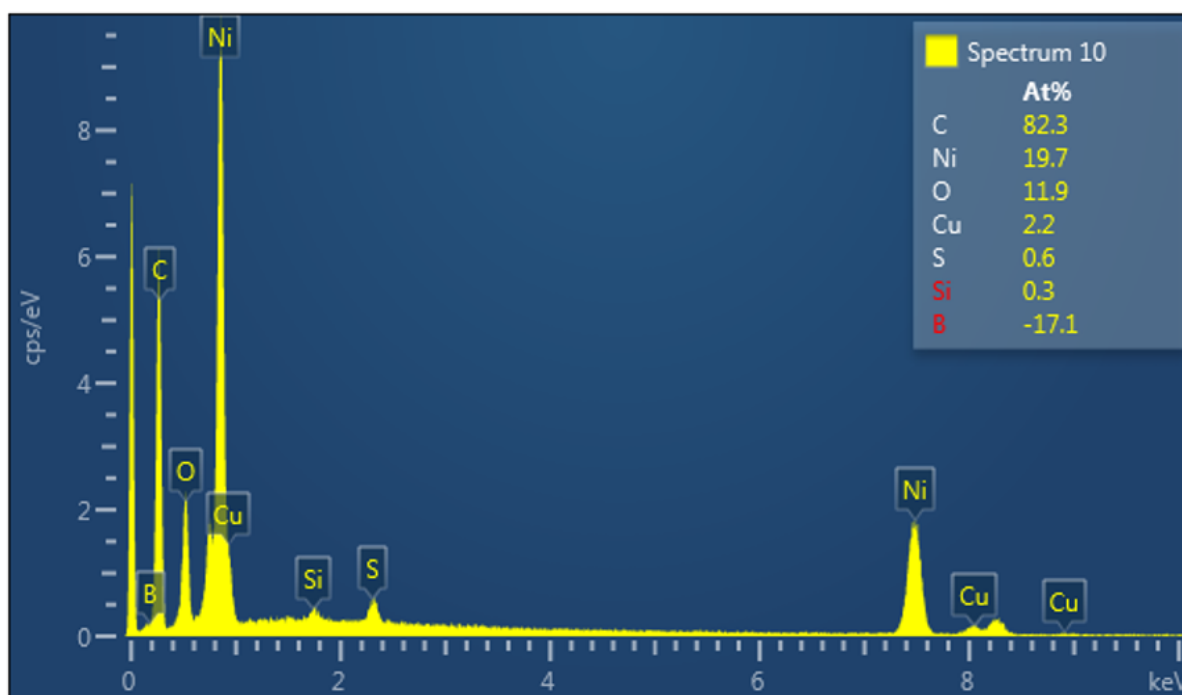


Figure 3.2. Example Energy Dispersive Spectrum (EDX Spectrum 10) of an f-BDD electrode after nickel deposition.

3.3. Raman Spectroscopy

Raman Spectroscopy is a non-destructive spectroscopic technique. The Raman shift is the energy gap between the incident photon and the departing photon. The Raman band is produced by light scattered by a crystal lattice or molecule's vibrational modes. Whereas

infrared (IR) absorbance occurs when there is a direct equivalence between the energy of the incident photon and the energy gap between two electronic energy levels.

Scattering will occur where there is no direct equivalence between the incident photon energy and the energy gap between two electronic energy levels. For scattering to occur, the electron cloud of a crystal lattice will be distorted and the polarisation will change, due to the formation of a virtual state. This transient virtual state, which is produced by scattering, decays and a photon departs. Scattering can be either elastic (Rayleigh) or non-elastic (Stokes). Anti-Stokes scattering will occur when the energy of the outgoing photon is higher than that of the incident photon.¹⁴⁵ This difference can be seen in **Figure 3.1**.

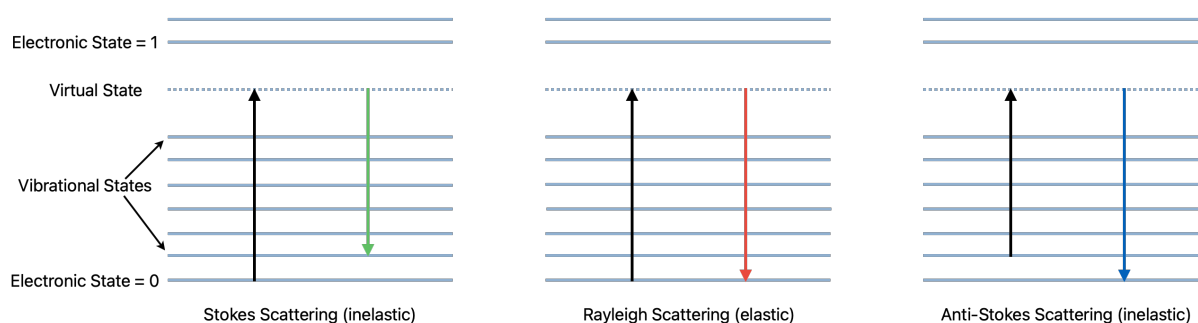


Figure 3.1. Energy Diagram Showing Rayleigh, Raman Stokes and anti-Stokes related transitions.

3.4. Cyclic Voltammetry

3.4.1. Nernst Equation

This is an important analytical method that can determine redox potentials for electrochemical processes. Fundamentally, an understanding of the Nernst Equation is required. Here, the potential of an electrochemical cell (E) is related to the standard potential of a species (E^0). The relative activities of the oxidised (Ox) and reduced (Red) analytes are necessary factors that must also be considered:

$$E = E^0 + \frac{RT}{nF} \ln \frac{OX}{RED} = E^0 + 2.3026 \frac{RT}{nF} \log_{10} \frac{OX}{RED} \quad (3.1.)$$

When [Ox] is scanned negatively it is reduced to [Red] at the electrode. The “duck-like” shape of the classical CV, shown in **Figure 3.2.**, is the result of plotting the current at the working potential against the applied voltage. Therefore, the depletion of (Ox) at the electrode allows for the measurement of a current in the form of a cyclic voltammogram.

Scanning cathodically from point A to D (A-->D) results in the concentration of the oxidised form being reduced to [RED]. Point C indicates when the peak cathodic current ($i_{p,c}$) is seen. This current is affected by the diffusion of [OX] from the bulk solution. The current is expected to decrease as the scan progresses (C-->D) due to diffusion from the bulk decreasing as mass transport of (Ox) to the electrode is slowed.¹⁴⁶

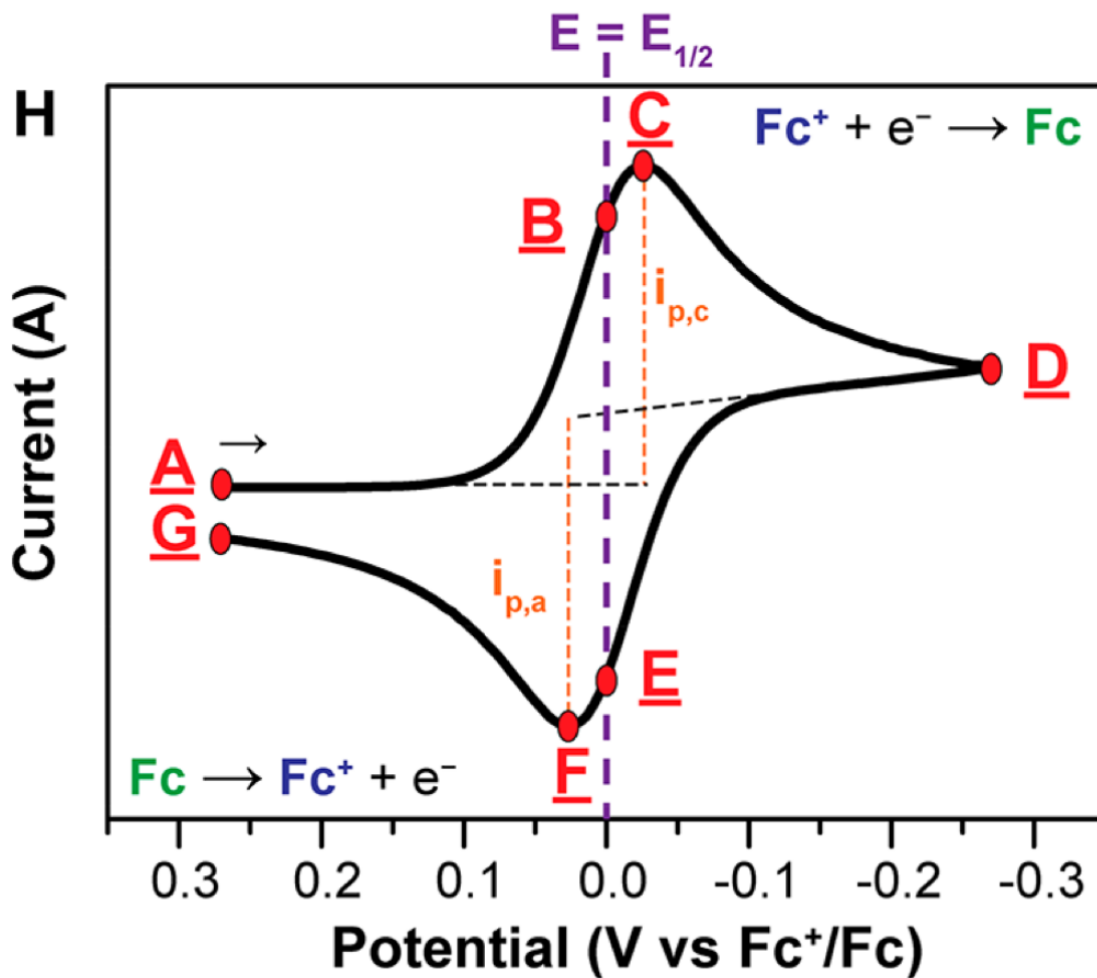


Figure 3.2. Cyclic Voltammogram of the reversible reduction for 1mM Fc^+ solution to Fc , Scan Rate (v) = 100mV/s. Figure taken from Reference 146.

3.4.2. Capacitance

The capacitance of the double layer (C_{dl}) can be determined by plotting the capacitive current (i_c) versus the scan rate (v). The gradient of the plotted straight line will be the double-layer capacitance as:

$$i_c = C_{dl}v \quad (3.3.)$$

Alternatively, the capacitance can be determined by averaging the current at $V = 0$ and using the area of the electrodes exposed window:

$$C_{dl} = \frac{i_{av}}{vA_{Geometric}} \quad (3.4.)$$

C_{dl} is the double-layer capacitance, i_{av} is the average current from forward and reverse sweeps at 0V, v is the scan rate and $A_{Geometric}$ is the area of the exposed window for the electrode.¹⁴⁸

3.4.3. Surface Area Calculations

We assume that for f-BDD $A_{\text{Effective}}$ is positively correlated to $A_{\text{Geometric}}$ and A_{Actual} . By making this assumption, the C_{dl} of f-BDD can be determined using the area of the electrode's exposed window, as the scan rate and average current are already known. We can then determine the C_{dl} of the bD & EBL-BDD samples using their $A_{\text{Geometric}}$ values as well. Finally, to find the relative increase in surface area between f-BDD and either bD or EBL-BDD we take $C_{\text{dl(EBL-BDD)}} / C_{\text{dl(f-BDD)}}$. This can be used to find the electrodes $A_{\text{Effective}}$ as the increase in capacitance is proportional to the increase in $A_{\text{Effective}}$.¹⁴⁹

$A_{\text{Effective}}$ is the useful surface area of the electrode, calculated from the capacitance. A_{Actual} is the pre-determined design area of the electrode, for EBL-BDD we sum the surface area of the flat electrode and all the column's curved areas together. $A_{\text{Geometric}}$ is the area of the exposed window of the electrode holder. This can be seen in **Equation 5.1**.

A high $A_{\text{Effective}} / A_{\text{Actual}}$ ratio will indicate that a greater proportion of the surface area is being used for electrochemical purposes. A small value would indicate that much of the surface is not available for reactions to proceed, indicating that there is an underlying issue present within the process.

Chapter 4 – Experimental

4.1. BDD Sample Preparation

4.1.1. Wafer Cutting:

f-BDD and EBL-BDD substrates were produced by first cutting 10 x 10mm samples of highly conductive Si wafers with a laser cutter. The laser cutter etched the desired pattern and the individual wafers were then forced apart by hand.

Prefabricated sheets of bSi wafers were provided by Lam Technology. These were then cut down to a scale of 10 x 10mm with a laser cutter.

4.1.2. EBL Etching of Si Wafer:

EBL was performed on the wafers to produce a microstructured conductive silicon structure for EBL-BDD products. This process ensured that a set design was etched onto the surface of the Si wafers. This meant controlling the column thickness (T) and the pitch (P). This meant that the minimum pitch would be $P_{\text{Min}} = 3 \times T$ to allow for uniform BDD coverage later. After deliberating on the optimum T & P values for greater surface area, two options seemed most viable:

1. T = 200 nm P = 600 nm
2. T = 200 nm P = 1000 nm

4.1.3. Nanodiamond Seeding:

For f-BDD, a small sample of nanodiamond was applied to the surface of a 10 x 10mm conductive Si wafer. Two wafers were then rubbed together until their surfaces became dull and a microstructured surface had been produced.

bSi-BDD samples required a different method for seeding, to prevent damage to the nanostructure. Therefore, a diamond seed solution was produced where 10 drops of nanodiamond solution were pipetted into a vial. This was then diluted by filling the vial to 90% with methanol. Sonication of the suspension was then performed for 3Hrs.

A third of the solution was then added to a petri dish and the bSi sample was dipped into this solution for 1Hr. This sample was then air-dried for 30 minutes. The process was repeated twice to ensure total uniform coverage.

4.1.4. HFCVD:

Two Si wafers were placed in the HFCVD reactor with a gas mixture containing: H₂ (200sccm), CH₄ (2sccm) & B₂H₆ (0.67sccm). Three tantalum filaments (99.9% ADVENT Research Materials Ltd) were placed 3 mm above the surface of the substrate. The process was performed for 30 minutes to coat the substrate in a polycrystalline BDD film. Once the film had been formed, CH₄ & B₂H₆ were removed from the system and H₂ was allowed to remain for a further two minutes. This resulted in an H-terminated surface. The deposition process was performed at 25 Torr and 2000°C in all cases with an applied current of 25A.

4.2. Electrode Preparation

4.2.1. f-BDD Electrode Preparation

f-BDD was analysed using a holder specially designed for this purpose. The sample holder consisted of a front face, back-plate and a conductive arm. The front face had a circular hole cut into the centre which allowed for contact between solution and BDD sample. The f-BDD samples were held in place by a copper back-plate. The connection between the copper back-plate and the back of the BDD sample was held in place using gallium-indium eutectic. The back-plate and front face were screwed together with minimal force, to prevent sample cracking under pressure. The conductive arm was then screwed into place and the join between the arm and main body of the sample holder was covered using PTFE tape, to prevent solution leaking in. The sample holder design was provided by A. Black and is shown in **Figure 4.1**.



Figure 4.1. The electrode holder for f-BDD and EBL-BDD samples. The sample being held here is an f-BDD sample.

4.2.2. bSi Electrode Preparation

Due to the bSi substrate not being conductive, an alternative approach was employed that better suited the arrangement of the electrode. For bSi, the wire connected to the sample must be joined on the conductive bD side of the sample. Teflon tape was used to cover the surface of the sample, ensuring a 7.00mm² window was left uncovered. A corner of the surface was left uncovered to allow for a connection to be made with the potentiostat.

Silver paint was used as the conductive adhesive that made the connection possible. Sample preparation was completed with the aid of A. Black.

4.3. Electrochemical Analysis

4.3.1. Cyclic Voltammetry for H-terminated Samples

f-BDD and bD-BDD electrodes were both analysed electrochemically by cyclic voltammetry using two different solutions: (i) KNO_3 100mM in 100ml of DI water and (ii) $\text{Ru}(\text{NH}_3)_6$ (1mM) and KCl (100mM) in 100ml of DI water. 100ml of solution (i) or (ii) was transferred to a three-electrode electrochemical cell and degassed with Argon for 15 minutes. The working electrode (diamond sample), reference electrode (Ag/AgCl) and counter electrode (KCl) were all put in their respective positions. The working electrode was moved up and down to remove bubbles from the sample holder used to analyse f-BDD. It is important to ensure the sample holder is air-tight to prevent solution interference. Measurements were then taken using a μ Autolab Type III potentiostat at room temperature (RT).

4.3.2. Ozone Treatment for O-Terminated CV Analysis

After Cyclic Voltammetry was performed on the H-terminated samples, the samples were O-terminated by ozone treatment. This was performed using the Jetlight UVO Cleaner for 25 mins. CV analysis was done on the O-terminated f-BDD samples in the same manner as for H-terminated f-BDD samples.

4.4. Electrodeposition & Dealloying

4.4.1. Electrodeposition

f-BDD and bD-BDD electrodes were individually coated with nickel using an electrodeposition process with a solution containing NiSO_4 (0.2M), CuSO_4 (0.01M) and H_3BO_3 (0.5M) that was made up to 100ml. The solution was degassed for 15 minutes with Argon in a three-electrode electrochemical cell. The working electrode (diamond sample), reference electrode (Ag/AgCl) and counter electrode (KCl) were all put in their respective positions. bD-BDD had an exposed window area of 7.00mm^2 and f-BDD had an exposed window area of 50.27mm^2 , since the diameter of the electrode holder is 8 mm. Deposition of the Ni-Cu alloy was performed in a manner that limited the total cathodic charge (deposition charge) to 1 C cm^{-2} where time could be varied to achieve this. The Ni-Cu alloy was deposited with a ratio of 1:1, which was made possible by performing co-deposition at a constant potential of -0.85V . See **Figure 4.2.** for more details on the set-up.

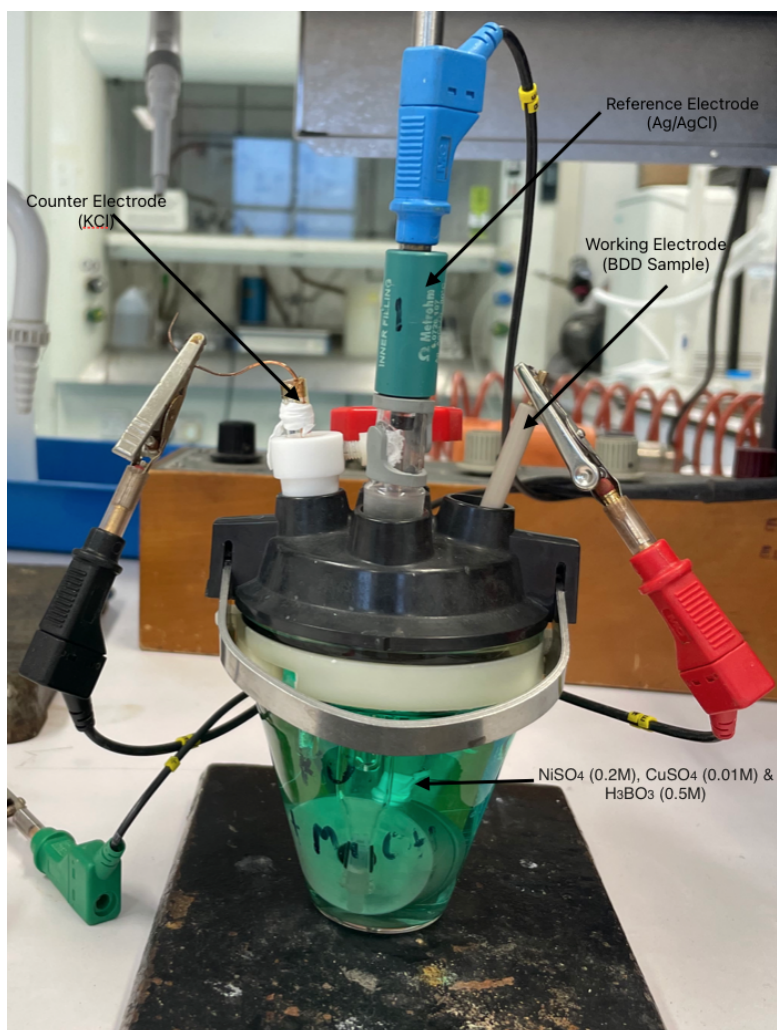


Figure 4.2. Three-electrode set-up for cyclic voltammetry and nickel/copper alloy deposition and dealloying.

4.4.2. Dealloying

Dealloying was performed in the same solution as electrodeposition with the same μ Autolab Type III potentiostat used for CV work done previously at RT. This was done immediately after the deposition process. The selective dissolution of Cu was performed at -0.5V

4.5. Scanning Electron Microscopy (SEM)

All BDD sample (f-, bD- & EBL-Si) images were obtained using the JEOL JSM 5600LV system. Side-profile images were taken when samples were cut to a smaller scale and secured to the sample-holder plate.

Chapter 5 Results & Discussion

5.1. Scanning Electron Microscopy (SEM)

5.1.1. EBL-Si Substrate Fabrication

5.1.1.1. Post-deposition Pattern Definition

It is believed that to adequately coat the Si columns with BDD while also ensuring good pattern definition, the Pitch must be 3x the T value. **Figure 5.1. (a)** shows an example of when the pitch is not large enough to accommodate the BDD coating process. In this example, the definition of the pattern has been negatively affected, with the columns beginning to form a continuous layer, due to the over-growth of diamond. This is expected to reduce the effective surface area of the electrode, as the solution cannot penetrate the spacing between the columns and utilise the base area of the columns. Over-growth can be mitigated by (i) adequately spacing the columns, by increasing the pitch value, (ii) decreasing the thickness (T) of the columns or (iii) depositing a thinner layer of BDD onto the Si substrates by reducing deposition time.

The second approach is observed in **Figure 5.1. (b)** where T is reduced and HFCVD conditions are maintained the same.

When T is reduced from 220 to 160 the separation of the columns improves. However, a drawback of this approach is that the survivability of the individual columns is reduced. This is evident in the presence of chipped and missing columns. Due to the reduced survivability of columns where $T < 200\text{nm}$, it is suggested that $T = 200$ is currently the smallest diameter for successful electrode fabrication. Therefore, $P = 600$ is recommended as the smallest pitch value.

The final approach is viable but may result in individual columns not being fully coated, especially columns within the central bulk of the electrode. This was observed for dense bD-BDD samples which had short HFCVD deposition times, as seen in **Figure 5.2**. In this instance, not only did the bases not coat fully but the tops grew wider, creating a “baseball bat” like shape. This is likely because the deposited material had better access to the top surface of the needles than the bases. However, this effect is not noted in dense EBL-BDD samples.

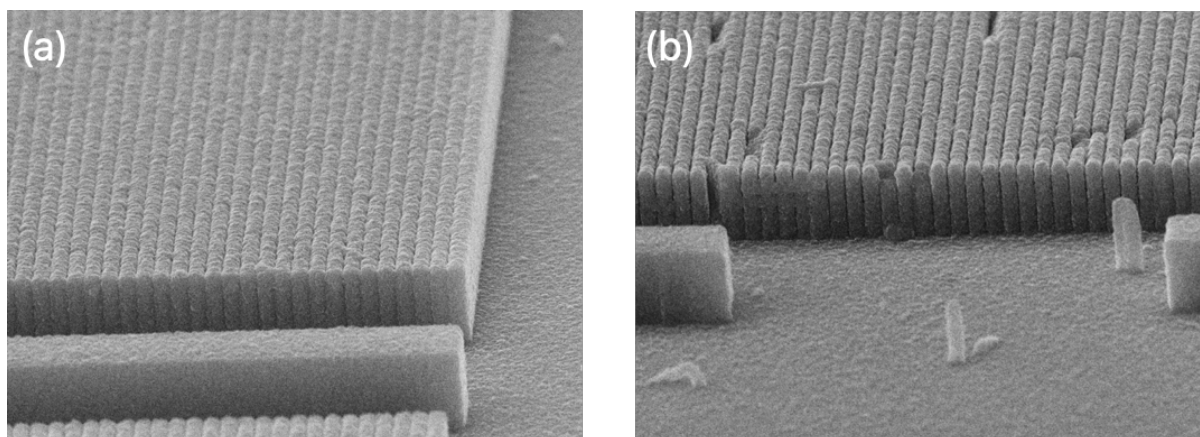


Figure 5.1. (a) Si-03 R1C4 T220 P383 SEM & (b) Si-03 R1C1 T160 P383 SEM.

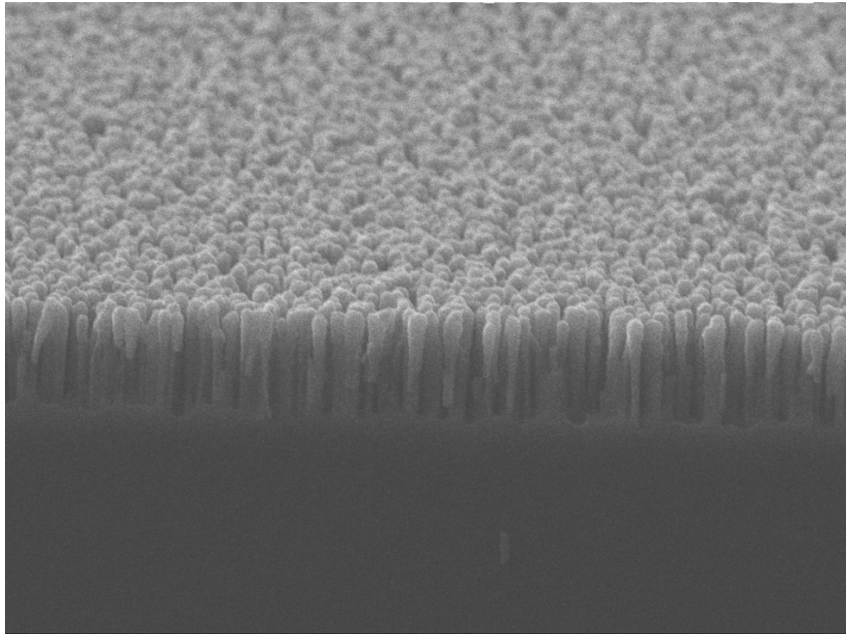


Figure 5.2. bd(MM33)-BDD Side Profile indicating poor consistency of coverage for the needle bases and widened tops after 30 minutes of BDD deposition.

5.1.1.2. EBL-Si Substrate Pattern Accuracy

Through SEM it has been shown that the EBL-Si substrate columns do not possess the exact desired T and P values that have been selected. This is indicated in **Table 5.1.** which shows that the etching process has left the columns with a greater thickness than desired. However, the accuracy of the patterning process for producing the required Pitch is high.

The impact of this deviation from the desired pattern becomes clearer for smaller T values. This indicates that a limit may be being approached that could be difficult to overcome. For this reason, a T value of 200 was chosen as the minimum appropriate T value at this time. Further experiments to improve pattern accuracy ought to be performed.

Table 5.1. Various applied Si patterns with their required column pattern and the actual column pattern, determined through SEM.

T_{Required} (nm)	T_{Actual} (nm)	T_{Actual} / T_{Required}	P_{Required} (nm)	P_{Actual} (nm)	P_{Actual} / P_{Required}
100	169	1.69	600	600	1.00
150	207	1.38	600	600	1.00
200	242	1.21	600	620	1.03
200	233	1.17	900	900	1.00
200	220	1.10	1000	1038	1.04

5.1.2. Post-nickel Deposition & Dealloying Pattern Definition

5.1.2.1. f-BDD Electrode

The f-BDD sample clearly shows that deposition of nickel has occurred. In **Figure 5.3. (a)** the divide between the exposed and non-exposed regions of the electrode is visible. However, SEM alone cannot tell us definitively what the composition of the deposited layer is as the Ni-Cu alloy may not have been fully dealloyed.

Most of the exposed region of the electrode appears to have resulted in small boulder deposits that cover the underlying BDD support layer almost entirely, as seen to the left of **Figure 5.3. (b)**. In this region, the structures are mostly of the same scale, however, there are larger structures within the region. These may be formed entirely post-nickel deposition, or they may be large BDD structures, formed during the HFCVD deposition process that have been thinly coated in nickel. **Figure 5.3. (b)** also shows regions which have not entirely been coated with nickel. This may suggest that (i) the surface morphology of the BDD electrode is not entirely homogeneous leading to discrepancies in the deposited film or (ii) the Ni-Cu alloy deposition phase was not complete.

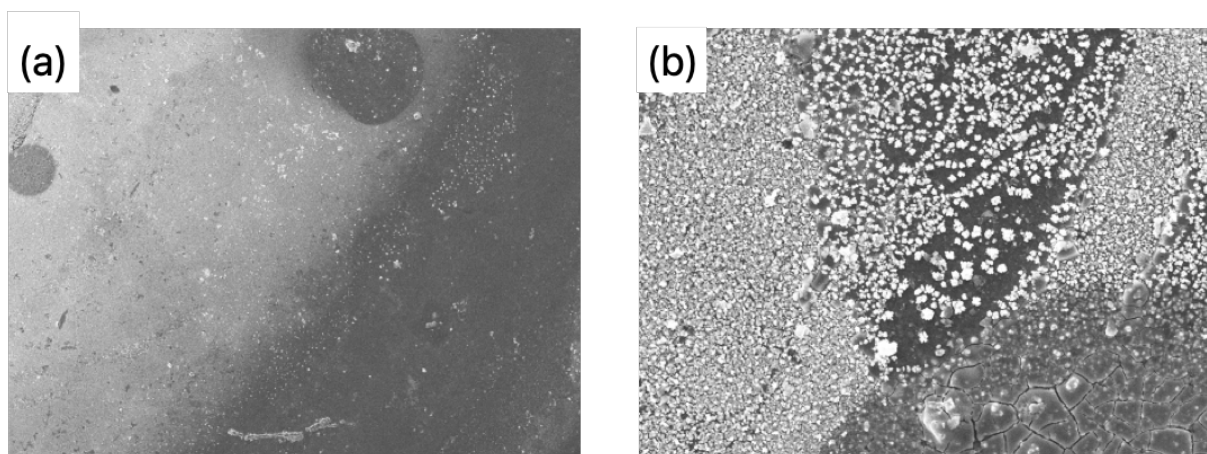


Figure 5.3. f-BDD 6hrs O-terminated after Ni-Cu alloy deposition and dealloying where **(a)** indicates the boundary between the exposed and non-exposed areas of the f-BDD electrode & **(b)** shows different regions that are exhibited by the exposed area.

5.1.2.2. bD-BDD Electrodes

Comparison between bD(MM22)-BDD and after the nanoporous nickel deposition process (bD(MM22)-Ni) by SEM indicates that nickel has been successfully deposited onto the BDD-coated support nanostructures.

Figure 5.4. (a) shows that the bD(MM22)-BDD nanostructures have clumped together but that the BDD deposition process has successfully coated these needles/clusters individually. While **Figure 5.4. (b)** shows that the bD(MM22)-Ni structure has a new layer coated above. This is believed to be the nanoporous nickel layer. However, SEM is not sufficient to determine whether the nickel has deposited on each needle down to the bases. The newly formed layer on the top may be the only deposited nickel on the structure.

Figure 5.4. (b) shows that strands have formed between each needle in regions that have not entirely been coated with nickel. Deposition of nickel does not result in individual needle coating. A greater spacing between needles ought to be provided to allow for the solution to form better contact with the nanostructured surface. This is a benefit of EBL-BDD electrodes over bD-BDD electrodes, as the uniformly spaced arrays of EBL-BDD can be controlled to ensure that regions which are too dense do not arise. This is not the case for bD-BDD as the nanostructured bSi fabrication process results in randomly placed needles.

To continue with bSi substrates, it may be necessary to alter the initial etching process to ensure better needle separation. This could be done by altering the gas-phase composition, temperature or substrate bias, as mentioned in **Section 2.4.3.5**.

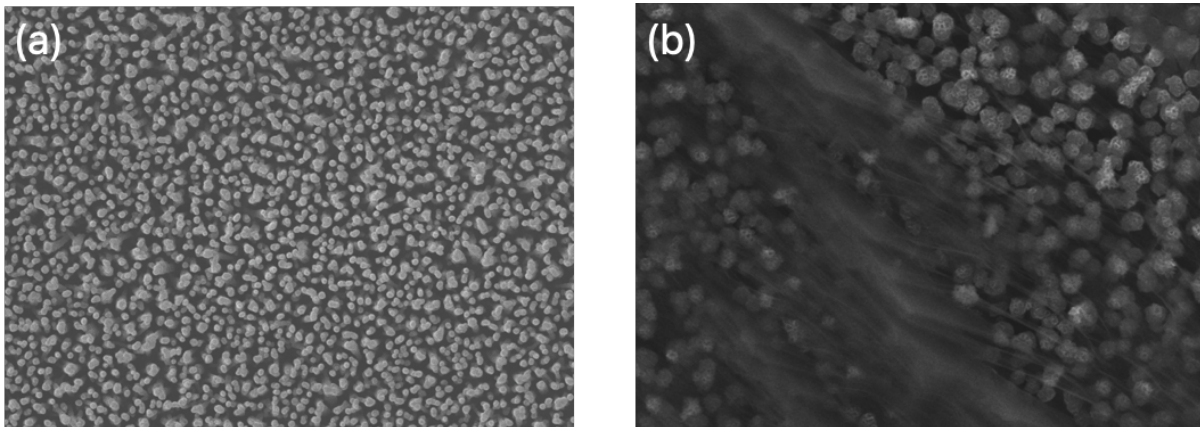


Figure 5.4. (a) Top-down view of bD(MM22)-BDD & **(b)** Top-down view of bD(MM22)-Ni.

5.2. Energy-dispersive X-ray Spectroscopy (EDX)

5.2.1. EDX for f-BDD

5.2.1.1. Lack of Nickel Deposition

Figure 5.6. (a) & (b) shows that the dark circular regions of **Figure 5.5** are indicative of regions where nickel deposition has not been successful. Instead, an increased concentration of carbon, boron and oxygen is seen in **Figure 5.6. (e) & (f)**. The increase in oxygen may be due to increased O-termination. However, since the oxygen content correlates to the regions where the boron has a greater presence, we can suggest that the boron is present due to the drying of H_3BO_3 present in the solution.

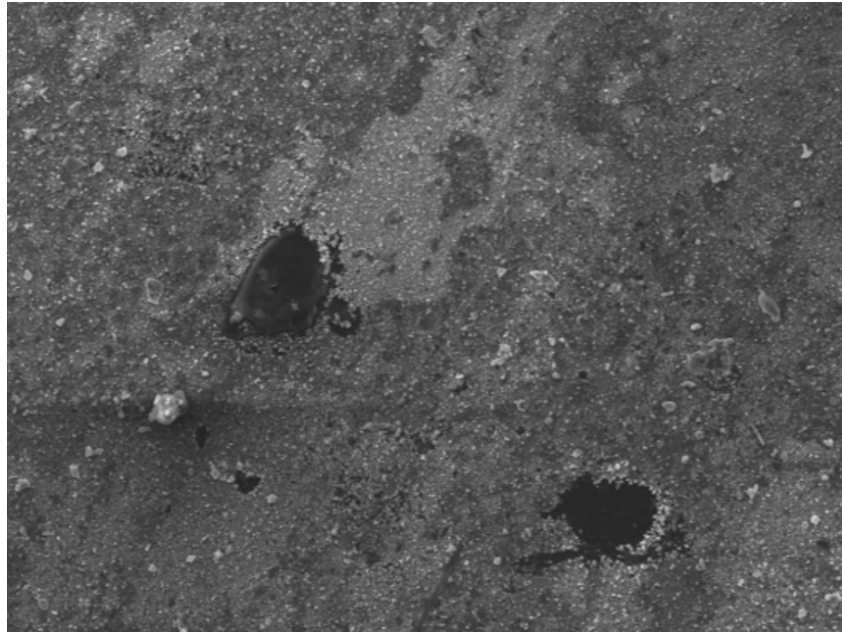


Figure 5.5. f-BDD-Ni reference image for EDX spectroscopy, showing that the dark regions have reduced nickel deposition.

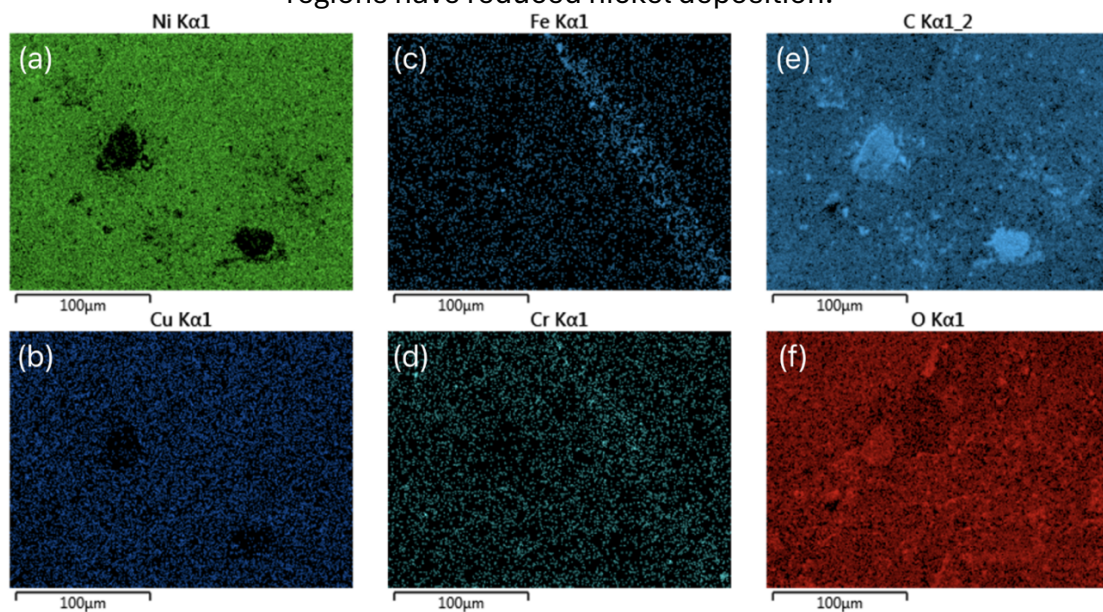


Figure 5.6. f-BDD-Ni composition (a) Nickel, (b) Copper, (c) Iron, (d) Chromium, (e) Carbon & (f) Oxygen.

5.2.1.2. Surface Contamination

The presence of iron and chromium is due to contamination. The shape of the markings suggests that contamination has occurred due to scratching, potentially caused by tweezers used to transport the electrode. This can be seen in **Figure 5.6 (c) & (d)**.

5.2.1.3. Bulk Nickel-deposited Region

The darker region, highlighted by EDX Spectrum 8 in **Figure 5.7.**, indicates a region where nickel deposition has been more successful. In addition, the ratio of nickel to copper is high, as shown in **Table 5.2.**, indicating that dealloying has occurred to a large degree. This is slightly reduced in the lighter region encompassing EDX Spectrum 10. However, the remaining copper may be due to the drying of the solution on the surface rather than

alloyed metal. More rigorous cleaning of the electrode after deposition and dealloying should be performed to ensure that this is not the case.

Within the bulk of the electrode, there are regions where adequate deposition has not occurred. EDX Spectrum 9 of **Figure 5.7**. highlights a region where this is the case. Here, the presence of nickel is reduced greatly while copper remains roughly the same. This will reduce the overall effectiveness of the electrode and these regions must be diminished in further electrode fabrication. By stirring the solution, while performing deposition and dealloying, the contact can be improved and subsequently a more uniform layer of deposited material is expected.

Table 5.2. Composition of EDX Spectrums 8, 9 & 10. These spectrums highlight different regions within the bulk of the f-BDD electrode.

EDX Spectrum	% Nickel	% Copper	%Nickel / %Copper
EDX Spectrum 8	23.7	1.6	14.81
EDX Spectrum 9	4.9	1.5	3.27
EDX Spectrum 10	19.7	2.2	8.95

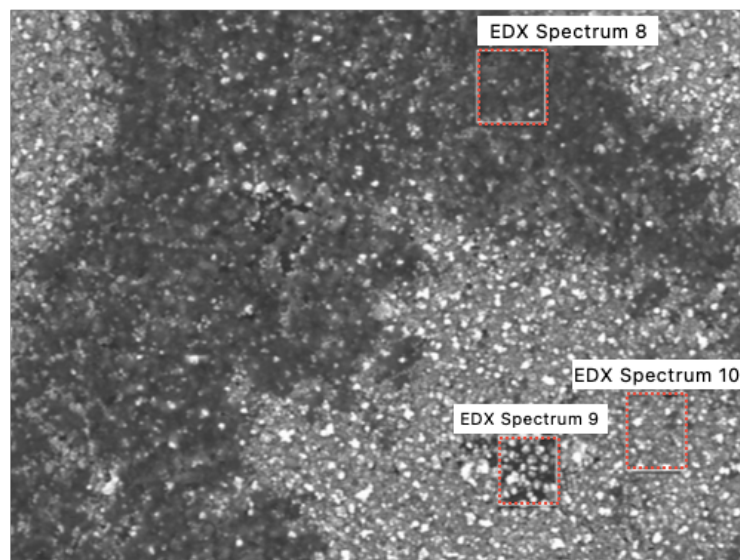


Figure 5.7. f-BDD-Ni Bulk nickel Deposition Region highlighting the three regions indicated by Spectrum's 8, 9 & 10.

5.2.2. EDX for bD-BDD

5.2.2.1. bD(MM22)-Ni Bulk Deposition

Nickel deposition is much lower in bD(MM22)-Ni than in the f-BDD-Ni sample. The nickel concentrates in the darker regions of **Figure 5.8**. which appear to be more overgrown. The presence of nickel also coincides with the presence of oxygen which may be due to O-termination or solution that has dried on the surface. The latter is made more convincing since sulphur and nickel are present in the same proportions. The concentration of copper is negligible.

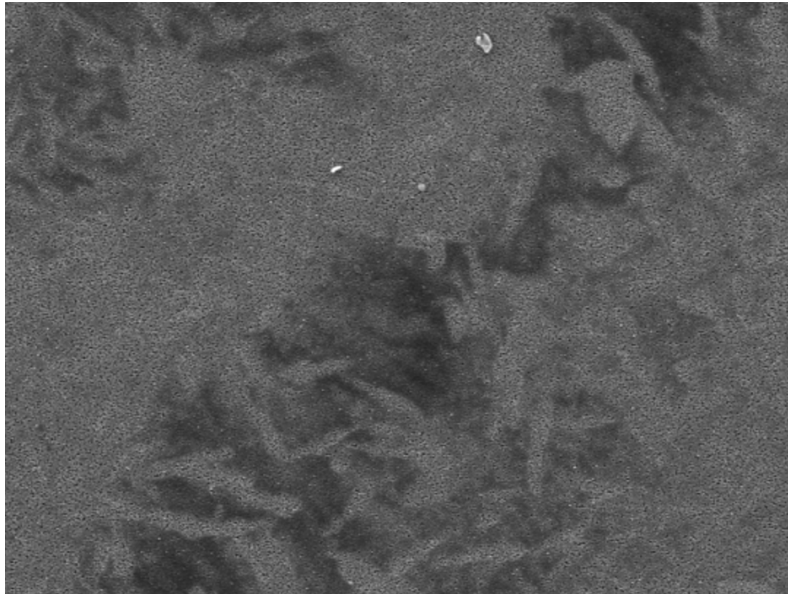


Figure 5.8. bD(MM22)-Ni Bulk Deposition Region showing that darker regions have greater nickel deposition than the lighter regions.

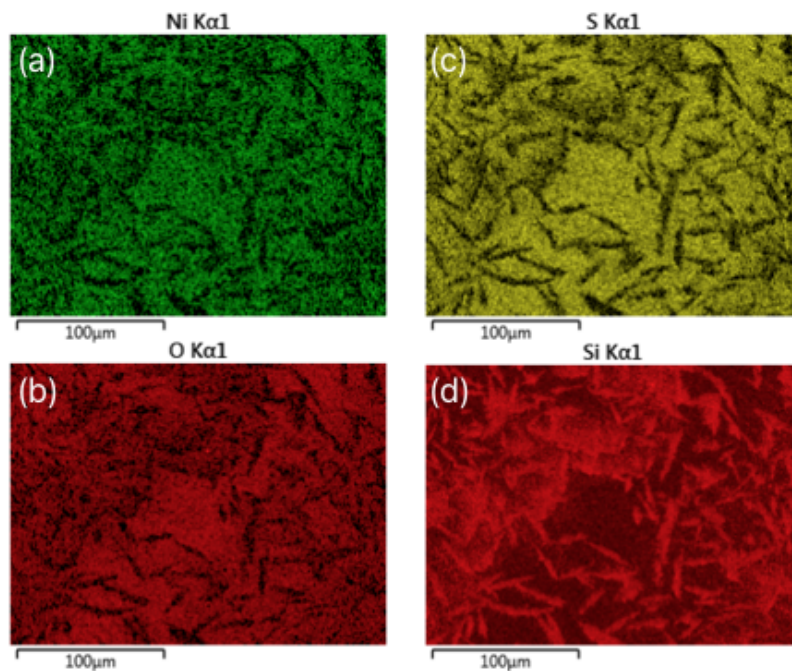


Figure 5.9. bD(MM22)-Ni Bulk Deposition Region (a) Nickel, (b) Oxygen, (c) Sulphur & (d) Silicon.

5.2.2.2. bD(MM22)-Ni Close-up

Figure 5.11. (d) shows that it is the gaps between the needles, shown in **Figure 5.10.**, that are exposed silicon. This suggests that the bases of the needles were not coated with BDD during the HFCVD process, leaving the silicon exposed. Whereas the tops of the needles are coated in carbon suggesting BDD deposition has occurred. It is only in the region where the definition of the gaps between the needles is lost that limited nickel deposition is present. This suggests that the initial HFCVD BDD deposition process was not entirely complete, resulting in an incomplete electrode surface. This will result in a reduced capacitance as well as a poorer quality deposited nickel layer. It is expected that, for EBL-BDD samples, BDD

deposition will be more uniform and so will subsequent nickel deposition. However, this would be dependent on the T and P values of the initial silicon substrate.

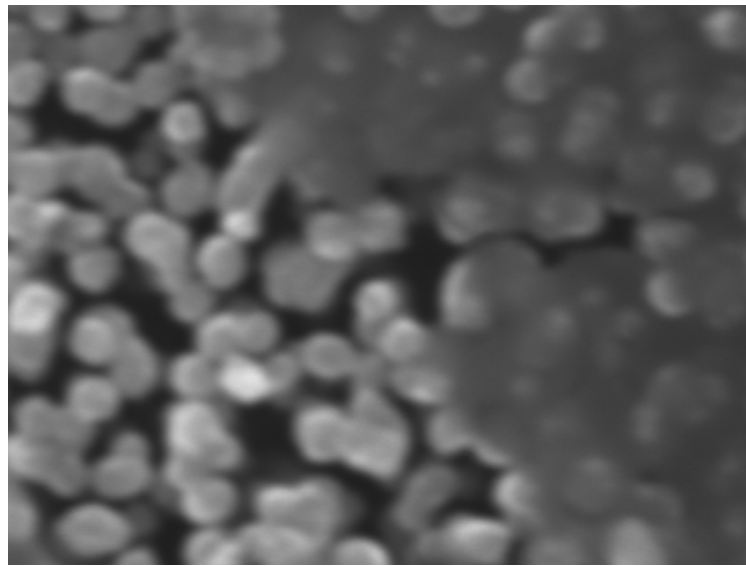


Figure 5.10. bD(MM22)-Ni Close-up showing the overgrowth of diamond in the darker region and the lack of BDD deposition in the lighter region.

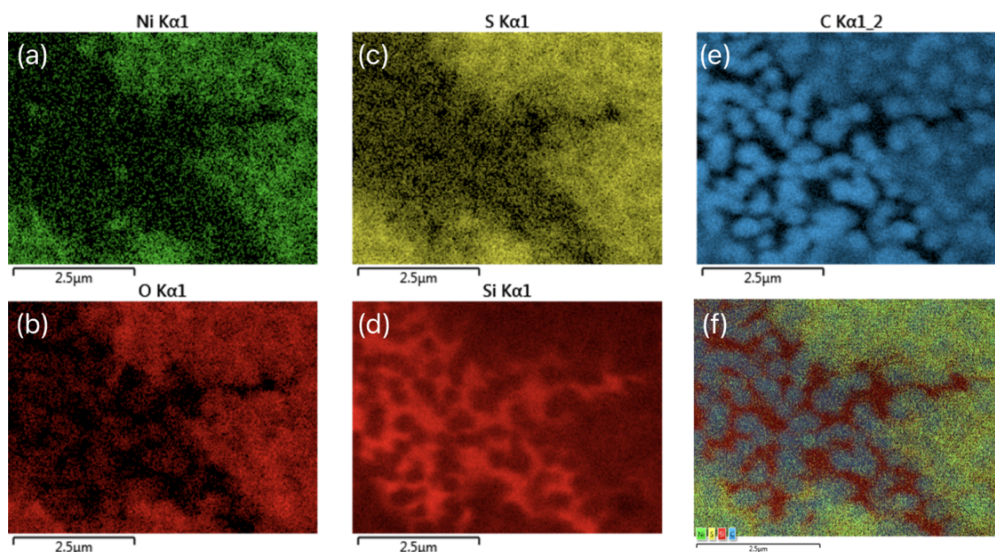


Figure 5.11. EDX Maps for bD(MM22)-Ni (a) Nickel, (b) Oxygen, (c) Sulphur, (d) Silicon, (e) Carbon & (f) Layered Image.

To gain a greater understanding of the HFCVD and nickel deposition processes, the sample should be cleaved in half so that a side view of the needles can be observed. This will help determine how deep the deposition process goes within the bulk of the electrode area.

5.3. Raman Spectroscopy

Nanostructured Nickel-coated BDD electrodes exhibit features which indicate high levels of boron doping when excited with the Renishaw RM 2000 laser Raman spectrometer, with a 514 nm excitation source, as shown in **Figure 5.12**. This is made evident by the negative shift

in characteristic wavenumber for BDD samples associated with higher doping levels. Such as the characteristic boron-related bands at $\sim 500\text{cm}^{-1}$ and $\sim 1220\text{cm}^{-1}$. As well as the right-hand side of the NCD “shoulder” at $\sim 1289\text{cm}^{-1}$.¹⁵⁰

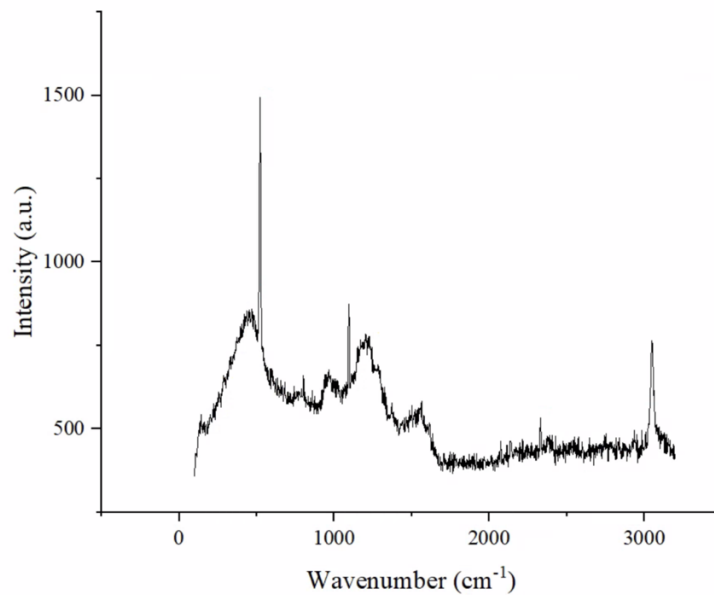


Figure 5.12. Raman spectra for bD(MM22)-Ni using green (514 nm) excitation.

bD(MM22)-Ni is shown to exhibit a highly disordered structure and the presence of a broad signal at $\sim 1150\text{cm}^{-1}$ is likely caused by the existence of polymeric sp^2 hybridised structures at the grain boundaries. The peak appears in the lower wavenumber side of the NCD “shoulder”.

Sp^2 hybridised structures being present indicates that the surface is NCD. This is because increased graphitisation is observed at grain boundaries and NCD surfaces have more grain boundaries than MCD surfaces, as covered in **Section 2.1.1**. The NCD sp^2 peak has not been shifted by the increased doping of boron.

The G peak, which is caused by graphitic impurities in MM22, is broad and weak but has not separated into two peaks, which is an observation noted in the literature, for highly-BDD NCD. This appears at $\sim 1550\text{cm}^{-1}$ which suggests that the G peak is also not negatively shifted by increased boron-doping. The D peak (disordered graphite) appears to have shifted with the diamond peak. However, this is difficult to interpret due to the formation of the NCD “shoulder” between $1050 - 1440\text{cm}^{-1}$, which masks the individual peaks. The strong and well-defined peak at 1094cm^{-1} is also believed to be related to NCD.

The strong Si peak at 523cm^{-1} appears to have not been shifted and neither has the associated second order $\sim 900 - 1000\text{cm}^{-1}$ broad peak.¹⁵¹ Due to the 523cm^{-1} peak being strong, relative to the NCD peaks, it can be suggested that the surface has not been sufficiently coated during the HFCVD process. This observation fits well with the data obtained by EDX and SEM.

The peak at 1332cm^{-1} , which corresponds to the diamond (sp^3) peak, appears to be rather subdued. This may be indicative of a combination of (i) increased graphitisation of the

surface during the metal deposition/dealloying process and (ii) asymmetry due to the Fano effect. However, this cannot be proven without further comparison between Raman spectroscopy from before and after nickel deposition. Increased graphitisation has been shown to occur after Nickel is sputtered onto BDD electrodes.¹⁵² Nickel itself is not Raman active so its presence should be determined through changes to the intensity of D, G and diamond peaks.

5.4. Cyclic Voltammetry

5.4.1. Effect of H- & O- Termination

HFCVD diamond growth is known to provide us with an H-terminated surface which will be hydrophobic, as covered in **Section 1.4.4.1**. This results in a contact between the solution and the electrode surface that is weak. Ozone treatment will change the surface of the electrode to O-terminated and hydrophilic. The hydrophilic surface will have an improved contact with the solution resulting in a higher C_{dl} value. This is shown to be the case and is represented by **Figure 5.13. & 5.14.** which shows that the C_{dl} of OT f-BDD is 1.85x greater than that of HT f-BDD.

Due to factors which limited the progress of this project, bD electrodes had to be used instead of the final EBL-BDD electrodes, as the fabrication of the EBL-BDD electrodes could not be completed. bD nanostructured electrodes were already O-terminated so a comparison between H- & O-terminated nanostructured electrodes could not be performed.

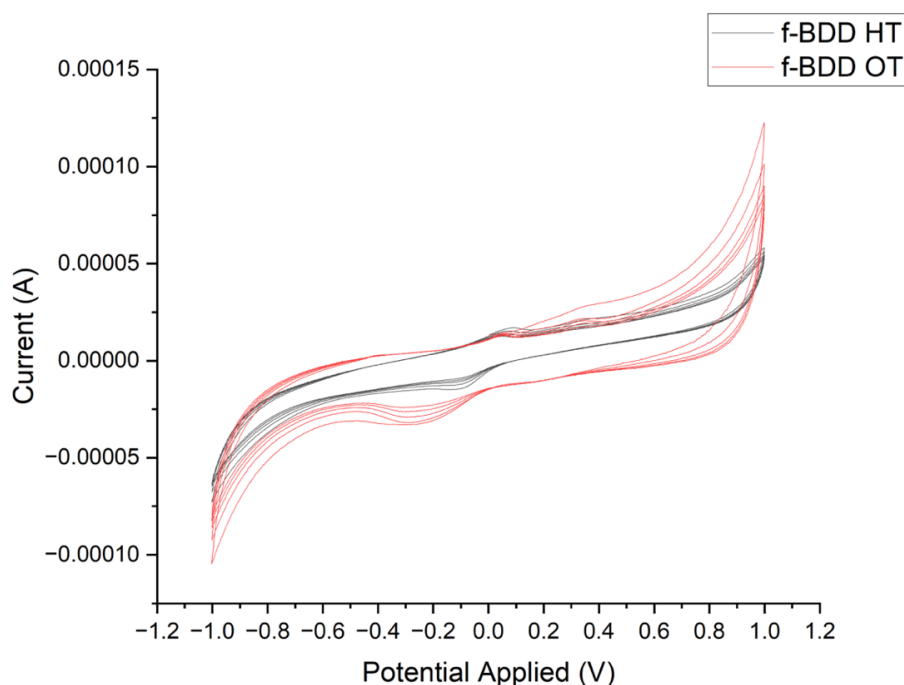


Figure 5.13. H- & O-terminated (HT & OT) capacitance CVs ($\nu = 500\text{mV/s}$) for a f-BDD sample in 100mM KNO_3 .

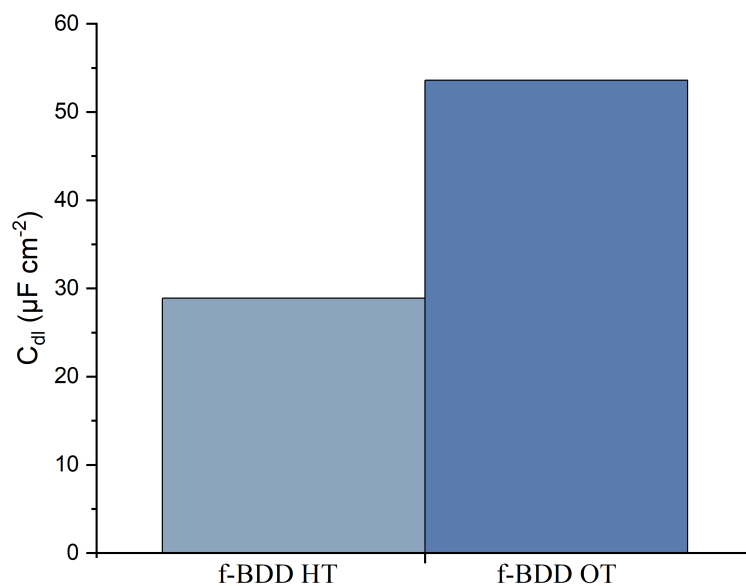


Figure 5.14. H- & O-terminated (HT & OT) calculated ($v = 500\text{mV/s}$) capacitance values for f-BDD in 100mM KNO_3 .

5.4.2. Double Layer Capacitance of f-BDD & bD-BDD

Figures 5.15. & 5.16. indicate that the C_{dl} of the bD(MM23)-BDD OT sample is 21.93x greater than that of the f-BDD OT sample. This suggests that, for O-terminated samples, the effective surface area of nanostructured bD-BDD electrodes is far greater than that of f-BDD. This is evident as the electrode capacitance is proportional to the effective surface area.¹⁴⁹ It would be useful to compare these results to H-terminated f-BDD and bD-BDD electrodes as it is likely the hydrophobicity would prevent the effective use of the individual needle's curved surface.

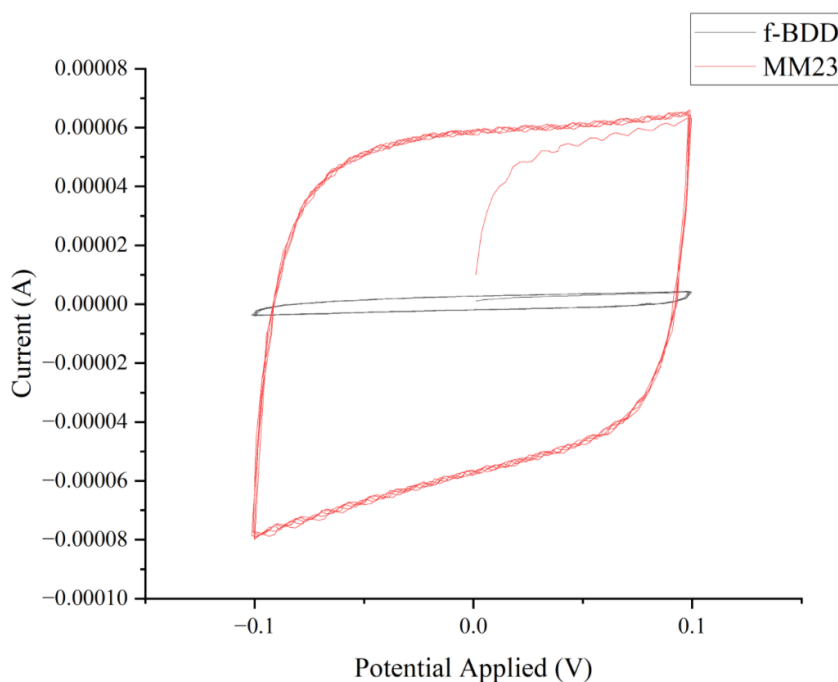


Figure 5.15. f-BDD and bD(MM23)-BDD capacitance CVs ($v = 1000 \text{ mV/s}$) in 100mM KNO_3 .

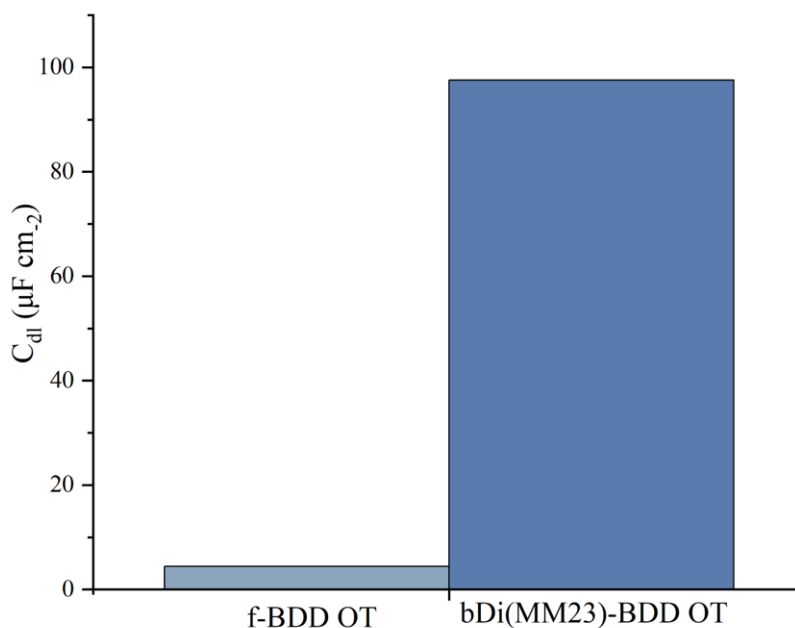


Figure 5.16. f-BDD and bD(MM23)-BDD calculated ($v = 1000\text{mV/s}$) capacitance values in 100mM KNO_3 .

5.4.3. Effective Surface Area of Electrodes

It is assumed that, for f-BDD, the geometric and effective surface area of the electrode are equal. Therefore, the relative effective surface area of the bD-electrode can be assumed to be a product of the ratio between f-BDD and the bD-BDD capacitance. This is detailed in **Table 5.3**.

While the relative effective surface area of the bD-BDD electrode is greater than that of the f-BDD electrode, it is not as great a difference as would be expected, considering the increased surface area of the bSi substrate. This suggests that the surface is not being used very efficiently, which may be due to incomplete BDD deposition, over-growth or high needle density preventing the solution from accessing further down the needles.

Table 5.3. Relative and Actual effective surface area values calculated from capacitance values for O-terminated BDD electrodes in 100mM KNO_3 solutions.

Electrode (OT) (KNO_3)	Capacitance ($\mu\text{F cm}^{-2}$)	Geometric Area (cm^2)	Relative Effective Surface Area	Effective Surface Area (cm^2)
f-BDD	4.45	0.5	1	0.5
bD(MM23)-BDD	97.58	0.6	21.93	13.16

Due to time constraints, the relative effective surface area of the EBL-BDD electrodes could not be determined. However, it is believed that EBL-BDD electrodes will provide an improvement to the efficient use of the substrate surface area. This is because of the wider spacing between columns and the uniformity of the array.

The actual surface area (A_{Actual}) of the EBL-BDD electrode can be calculated by taking the area of the flat surface (d^2) and adding the curved surface of each column. The total number of columns (n) can be determined based on the T, P and base area of the substrate. An

important assumption in this calculation is that the deposition of BDD is both uniform and complete. Therefore, the EBL-BDD A_{Actual} can be represented by **Equation 5.1**.

$$A_{\text{Actual}} = n(2\pi rh) + d^2 \quad (5.1.)$$

The efficiency of the use of the Actual Surface Area can be determined for EBL-BDD and will help determine what percentage of the available surface is in contact with the solution. This can be determined by **Equation 5.2**.

$$\text{Useful Area}\% = 100 (A_{\text{Effective}}/A_{\text{Actual}}) \quad (5.2.)$$

5.4.4. Effect of Scan Rate on Current

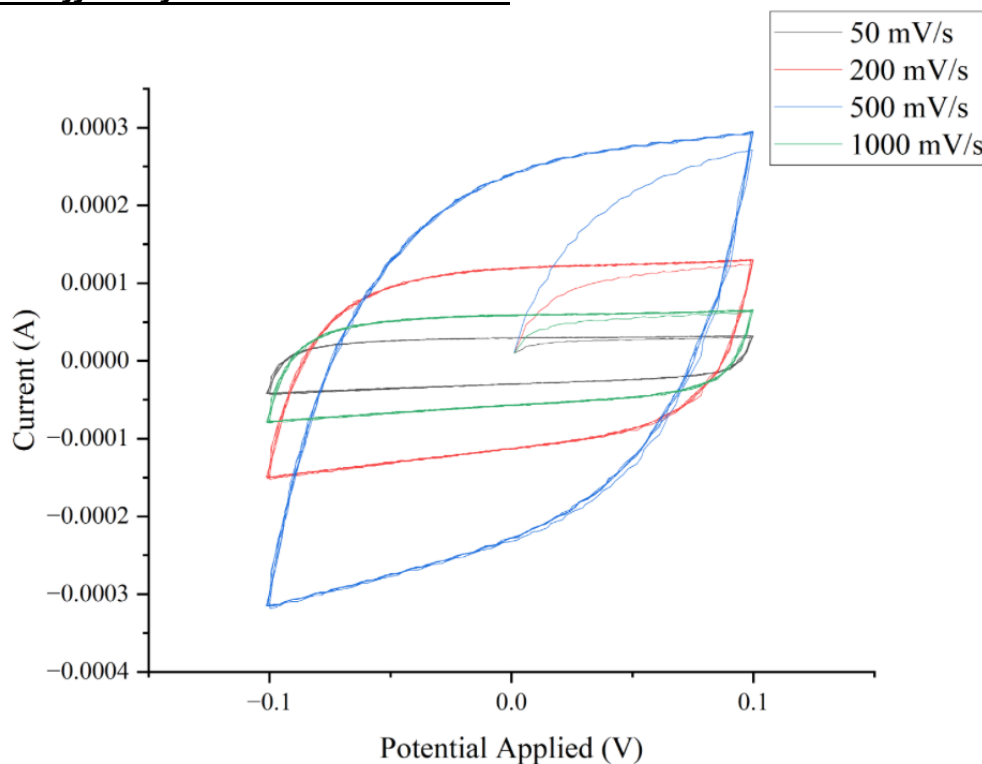


Figure 5.17. bD(MM23)-BDD capacitance CVs at four different scan rates. $V = 50, 200, 500$ & 1000 mV/s in 100mM KNO_3 .

A trend can be seen in **Figure 5.17**. that indicates that increasing scan rate increases the peak current observed. This is to be expected as the rate of diffusion is being increased faster than the rate of reaction at the interface. However, this appears to have broken down at a very high scan rate (1000 mV/s). This could either indicate that the results must be repeated or that the rate of diffusion and/or reaction are significantly impacted by the alteration to the scan rate. Further investigation in the $500 - 1000$ mV/s range is suggested.

5.4.5. Ni-Cu Solution Cyclic Voltammetry

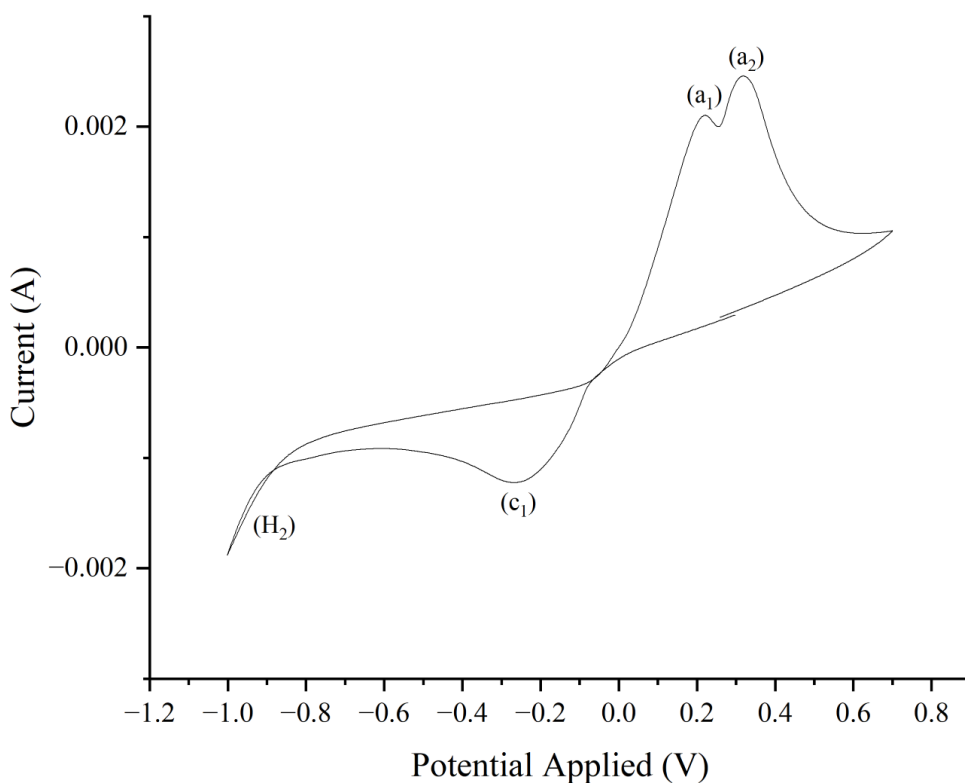


Figure 5.18. Cyclic Voltammogram for a f-BDD electrode in a solution containing 0.5M H_3BO_3 , 0.2M NiSO_4 and 0.01M CuSO_4 .

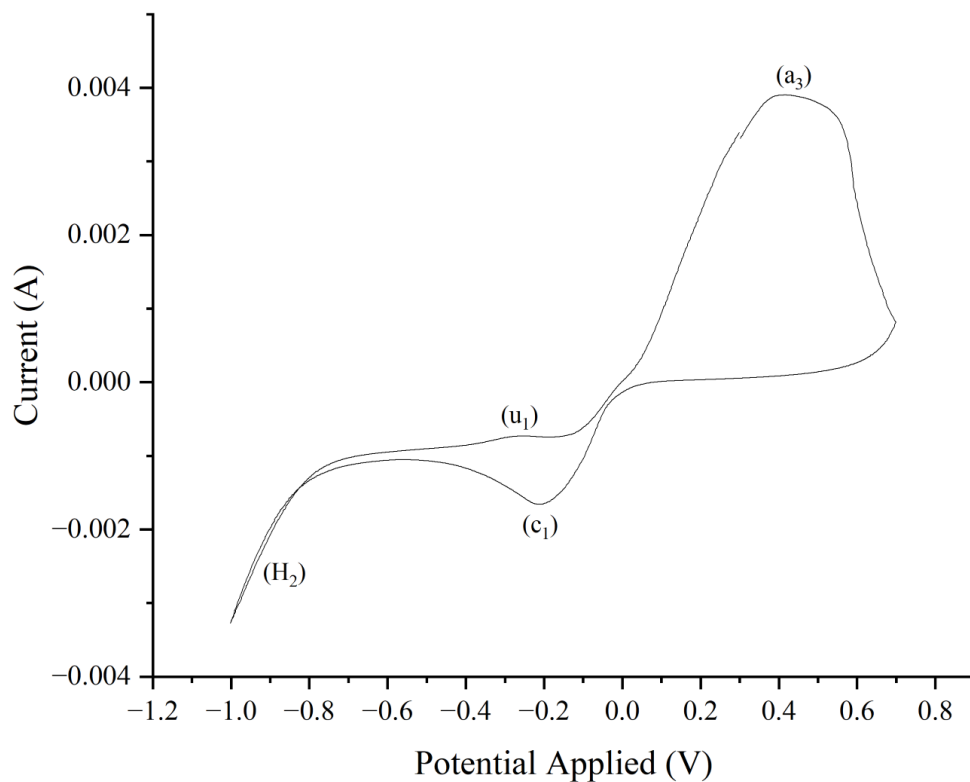


Figure 5.19. Cyclic Voltammogram for MM23 bD-BDD electrode in a solution containing 0.5M H_3BO_3 , 0.2M NiSO_4 and 0.01M CuSO_4 .

5.4.5.1. Anodic Potentials

The initial anodic peak a_1 , in **Figure 5.18.**, can be attributed to the anodic stripping of deposited copper metal to Cu(II) from the Ni-Cu film on the electrode. However, this has been overlaid by a more positive peak (a_2) due to the retardation of the copper stripping process. This is caused by the passivation of nickel. The process of passivation is known to be caused by the formation of a thin layer of NiO.⁶⁶ Therefore, we can infer the presence of a thin nickel oxide layer above the Ni-Cu alloy.

The CV for the bD-BDD nanostructured electrode, shown in **Figure 5.19.**, indicates a greater ability to oxidise and strip the copper from the alloy. However, only one peak (a_3) is now seen in the CV. This may indicate that a change in mechanism has occurred or that the reaction leading to either peak a_1 or a_2 has been favoured and fully covered the other peak. For this reason, further analysis of the surface is necessary to determine whether the thin NiO layer has been formed.

5.4.5.2. Cathodic Potentials

The cathodic peak (c_1) indicates that Cu(II) is reduced directly to copper metal. This process is consistent with more recent studies.⁶⁶ The reduction of Cu(II) to copper metal is seen for both f-BDD and bD-BDD electrodes indicating a consistent mechanism. Therefore, we can suggest that nickel deposition is possible.

In the CV for the bD-BDD sample, **Figure 5.19.**, a new small peak has been observed (u_1) which does not appear in the f-BDD sample. However, it is suggested that at around -0.1V a small peak can be observed which may correspond to passivation.⁶⁷

5.4.5.3. H₂ Evolution

Region H₂ indicates where H₂ evolution has occurred, this region ought to be as negative as possible. For our f-BDD sample, **Figure 5.18.**, the H₂ region is not particularly negative which indicates that f-BDD is not particularly good at H₂ evolution.⁶⁶ The nanostructured bD-BDD electrode, **Figure 5.19.**, shows improved hydrogen evolution in the useful cathodic range. This is indicated by the more negative current achieved in this range.

5.4.5.4. Dealloying

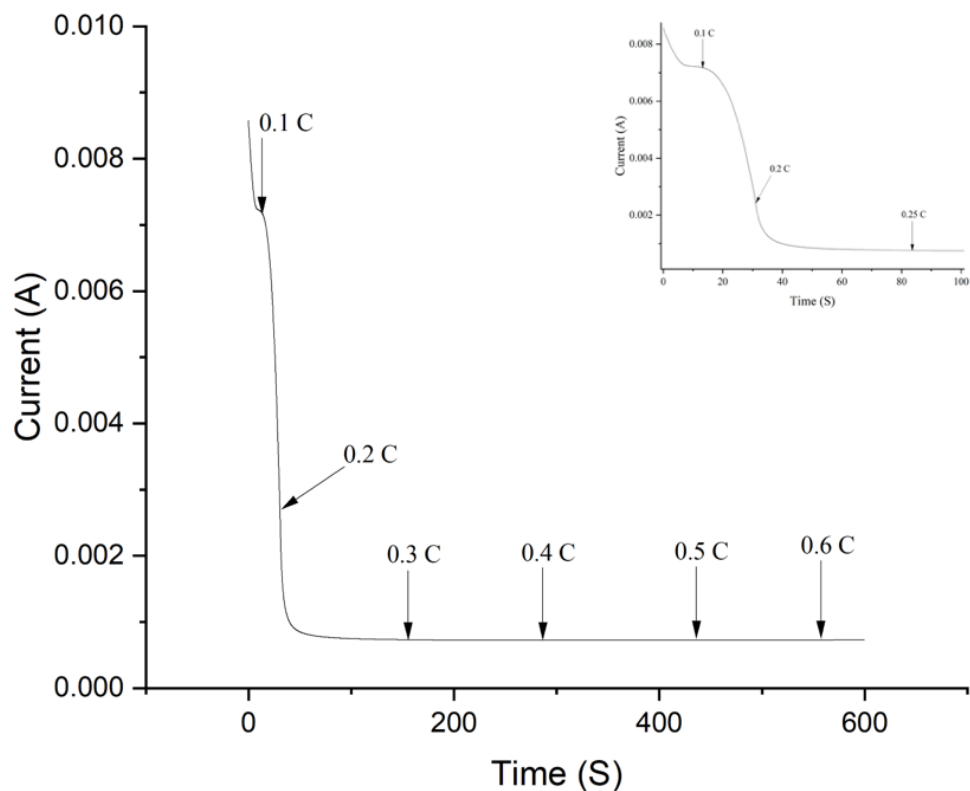


Figure 5.20. Current-time curve for the selective dissolution of copper from the Ni-Cu alloy on f-BDD electrodeposited at -0.85V with 0.5C charge.

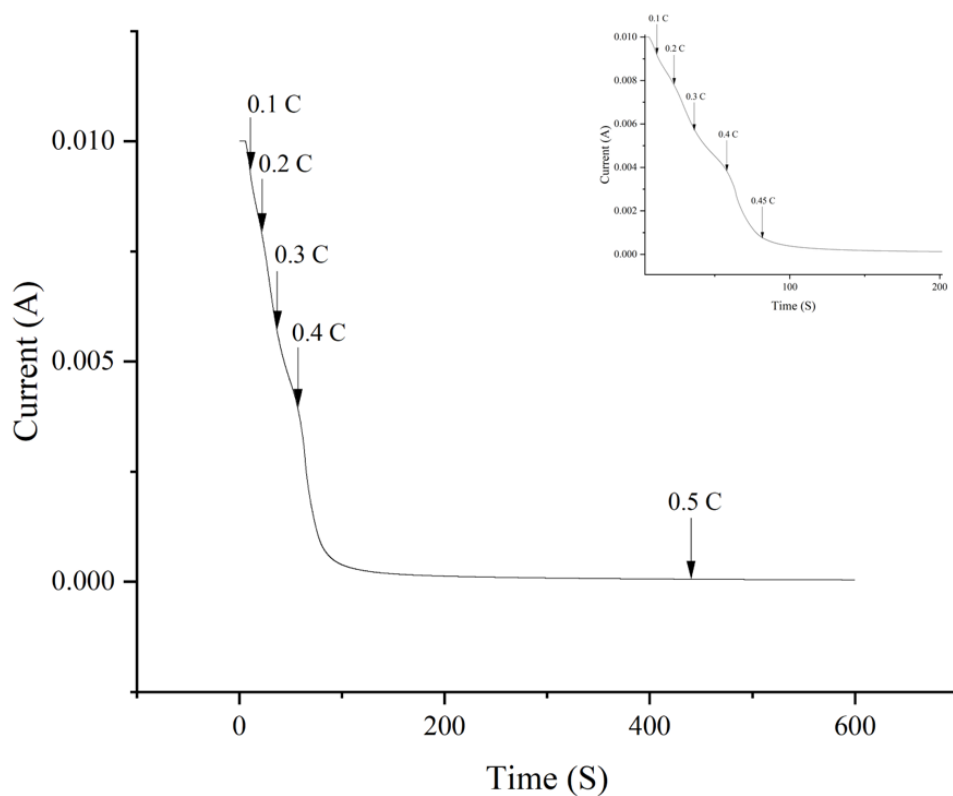


Figure 5.21. Current-time curve for the selective dissolution of copper from the Ni-Cu alloy on MM23 bD-BDD electrodeposited at -0.85V with 0.5C charge.

Figures 5.20. & 5.21. indicate that the dissolution current remains high and constant for f-BDD before dropping rapidly, once 0.1 C of charge has passed. This suggests that the rates for the creation and removal of active dissolution sites remain equal for a short period in our flat sample.⁶⁶

The dissolution current is expected to decrease rapidly once the porous nickel film is formed, as all the copper atoms have been removed. This is the case for the f-BDD sample, however, the process is much slower for the nanostructured electrode. Rather than staying constant and then rapidly dropping once the copper is removed, the dissolution current drops slowly and then collapses once 0.4C of charge has passed. This may suggest that the rates for the creation and removal of dissolution sites do not remain equal while the copper is removed from the nanostructured surface.

Chapter 6 Conclusions

The main aim of the project was to deposit conducting boron-doped diamond onto nanostructures, for use as high-surface-area electrochemical electrodes. Due to various limiting factors, the fabrication of the EBL-Si substrates was delayed considerably and boron-doped diamond deposition could not be performed. However, prototype substrates were characterised by SEM. f-BDD and bD-BDD samples were characterised by SEM, EDX, laser Raman and Cyclic Voltammetry. These electrodes were also used for the electrodeposition of nickel, as an example of the performance of a high-surface-area electrode.

EBL-Si substrates were successfully fabricated in the Physics clean-room facility and then observed using SEM. It has been determined that to ensure high pattern definition, post-HFCVD of BDD, each column should be separated by a Pitch value three times greater than the cross-sectional diameter of the column.

Failure to ensure adequate spacing between columns resulted in the over-growth of BDD and the loss of pattern definition. It is believed that, by reducing the effective surface area of the electrode, the double-layer capacitance of the electrode will be reduced. However, since the final EBL-Si substrates that were necessary for further analysis were not available for this project, these calculations could not be made at this time.

Additionally, SEM analysis indicated that the pattern accuracy of the EBL process was good but that the individual column diameter (T) often deviated from the desired size. This was especially true when $T < 200$ nm.

Cyclic Voltammetry experiments indicated that, for f-BDD electrodes, the alteration of the surface termination affects the performance of the electrode. For example, the O-termination of the f-BDD electrode increased double-layer capacitance by 1.85 times, compared to the H-terminated sample.

Cyclic Voltammetry also highlighted the improved double-layer capacitance of nanostructured bD-BDD electrodes over f-BDD electrodes. This can be attributed to the

21.93x increase in relative effective surface area of the bD-BDD electrode, compared to f-BDD.

Furthermore, Cyclic Voltammetry analysis of the NiSO_4 , CuSO_4 and H_3BO_3 solution suggested that the behaviour of flat and nanostructured (bD) electrodes may be slightly different during electrodeposition and dealloying. However, the nobler element, copper, is still believed to be stripped, due to the formation of a passivating layer. Improved H_2 evolution is also observed for the nanostructured electrode.

Raman analysis of bD(MM22)-Ni indicated that regions of highly-boron-doped diamond were present in the electrode. However, the presence of strong Si peaks indicates that the deposition of a continuous layer of BDD has not occurred and that some of the silicon substrate is still exposed. Also, sp^2 hybridisation-related peaks are seen which indicates that the surface is NCD, as increased graphitisation is observed at grain boundaries.

EDX analysis revealed that the deposition of the nickel layer was not continuous and that the HFCVD process was not complete, for the bD nanostructures. This latter point was evidenced by the lack of carbon between individual needles. This shows that deposition was not complete at the bases of the needles. The f-BDD sample showed improved deposition and dealloying, compared to the bD nanostructured sample. However, the f-BDD sample exhibited some regions which were more copper-rich than others. It was also seen that there were solution drying marks and contamination of the surface, in some instances.

Chapter 7 Future Work

There are many ways in which this topic may be expanded through future work. This could include:

1. Deposition of BDD onto the fabricated EBL-Si substrates produced at the end of this project. SEM, EDX, Raman and CV can then be used to analyse these new electrodes.
2. Nickel deposition on various nanostructured BDD electrodes. These could include (i) bD, (ii) EBL columns, (iii) honeycomb, (iv) CNTs & (v) CNT Teepees. These nanostructures were covered in greater detail in **Section 2.4**. The performance of these electrodes for hydrogen evolution can then be tested.
3. The fabrication of nanostructured aliquots. This would be useful as it would allow for SEM, EDX and Raman analysis to be performed (i) before the deposition of the Ni-Cu alloy, (ii) after the deposition of the Ni-Cu alloy and (iii) after Ni-Cu dealloying. Aliquots would make it possible to observe each step of the process under the same starting conditions.
4. A comparison between MCD and NCD nanostructured BDD electrodes. This could include a comparison between capacitance or perhaps nickel deposition uniformity. The increased graphitisation of the NCD surface may affect nickel deposition.
5. Attempt to produce EBL-Si wafers with smaller T values, to allow for thicker diamond layers to be grown, which may improve survivability.
6. Vary boron-doping of diamond layer for different nanostructures. CV analysis and nickel deposition could then be attempted.
7. Producing EBL-BDD electrodes with different T and P values. The Useful Area value could then be calculated to determine what conditions lead to the most efficient use of the provided electrode surface area.

Chapter 8 References

1. A. K. Ramdas, in *Properties, Growth and Applications of Diamond*, Institute of Electrical Engineers, 2001, 3–6.
2. L. S. Pan and D. R. Kania, *Diamond: Electronic Properties and Applications*, Kluwer Academic, Boston, 1995.
3. C. J. H. Wort and R. S. Balmer, *Mater. Today*, 2008, **11(1)**, 22-28.
4. K. Miyoshi, 1998, “Structures and Mechanical Properties of Natural and Synthetic Diamonds” NAS 1.15:107249/CHAP8.
5. J E Field, *Rep. Prog. Phys.*, 2012, **75**, 126505.
6. J.V. Manca, M. Nesladek, M. Neelen, L. De Schepper and W. De Ceuninck, *Microelectron. Reliability*, 1999, **39(2)**, 269-273.
7. Coe and Sussmann – S. E. Coe and R. S. Sussmann, *Diam, Relat. Mater.*, 2000, **9(9)**, 1726-1729.
8. Gåhlin et al. - R. Gåhlin, H. Björkman, P. Rangsten and S. Jacobson, *Wear*, 1999, **233**, 387-394.
9. Da Silva Neto et al. - J. V. da Silva Neto, M. A. Fraga and V. J. Trava-Airoldi, *IntechOpen.*, London, UK, 2020.
10. C. Kittel and P. McEuen, *Introduction to solid state physics*, Wiley, Hoboken, NJ, 8th ed., 2022.
11. D. A. Neamen, *Semiconductor physics and devices: Basic principles*, McGraw-Hill, New York, N.Y, 2012.
12. D. K. Seo and R. Hoffmann, *Theor. Chem. Acc.*, 1999, **102**, 23-32.
13. V. K. Jain, *Solid State Physics*, Springer, New York, New York, USA, 2022.
14. K. Takahashi, A. Yoshikawa and A. Sandhu, *Wide bandgap semiconductors fundamental properties and modern photonic and electronic devices*, Springer, Berlin, 2007.
15. A. Kumar, M. Moradpour, M. Losito, W.-T. Franke, S. Ramasamy, R. Baccoli and G. Gatto, *Energies*, 2022, **15**, 9172.
16. F. Roccaforte, F. Giannazzo, F. Lucolano, J. Eriksson, M. H. Weng and V. Raineri, *Applied Surface Science*, 2010, **256**, 5727–5735.
17. A. Volta, *Philos. Trans. R. Soc. Lond.*, 1800, **90**, 403-431.
18. H. Davy, *Philos. Trans. R. Soc. Lond.*, 1807, **97**, 1-44.
19. M. Faraday, *Philos. Trans. R. Soc. Lond.*, 1834, **124**, 77–122.
20. A. J. Bard, L. R. Faulkner and H. S. White, *Electrochemical Methods: Fundamentals and Applications*. Wiley, Hoboken, New Jersey, 2001.
21. A. C. Fischer, *Electrode Dynamics.*, Oxford University Press, 1996.
22. N. Sato, *Electrochemistry at Material and Semiconductor Electrodes*, Elsevier, Amsterdam, Netherlands, 1998.
23. W. Schmickler, *Interfacial Electrochemistry.*, Oxford University Press, 1996. 299 – 230.
24. A. T. Celebi, M. Olgiati, F. Altmann, M. Kogler, L. Kalchgruber, J. Appenroth, U. Ramach, M. Valtiner and L. L. E. Mears, *Encyclopaedia of Solid-Liquid Interfaces.*, Elsevier, Amsterdam, Netherlands, 2024, 8 – 24.
25. O. Stern, *Zeitschrift für Elektrochemie*, 1924, **30**, 508-516.
26. G. Gouy, *Journal de Physique Théorique et Appliquée*, 1910, **9**, 457-468.
27. D. L. Chapman, *Philosophical Magazine*, 1913, **25**, 475-481.
28. S. M. Sze and K. K. Ng, *Physics of Semiconductor Devices*, John Wiley & Sons, Incorporated, Hoboken, New Jersey, 2006.
29. S.J. Cobb, Z.J. Ayres and J.V. Macpherson, *Annu. Rev. Anal. Chem.*, 2018, **11**, 463 – 484.

30. G. Wan, M. Cattelan and N. A. Fox, *J. Phys. Chem. A.*, 2019, **123**, 4168 – 4177.
31. G. Pippione, P. Olivero, M. Fischer, M. Schreck and A. Pasquarelli, *Phys. Status Solidi*, 2017, **214**, 1700223.
32. M. Alexander, M. N. Latto, G. Pastor-Moreno and D. J. Riley, *J. Electrochem. Soc.*, 2001, **25**, 54 – 65.
33. T. Watanabe, T. K. Shimzu, Y. Tateyama and Y. Kim, *Diam. Relat. Mater.*, 2010, **19**, 772 – 777.
34. Y. Kato, D. Tsujikawa, Y. Hashimoto, T. Yoshida, T. Fukami, H. Matsuda, M. Taguchi, T. Matsushita and H. Daimon, *Appl. Phys. Express*, 2018, **11**, 061302.
35. M. Werner, R. Job, A. Zaitzev, W. R. Fahrner, W. Seifert, C. Johnston and P. R. Chalker, *Physica Status Solidi (a)*, 1996, **154**, 385–393.
36. K. W. Böer, U. W. Pohl, Carrier Transport Induced and Controlled by Defects. In: *Semiconductor Physics*. Springer, Cham, 2023.
37. Y. H. Chen, C. T. Hu and I. N. Lin, *Appl. Phys. Lett.*, 1999, **75**, 2857 – 2859.
38. P. Muret, J. Pernot, A. Kumar and L. Magaud, *Phys. Rev. B*, 2010, **81**, 235205 – 235220.
39. P. Muret, P. -N. Volpe, J. Pernot and F. Omnes, *Diam. Relat. Mater.*, 2011, **20**, 722 – 725.
40. J. P. Goss and P. R. Briddon, *Physical Review B*, 2003, **68**, 235209.
41. Allahverdiyeva, P. Talay Pınar, Y. Yardım and Z. Şentürk, *Diamond and Related Materials*, 2021, **114**, 108332.
42. S. M. Tan, H. L. Poh, Z. Sofer and M. Pumera, *The Analyst*, 2013, **138**, 4885.
43. T. N. Rao, I. Yagi, T. Miwa, D. A. Tryk and A. Fujishima, *Anal. Chem.*, 1999, **71**, 2506.
44. T. M. Selva and T. R. Paixao, *New J. Chem.*, 2016, **40**, 2514-2520.
45. L. Wu, X. Liu, X. Yu, S. Xu, S. Zhang and S. Guo, *Materials*, 2022, **15**, 6013.
46. T. Kondo, *Curr. Opin. Electrochem.*, 2022, **32**, 100891.
47. R. Tenne, K. Patel, K. Hashimoto and A. Fujishima, *Journal of Electroanalytical Chemistry*, 1993, **347**, 409–415.
48. T. Kuwana, *Ber. Bunsen-Ges. Physik. Chem.*, 1973, **77**, 858 – 871.
49. J. K. Zak, J. E. Butler and G. M. Swain, *Anal. Chem.*, 2001, **73**, 908 – 914.
50. S. Haymond, J. K. Zak, Y. Show, J. E. Butler, G. T. Babcock and G. M. Swain, *Anal. Chim. Acta*, 2003, **500**, 137 –144.
51. Y. Dai, G. M. Swain, M. D. Porter and J. Zak, *Anal. Chem.*, 2008, **80**, 14 – 22.
52. J. Stotter, Y. Show, S. Wang and G. M. Swain, *Chem. Mater.*, 2005, **17**, 4880 – 4888.
53. W. Luo and L. Dai, *Carbon Nanotubes*, *InTech Open*, London, UK, 2010.
54. F. Gao and C. E. Nebel, *ACS Appl. Mater. Inter.*, 2016, **8**, 28244 – 28254.
55. W. Smirnov, A. Kriele, N. Yang and C. E. Nebel, *Diam. Relat. Mater.*, 2010, **19**, 186 – 189.
56. S. Yu, N. Yang, H. Zhuang, J. Meyer, S. Mandal, O. A. Williams, I. Lilge, H. Schronherr and X. Jiang, *J. Phys. Chem. C.*, 2015, **119**, 18918 – 18926.
57. Y. Takano, M. Nagao, K. Kobayashi, H. Umezawa, I. Sakaguchi, M. Tachiki, T. Hatano and H. Kawarada, *Appl. Phys. Lett.*, 2004, **85**, 2851–2853.
58. R. Solmaz, A. Döner, G. Kardas, *Electrochemistry Communications*, 2008, **10**, 1909–1911.
59. C. Hu, C. Lv, N. Zeng, A. Liu, Y. Li, L. Hu, P. Li, Y. Yao, J. Cai and T. Tang, *Energy Technol.*, 2022, **11**, 2201048.
60. L. Huo, C. Jin, K. Jiang, Q. Bao, Z. Hu and J. Chu, *Adv. Enr. Sust. Res*, 2022, **3**, 2100189.
61. M. F. Kibria, M. S. Mridha and A. H. Khan, *Int. J. Hydrog. Energy*, 1995, **20 (6)**, 435-440.
62. Z. Angeles-Olvera, A. Crespo-Yapur, O. Rodriguez, J. L. Cholula-Diaz, L. M. Martinez and M. Videa, *Energies*, 2022, **15**, 1609.

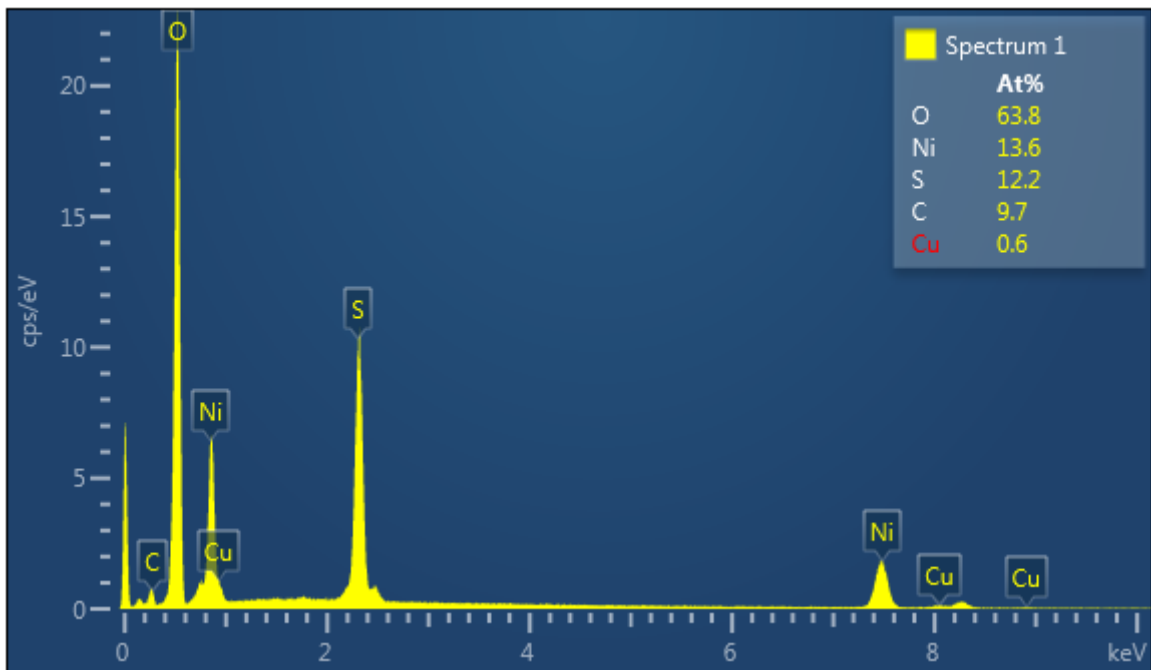
63. M. A. McArthur, L. Jorge, S. Coulombe and S. Omanovic, *J. Power Sources*, 2014, **266**, 365-373.
64. B. H. R Suryanto, Y. Wang, R. K. Hocking, W. Adamson and C. Zhao, *Nat. Commun.*, 2019, **10**, 5599.
65. L. A. Hutton, M. Vidotti, A. N. Patel, M. E. Newton, P. R. Unwin and J. V. Macpherson, *J. Phys. Chem. C*, 2011, **115**, 1649–1658.
66. J. K. Chang, S. H. Hsu, I. W. Sun and W. T. Tsai, *J. Phys. Chem. C*, 2008, **112**, 1371-1376.
67. L. Sun, C. L. Chien and P. C. Searson, *Chem. Mater.* 2004, **16**, 3125-3129.
68. R. Madhavaram, J. Sander, Y. X. Gan and C. K. Masiulaneic, *Mater. Chem. Phys.*, 2009, **118**, 165-173.
69. K. R. Koboski, E. F. Nelsen and J. R. Hampton, *Nanoscale Res. Lett.*, 2013, **8**, 528.
70. Z. Liu, L. Guo, C-L. Chien and P. C. Searson, *J. Electrochem. Soc.*, 2008, **155 (9)**, 569-574.
71. W. G. Eversole, US Patent 3030188, 1958.
72. B. V. Derjaguin, D. V. Fedoseev, V. M. Lukyanovich, B.V. Spitzin, V. A. Ryabov and A.V. Lavrentyev, *J. Cryst. Growth*, 1968, **2**, 380 – 384.
73. B.V. Spitsyn, L.L. Bouilov and B.V. Derjaguin, *J. Crystal Growth*, 1981, **52**, 219-226.
74. J. Lin, *Diamond Nanotechnology: Synthesis and Applications*, Pan, Stanford Publishing, 2009.
75. C. E. Johnson, W. A. Weimer and F. M. Cerio, *J. Mater. Res.*, 1992, **7**, 1427 – 1431.
76. S. J. Harris and D. G. Goodwin, *J. Phys Chem.*, 1993, **97(1)**, 23 – 28.
77. M. Chandran, *Carbon-Based Nanofillers and Their Rubber Nanocomposites*, Elsevier, Netherlands, 2019.
78. J. C. Angus, H. A. Will and W. S. Stanko, *J. Appl. Phys.*, 1968, **39**, 2915 – 2922.
79. K. K. Hirakuri, T. Kobayashi, E. Nakamura, N. Mutsukura, G. Friedbacher and Y. Machi, *Vacuum*, 2001, **63**, 449 – 454.
80. B. A. Reshi, S. Kumar, A. Misra and R. Varma, *Mater. Res. Express*, 2019, **6**, 046407.
81. P. W. May, M. N. Ashfold and Yu. A. Mankelevich, *J. Appl. Phys.*, 2007, **101**, 053115.
82. C. Wild, R. Kohl, N. Herres, W. Muller-Sebert and P. Koidl, *Diam. Relat. Mater.*, 1994, **3**, 373 – 381.
83. A. Cheesman, J. N. Harvey and M. N. R. Ashfold, *Phys. Chem. Chem. Phys.*, 2005, **7**, 1121 – 1126.
84. H. B. Schlegel, A. G. Baboul and S. J. Harris, *J. Phys. Chem.*, 1996, **100**, 9774 – 9979.
85. D. W. Comerford, A. Cheesman, T. P. F. Carpenter, D. M. E. Davies, N. A. Fox, R. S. Sage, J. A. Smith, M. N. R. Ashford and Y. A. Mankelevich, *J. Phys. Chem. A.*, 2006, **110**, 9, 2868 – 2875.
86. M. Kamo, Y. Sato, S. Matsumoto and N. Setaka, *J. Cryst. Growth*, 1983, **62**, 3, 642 – 644.
87. Y. Saito, S. Matsuda and S. Nogita, *J. Mater. Sci. Lett.*, 1986, **5**, 565 – 568.
88. P. W. May, *Philosophical Transactions of the Royal Society of London. Series A: Mathematical, Physical and Engineering Sciences*, 2000, **358**, 473–495.
89. S. Matsumoto, Y. Sato, M. Tsutsumi and N. Setaka, *J. Mater. Sci.*, 1982, **17**, 3106 – 3112.
90. M. A. McNeilly and W. C. Benzing, US Patent 3623712, 1969.
91. M. A. McNeilly and W. C. Benzing, US Patent 4047496, 1977.
92. Z. L. Wang, Q. Wang, H.J. Li, J.J. Li, P. Xu and Q. Luo, *Science and Tech. in Adv. Mat.*, 2005, **6**, 799-803.
93. I. Aharonovich, J. C. Lee, A. P. Magyar, D. O. Bracher and E. L. Hu, *Laser Photonics Rev.*, 2013, **7**, 61-65

94. A. Blanco, E. Chomski, S. Grabtchak, M. Ibisate, S. John and S. W. Leonard, *Nature*, 2000, **405**, 437-440.
95. W. Stober, A. Fink, *J. Colloid Interface Sci.*, 1968, **26**, 62-69
96. T. Van Regemorter and K. Larsson, *Diam. Relat. Mater.*, 2009, **18 (9)**, 1152-1156.
97. E.-S. Baik, Y.-J. Baik, S.W. Lee and D. Jeon, *Thin Solid Films*, 2000, **377**, 295 – 298.
98. T. Asano and J. Yasuda, *Jpn. J. of Appl. Phys.*, 1996, **35**, 6632.
99. P.A. Demkowicz, N.S. Bell, D.R. Gilbert, R. Singh, W.R. Drawl J. H. Adair, *J. Am. Ceram. Soc.*, 2004, **82**, 1079-1081.
100. H. Masuda, M. Watanabe, K. Yasui, D. Tryk, T. Rao, A. Fujishima, *Adv. Mater.*, 2000, **12**, 444-447.
101. H. Masuda, K. Yasui, M. Watanabe, K. Nishio, M. Nakao, T. Tamamura, T.N. Rao, A. Fujishima, *Electrochem. Solid St.*, 2001, **4**, 101- 103.
102. M. L. Terranova, S. Orlanducci, A. Forri, E. Tamburri and V. Sessa, *Chem. Mater.*, 2005, **17**, 3214-3220.
103. Y. Zou, P. W. May, S. M. C. Vieira and N. A. Fox, *J. Appl. Phys.*, 2012, **112**, 044903.
104. C.H. Hsu, S. G. Cloutier, S. Palefsky and J. Xu, *Nano Lett.*, 2010, **10(9)**, 3272-3276.
105. F. Weigl, S. Fricker, H-G. Goyen, C. Dietrich, B. Koslowski, A. Plettl and O. Pursche, *Diam. Relat. Mater.*, 2006, **15**, 1689-1694.
106. B. Koslowski, S. Strobel, T. Herzog, H. G. Boyen, R. Notz and P. Ziemann, *J. Appl. Phys.*, 2000, **87**, 7533 – 7538.
107. K. E. Strawhecker and S. K. Kumar, *Macromolecules*, 2001, **34**, 4669-4672.
108. A. Latypov and T.H. Coskun, *Directed Self-assembly of Block Copolymers for Nano-manufacturing*, Elsevier, Amsterdam, Netherlands, 2015.
109. X. Liu, P. R. Coxon, M. Peters, B. Hoex, J. M. Cole and D. J. Fray, *Energy Environ. Sci.*, 2014, **7**, 3223-3263.
110. P. W. May, M. Clegg, T. A. Silva, H. Zanin, O. Fatibello-Filho, V. Celorrio, D. J. Fermin, C. C. Welch, G. Hazell, L. Fisher, A. Nobbs and B. Su, *J. Mater. Chem. B*, 2016, **4**, 5737
111. A. M. Baracu, M. A. Avram, C. Breazu, M-C. Bunea, M. Socol, A. Stanculescu and E. Matei, *Nanomaterials*, 2021, **11(9)**, 2329
112. G. R. Sune, PhD Thesis, Universitat Autònoma de Barcelona, 2008.
113. C. Li, P. Yu, Y. Huang, Q. Zhou, I. Wu, Z. Li, X. Tong, Q. Wen, H-C. Kuo, Z. M. Wang, *Prog. Surf. Sci.*, 2020, **95(2)**, 100584.
114. L. Romano, *Micromachines*, 2021, **12 (8)**, 991.
115. S. Matsumoto, Y. Sato, M. Kamo and N. Setaka, *Jpn. J. Appl. Phys.*, 1982, **21**, 183.
116. K.F. Turner, B. R. Stoner, L. Bergman, J.T. Glass and R.J. Nemanich, *J. Appl. Phys.*, 1991, **69**, 6400-6405.
117. Y. Mitsuda, T. Yoshida and K. Akashi, *J. Mater. Sci.*, 1987, 1557.
118. Y. Saito, K. Sato, H. Tanaka, K. Fujita and S. Matuda, *J. of Mater. Sci.*, 1999, **23**, 842-846.
119. J. Yang, X. Su, Q. Chen and Z. Lin, *Appl. Phys. Lett.*, 1995, **66**, 3284-3286.
120. K. Kobayashi, M. Kumagai, S. Karasawa and T. Watanabe, *J. Cryst. Growth*, 1993, **128**, 408-412.
121. Liu
122. S.T. Lee, Y.W. Lam, Z. Lin, Y. Chan and Q. Chen, *Phys. Rev. B*, 1997, **55**, 15937 – 15941.
123. B.R. Stoner, G.-H. Ma, S.D. Wolter and J.T. Glass, *Phys. Rev. B*, 1992, **45**, 11067.

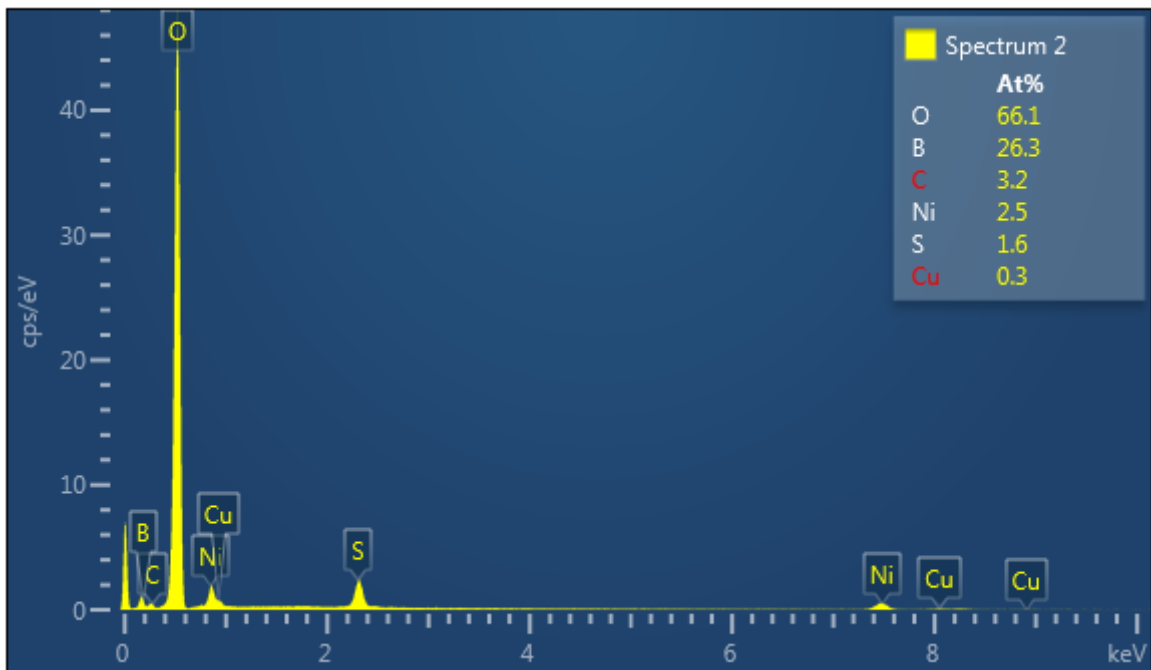
124. R. Stockel, M. Stammer, K. Janischowsky, L. Ley, M. Albrecht and H.P Strunk, *J. Appl. Phys.*, 1998, **83**, 531-539.
125. R. Stockel, K. Janischowsky, S. Rohmfeld, J. Ristein and M. Hundhausen, *J. Appl. Phys.*, 1996, **79**, 768-775.
126. B. A. Cola, R. Karru, C. Cheng, X. Xu and T.S. Fisher, *IEEE*, 2008, **31**, 46-53.
127. J. J. Lander and J. Morrison, *Surface Science*, 1966, **4**, 241-246.
128. S. Mandal, *RSC Adv.*, 2021, **17**, 10159 – 10182.
129. O. A. Williams, J. Hees, C. Dieker, W. Jager, L. Kirste and C. E. Nebel, *ACS Nano*, 2010, **4**, 4824 – 4830.
130. T. Petit, J.-C. Arnault, H. A. Girard, M. Sennour, and T.-Y. Kang, *Nanoscale*, 2012, **4**, 6792.
131. T. Wang, S. Handschuh-Wang, S. Zhang, X. Zhou and Y. Tang, *J. Colloid Interface Sci.*, 2017, **506**, 543 – 552.
132. R. C. Mendes de Barros, E. J. Corat, N. G. Ferreira, T. M. de Souza and V. J. Trava-Airoldi, N. F. Leite and K. Iha, *Diam. Relat. Mater.*, 1996, **5**, 1323 – 1332.
133. S. Iijima, Y. Aikawa and K. Baba, *J. Mater. Research*, 1991, **6**, 1491-1497.
134. L. Demuyne, J.C. Arnault, C. Speisser, R. Polini and F. Le Normand, *Diam. Relat. Mater.*, 1997, **6**, 235-239.
135. M. Varga, T. Izak, A. Kromka, M. Vesely, K. Hruska and M. Michalka, *Cent. Eur. J. Phys.*, 2012, **10**, 218-224.
136. R. Akhvlediani, I. Lior, S. Michaelson and A. Hoffman, *Diam. Relat. Mater.*, 2002, **11**, 545-549.
137. O. Shenderova, S. Hens and G. McGuire, *Diam. Relat. Mater.*, 2010, **19**, 260-267.
138. K. Hanada, K. Matsuzaki and T. Sano, *Surface Science*, 2007, **601**, 4502-4505.
139. C. I. Fornari, G. Fornari, P. H. de O. Rappl, E. Abramof and J. dos S. Travelho, *Epitaxy*, InTech, London, UK, 113-130.
140. A. van der Drift, *Philips Res. Repts.*, 1967, **22**, 267-288.
141. Hees, A. Kriele and O. A. Williams, *Chem. Phys. Letts.*, 2011, **509**, 12-15.
142. K. Akhtar, S. A. Khan, S. B. Khan and A. M. Asiri, *Scanning Electron Microscopy: Principle and Applications in Nanomaterials Characterization*, Springer, Cham., 2018.
143. N. Raval, R. Maheshwari, D. Kalyane, S. R. Youngren-Ortiz, M. B. Chougule, R. K. Tekade, *Basic Fundamentals of Drug Delivery*, Academic Press, Cambridge, Massachusetts, 2019, 269-400.
144. S. V. Pothula and Y. X. Gan, *Fabrication of Nickel/Zirconium Anode for Solid Oxide Fuel Cells by Electrochemical Method*, International Manufacturing Science and Engineering Conference, Erie, Pennsylvania, USA, April 2011, 433-437.
145. A. Orlando, F. Franceschini, C. Muscas, S. Pidkova, M. Bartoli, M. Rovere and A. Tagliaferro, *Chemosensors*, 2021, **9(9)**, 262.
146. N. Elgrishi, K. J. Rountree, B. D. McCarthy, E. S. Rountree, T. T. Eisenhart and J. L. Dempsey, *J. Chem. Educ.*, 2018, **95**, 197 – 206.
147. P. T. Kissinger and W. R. Heineman, *J. Chem. Educ.*, 1983, **60**, 702 – 706.
148. J. V. Macpherson, *Phys. Chem. Chem. Phys.*, 2015, **17**, 2935 – 2949.
149. P. W. May, M. Clegg, T. A. Silva, H. Zanin, O. Fatibello-Filho, V. Celorrio, D. J. Fermin, C. C. Welch, G. Hazell, L. Fisher, A. Nobbs and B. Su, *J. Mater. Chem. B.*, 2016, **4**, 5737.
150. V. Mortet, A. Taylor, Z. Vlčková Živcová, D. Machon, O. Frank, P. Hubík, Tremouilles, L. Kavan, *Diam. Relat. Mater.*, 2018, **88**, 163-166.

151. P. W. May, W. J. Ludlow, M. Hannaway, P. J. Heard, J. A. Smith and K. N. Rosser, *Diam. Relat. Mater.*, 2008, **17**, 105-117.
152. H. Long, X. Liu, Y. Xie, N. Hu, Z. Deng, Y. Jiang, Q. Wei, Z. Yu and S. Zhang, *J. Electroanal. Chem.*, 2019, **832**, 353-360.
153. X. Blase, E. Bustarret, C. Chapelier, T. Klein and C. Marcenat, *Nat. Mater.*, 2009, **8(5)**, 375–382.

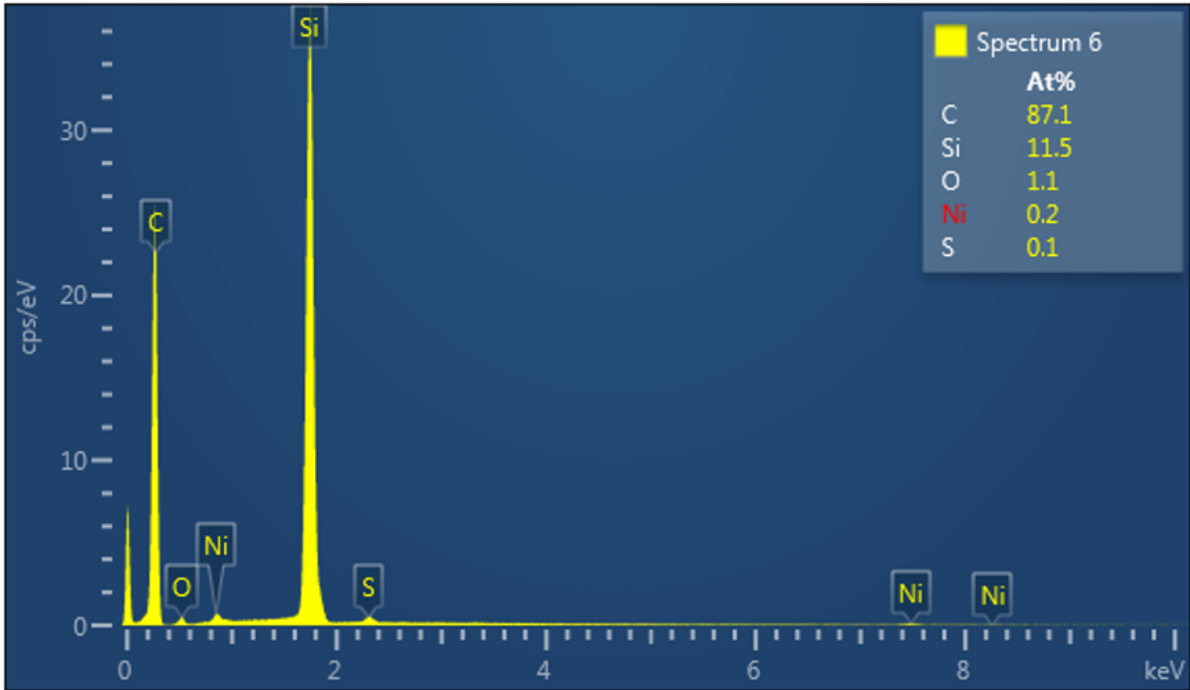
Appendix:



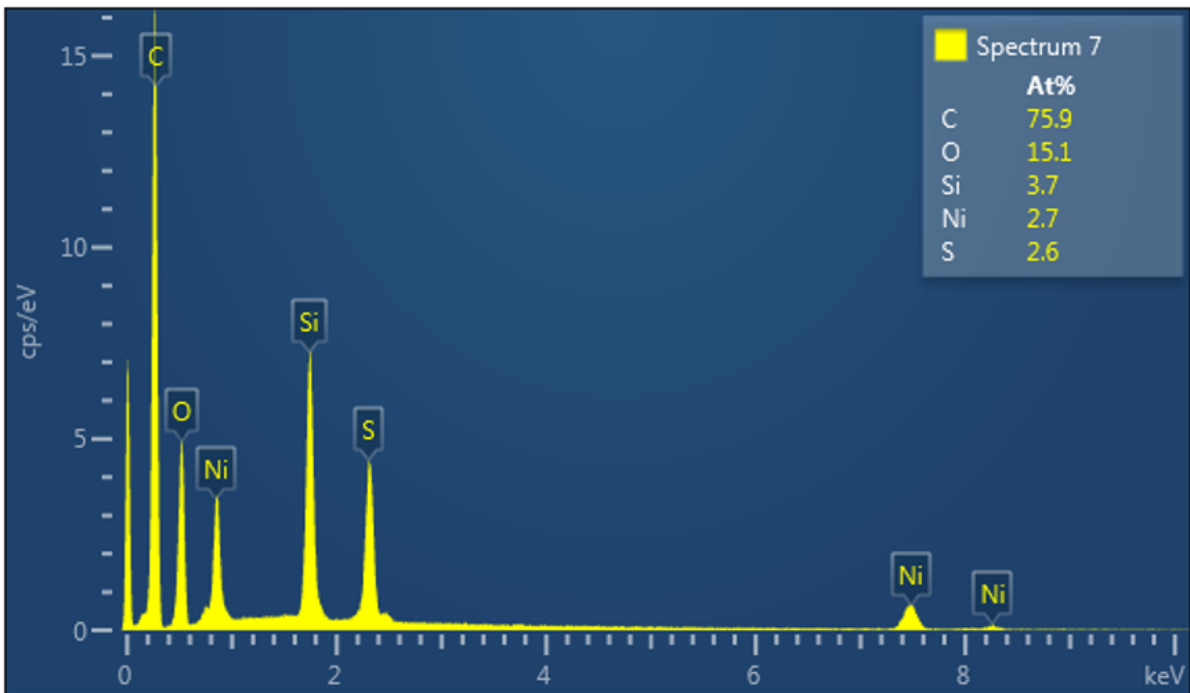
EDX Spectrum 1. Energy Dispersive Spectrum of bd(MM17)-BDD electrode after nickel deposition in a lighter over-grown region.



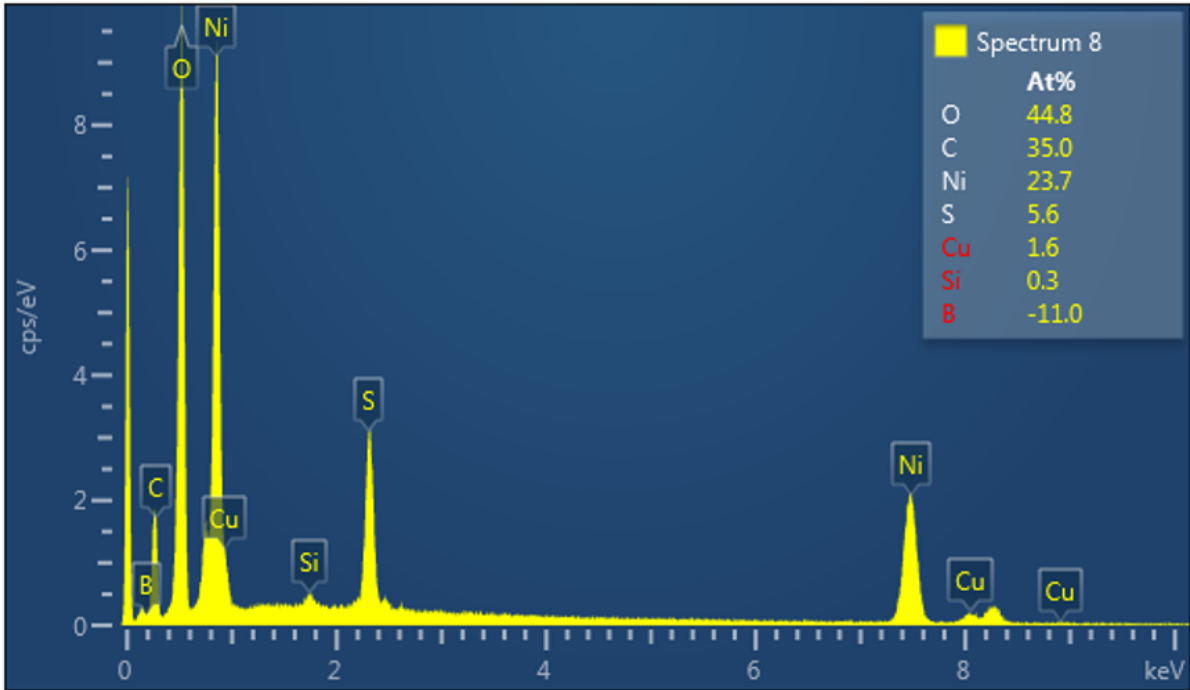
EDX Spectrum 2. Energy Dispersive Spectrum of bd(MM17)-BDD electrode after nickel deposition in a dark region with minimal deposition.



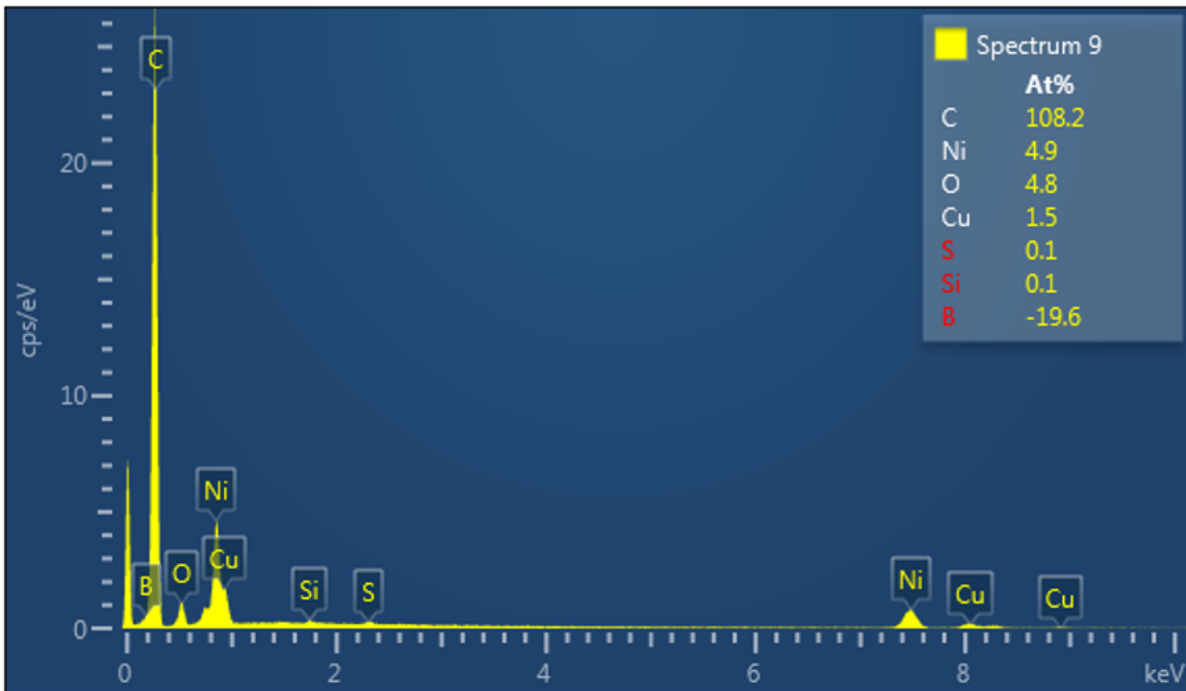
EDX Spectrum 6 Energy Dispersive Spectrum of bD(MM22)-BDD electrode after nickel deposition in the lighter region.



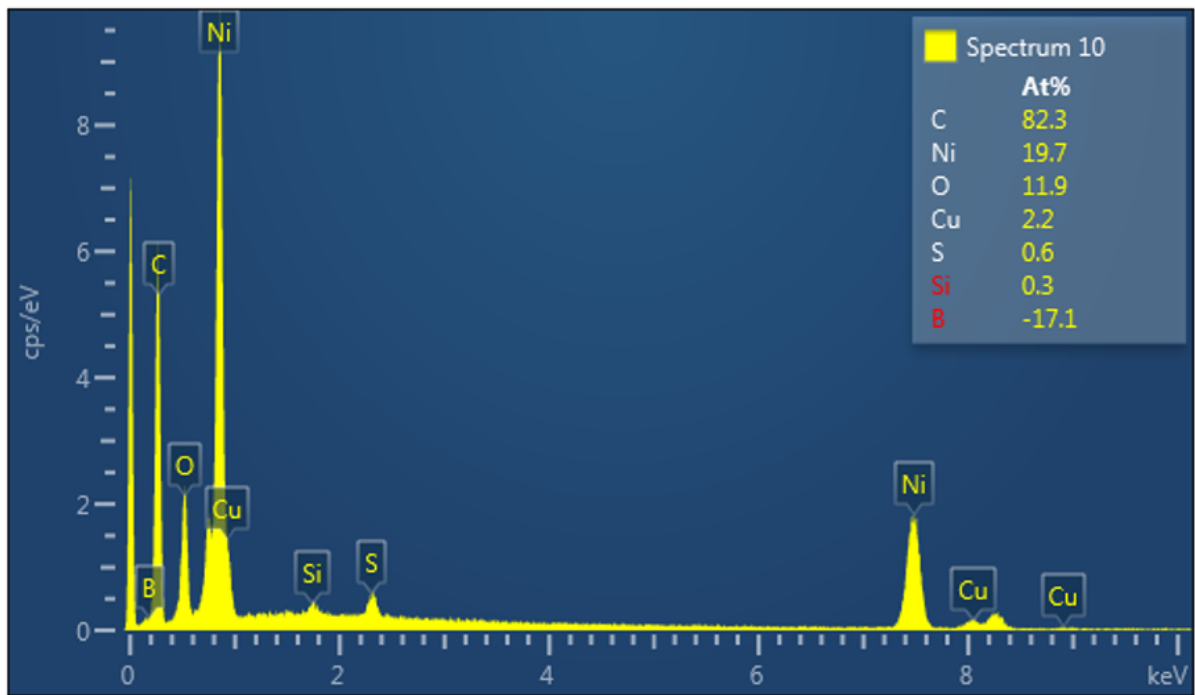
EDX Spectrum 7 Energy Dispersive Spectrum of bD(MM22)-BDD electrode after nickel deposition in a darker over-grown region.



EDX Spectrum 8. Energy Dispersive Spectrum of an f-BDD electrode after nickel deposition in a darker more nickel-rich region.



EDX Spectrum 9. Energy Dispersive Spectrum of an f-BDD electrode after nickel deposition in a darker low nickel region.



EDX Spectrum 10. Energy Dispersive Spectrum of an f-BDD electrode after nickel deposition in a lighter less nickel-rich region.